ANALYSIS OF THE NUCLEAR POTENTIAL FOR HEAVY-ION SYSTEMS THROUGH LARGE-ANGLE QUASI-ELASTIC SCATTERING

MOHD LUKMAN BIN INCHE IBRAHIM

THESIS SUBMITTED IN FULFILMENT OF THE REQUIREMENT FOR THE DEGREE OF DOCTOR OF PHILOSOPHY

DEPARTMENT OF PHYSICS
FACULTY OF SCIENCE
UNIVERSITY OF MALAYA
KUALA LUMPUR

2012

Abstract

The knowledge of the nuclear potential between two colliding nuclei is a fundamental ingredient in understanding a nucleus-nucleus collision. In order to study the nuclear potential, the colliding nuclei must be brought together close enough so that they experience the nuclear interaction. It has been demonstrated that large-angle quasi-elastic scattering is a suitable method to study the nuclear potential. In this thesis, analyses on the nuclear potential for heavy-ion systems, namely ^{48}Ti, ^{54}Cr, ^{56}Fe, ^{64}Ni, and ^{70}Zn + ^{208}Pb systems, have been performed through large-angle quasi-elastic scattering. At energies around the Coulomb barrier height, it has been well known that the effect of channel couplings, that is the coupling between the relative motion of the colliding nuclei and their intrinsic motions as well as transfer processes, plays an important role. Therefore, a coupled-channels procedure must be applied to take account of this effect. CQEL, which is a modified version of a computer code CCFULL, has been employed in order to perform these complex calculations. The nuclear potential is assumed to have a Woods-Saxon form, which is characterized by the surface diffuseness parameter, the potential depth, and the radius parameter. It is found that low values of the diffuseness parameter in comparison with the widely accepted value of around 0.63 fm are required in order to fit the experimental data at deep sub-barrier energies, that is at energies well below the Coulomb barrier height. In order to see the effect of collision energies on the deduced values of the diffuseness parameter, experimental data with energies up to 3 MeV below the Coulomb barrier height are used in the fittings.

This leads to higher deduced values of the diffuseness parameter, which are closer to the widely accepted value. It seems that the phenomenon of threshold anomaly might explain the relatively low diffuseness parameters obtained at deep sub-barrier energies, and also the increase in the diffuseness parameters as the collision energies increase. It is also possible that the increase in the diffuseness parameters with respect to the energies is due to the same reasons that might cause the diffuseness parameters obtained through fusion experimental data higher than those obtained through scattering experimental data. One of the possible reasons is the dynamical effects, particularly regarding the neutron movements. Furthermore, the increase in the diffuseness parameters as the collision energies are increased also seems to have a possible tendency to be a function of the charge product of the target and projectile nuclei.

Abstrak

Pengetahuan tentang keupayaan nuklear diantara dua nukleus yang berlanggar adalah sangat penting dalam memahami perlanggaran antara nukleus. Bagi membolehkan keupayaan nuklear diselidik dan difahami, dua nukleus yang bertembung perlu berada cukup dekat diantara satu sama lain supaya nukleus-nukleus tersebut merasai tarikan nuklear. Ianya telah dibuktikan bahawa serakan kuasikenyal pada sudut besar merupakan satu cara yang sangat sesuai untuk menyelidik keupayaan nuklear. Didalam tesis ini, analisis tentang keupayaan nuklear untuk sistem-sistem ion berat, atau dengan lebih tepat lagi untuk sistem-sistem ^{48}Ti, ^{54}Cr, ^{56}Fe, ^{64}Ni, dan ^{70}Zn + ^{208}Pb, dilakukan dengan menggunakan serakan kuasikenyal pada sudut besar. Pada tenaga sekitar puncak halangan Coulomb, ianya sememangnya diketahui bahawa kesan gandingan saluran, iaitu gandingan diantara pergerakan relatif nukleus-nukleus yang berlanggar dengan pergerakan intrinsik nukleus-nukleus tersebut dan proses pemindahan nukleon, memainkan peranan yang penting. Oleh itu, kaedah gandingan saluran perlu digunakan bagi membolehkan kesan tersebut diambil kira. CQEL, yang merupakan satu versi yang diubahsuai daripada kod komputer CCFULL, digunakan bagi melaksanakan pengiraan-pengiraan yang rumit ini. Keupayaan nuklear diandai mempunyai bentuk Woods-Saxon, yang dicirikan oleh parameter penyebaran permukaan, kedalaman keupayaan, dan parameter jejari. Ianya didapati bahawa nilai-nilai parameter penyebaran yang jauh lebih rendah berbanding dengan nilai yang diterima umum, iaitu sekitar 0.63 fm, diperlukan bagi membuat penyuaian terbaik kepada data-data eksperi-

men pada tenaga jauh dibawah puncak halangan Coulomb. Bagi menkaji kesan tenaga perlanggaran keatas nilai-nilai parameter penyebaran yang diperolehi, data-data eksperimen dengan tenaga sehingga 3 MeV dibawah puncak halangan Coulomb digunakan dalam penyuaian terbaik. Ini membawa kepada nilai-nilai parameter penyebaran yang diperolehi menjadi lebih tinggi, yang mana lebih dekat dengan nilai parameter penyebaran yang diterima umum. Nilai-nilai parameter penyebaran yang jauh lebih rendah berbanding dengan nilai yang diterima umum yang diperolehi pada tenaga jauh dibawah puncak halangan Coulomb, dan peningkatan nilai-nilai parameter penyebaran apabila tenaga meningkat mungkin boleh dijelaskan oleh fenomena ambang anomali. Peningkatan nilai-nilai parameter penyebaran apabila tenaga meningkat mungkin juga disebabkan oleh faktor-faktor yang sama yang mungkin menyebabkan nilai-nilai parameter penyebaran yang diperolehi melalui data eksperimen lakuran menjadi lebih tinggi daripada nilai-nilai yang diperolehi melalui data eksperimen serakan. Diantara faktor-faktor tersebut adalah kesan dinamik, terutamanya berkenaan pergerakan neutron. Selain daripada itu, peningkatan nilai-nilai parameter penyebaran apabila tenaga perlanggaran lebih tinggi berkemungkinan mempunyai kecenderungan sebagai fungsi hasil darab caj nukleus sasaran dan caj nukleus pelancar.

Acknowledgments

First of all, I would like to thank my supervisor, Assoc. Prof. Dr. Hasan Abu Kassim, for his support and guidance throughout my research project. I would also like to express a special acknowledgment to Dr. Muhammad Zamrun, who spent a year in the University of Malaya as a Research Fellow at the Department of Physics. His knowledge and experience in nuclear reactions have guided and enabled me to complete this thesis.

There are many others who have contributed to my research through formal and informal discussions and assistances. I would like to thank all my friends, particularly those who are in the Theoretical Physics Lab, who have helped me so much. I wish all the best for the future to all of them.

I would like to express my gratitude to the Department of Physics and the University of Malaya for the opportunity that they have given to me to pursue my study in Physics, and for their financial supports through Fellowship and Research Assistantship.

Special thanks to my family, especially to my parents for their love and continuous support.

Contents

List of Figures

List of Tables

Chapter 1

Introduction

The knowledge of the potential between two colliding nuclei is of fundamental importance in order to describe nucleus-nucleus collisions. The nucleus-nucleus potential is the sum of a short range attractive nuclear potential $V_N(r)$ and a long range repulsive Coulomb potential $V_C(r)$. The Coulomb potential is well understood. This has been demonstrated by the accurate description of the Coulomb or Rutherford scattering, the scattering where only the long range Coulomb potential acts.

Unlike the Coulomb potential, the exact form of the attractive potential between two nuclei is not fully known. One way to determine the nuclear potential is to accept a certain form of it and determine the parameters so that the experimental data are reproduced. The phenomenological Woods-Saxon form [1], which is characterized by the surface diffuseness parameter, the potential depth, and the radius parameter, is the most widely used. The main attractiveness is that it is relatively simple, which would make theoretical calculations easier to be performed.

The nuclear potential can be studied through fusion or quasi-elastic scattering experimental data. Quasi-elastic scattering is the sum of elastic scattering, inelastic scattering and transfer reaction. Thus, quasi-elastic scattering and fusion are complementary to each other due to flux conservation. At zero im-

pact parameter (i.e. head-on collision), quasi-elastic scattering is related to the reflection probability by the potential barrier, while fusion is related to the penetration probability. Strictly speaking, it is impossible to experimentally measure the quasi-elastic cross sections at deflection angle of 180°. However, it has been shown that large-angle quasi-elastic scattering can be well approximated as scattering at zero impact parameter through a centrifugal correction [2, 3].

There are advantages of studying the nuclear potential through the experimental data of quasi-elastic scattering rather than fusion. For example, measuring fusion cross sections requires specialized recoil separator (electrostatic deflector/ velocity filter) typically with low acceptance and efficiency. On the other hand, the measurement of quasi-elastic cross sections needs only a very simple charged particle detector. This means that the experimental data of quasi-elastic scattering are likely to be more accurate and less error-prone than the experimental data of fusion. Hence, more accurate analyses on the nuclear potential can be made through quasi-elastic scattering experimental data. Besides, several effective energies can be measured from a single-beam energy. This is because each scattering angle corresponds to scattering at a certain angular momentum in the semi-classical approximation. Thus, by taking the centrifugal correction into account, the cross sections can be scaled in energy.

Heavy-ion collisions involve the incidence of relatively heavy projectiles on targets. If a compound nucleus is created, it would have a high atomic number. The developments and improvements of experimental equipment and techniques have enabled heavy-ion reactions to be performed and measured with a high degree of accuracy. Previously, studies on nuclei mainly involved the bombardments on targets with light ions such as protons and alpha particles. In heavy-ion collisions, many interesting phenomena can occur. For example, by properly selecting targets and projectiles, it is possible to specifically excite different degrees of freedom in the nuclei, which are associated with the

single-particle motion and the collective motion. The exploration in 'the island of stability'—the isolated region where nuclei are stable—has also led to the formation of many super-heavy elements that are not found in nature [4–6]. Regarding the nuclear potential, it has been shown that the parameters of the nuclear potential for heavy-ion systems obtained through fusion experimental data differ from the ones obtained through quasi-elastic scattering experimental data [7], and this is still not well understood. Therefore, it is apparent that more studies on the nuclear potential for heavy-ion collisions, which might be unique from the nuclear potential for light-ion collisions, are required in order to make further progress in understanding heavy-ion reactions. The objective of this thesis is to study the nuclear potential, particularly the diffuseness parameter, for heavy-ion systems through large-angle quasi-elastic scattering. The diffuseness parameter determines the characteristic at the surface region of the nuclear potential.

In order to study the nuclear potential, the colliding nuclei must be brought together close enough so that the nuclear force of one nucleus is felt by the other nucleus. Therefore, it is necessary for the nuclei to collide at energies close enough to the Coulomb barrier height. Near the Coulomb barrier height, it has been well established that the internal structures of the colliding nuclei play a significant role [8]. For example, it has been shown that the coupling to the collective excitations such as the vibrational and the rotational states in the target and projectile nuclei enhance the sub-barrier fusion cross sections [8], therefore, reducing the sub-barrier quasi-elastic cross sections. Numerically solving the coupled-channels equations, including all relevant channels, are the standard way to apply the effect of channel couplings between the relative motion and the intrinsic degrees of freedom of the colliding nuclei. However, the full coupled-channels calculations turn into a very complex problem if many physical channels are included simultaneously. This also leads to

a very long computing time in order to solve the equations. Therefore, several simplifications have often been applied. In this thesis, we employ the so-called no-Coriolis approximation in solving the coupled-channels equations, which has been shown to work very well for both large angle quasi-elastic scattering and fusion reactions [3, 8–10].

This thesis is organized as follows. In Chapter 2, heavy-ion collisions around the Coulomb barrier are discussed. First, we briefly discuss the nucleus-nucleus potential. Next, we review the experimental method to measure quasi-elastic cross sections. We then discuss the coupled-channels equations, together with the method to solve these equations. The scaling property for large-angle quasi-elastic scattering is also reviewed.

In Chapter 3, we perform analyses on the nuclear potential for heavy-ion systems using large-angle quasi-elastic scattering experimental data of ^{48}Ti, ^{54}Cr, ^{56}Fe, ^{64}Ni, and ^{70}Zn + ^{208}Pb systems at deep sub-barrier energies. We study these collision systems since only the experimental data for these systems are available to us. Deep sub-barrier energies correspond to the penetration at the outer tail of the nuclear potential, thus still enable us to study the nuclear potential. One of the main attractions for determining the nuclear potential using the experimental data at these energies is that channel couplings can be neglected since they are weak [11–13], thus simplifying the calculations significantly.

In order to make a more comprehensive study on the nuclear potential, it is also important to investigate its dependence on certain aspects. In Chapter 4, by using the same heavy-ion systems as in Chapter 3, we intend to examine the effect of collision energies on the deduced nuclear potential. Therefore, we perform an investigation by using large-angle quasi-elastic scattering experimental data with energies up to 3 MeV below the Coulomb barrier height in the fittings. However, the effect of channel couplings must be considered in this

case. The results in Chapter 4 can be compared with the results in Chapter 3 in order to see the effect of increasing the collision energies on the deduced nuclear potential.

The thesis is then summarized in Chapter 5.

Chapter 2

Heavy-ion collision around the Coulomb barrier

2.1 The nucleus-nucleus potential

First, let us briefly discuss the nucleus-nucleus potential, which is the sum of a short range attractive nuclear potential V_N and a long range repulsive Coulomb potential V_C. The Coulomb potential between two spherical nuclei with uniform charge density distributions and when they do not overlap is given by [14]

$$V_C(r) = \frac{Z_P Z_T e^2}{r}, \tag{2.1}$$

where Z_P, Z_T, r, and e are the atomic number of the projectile, the atomic number of the target, the distance between the centers of the colliding nuclei, and the elementary charge (Gaussian units), respectively. When the nuclei overlap, the Coulomb potential is given by [14]

$$V_C(r) = \frac{Z_P Z_T e^2}{2R_C}\Big[3 - \Big(\frac{r}{R_C}\Big)^2\Big], \tag{2.2}$$

where R_C is the radius of the of the equivalent sphere of the target and projectile.

For the nuclear potential, the Woods-Saxon form is widely used, and is given by [1]

$$V_N(r) = -\frac{V_0}{1 + \exp[(r - R_0)/a]}, \tag{2.3}$$

where V_0 is the potential depth, a is the surface diffuseness parameter, and $R_0 = r_0 \left(A_T^{1/3} + A_P^{1/3}\right)$, where r_0 is the radius parameter, while A_T and A_P are the mass numbers of the target and the projectile, respectively. Throughout this thesis, the nuclear potential is assumed to have the Woods-Saxon form. The diffuseness parameter determines the characteristic at the surface region of the nuclear potential. Figure 2.1 illustrates the characteristic of the nuclear potential at the surface region using different values of the diffuseness parameter. It can be seen that a higher diffuseness parameter makes the nuclear potential to become more spread out.

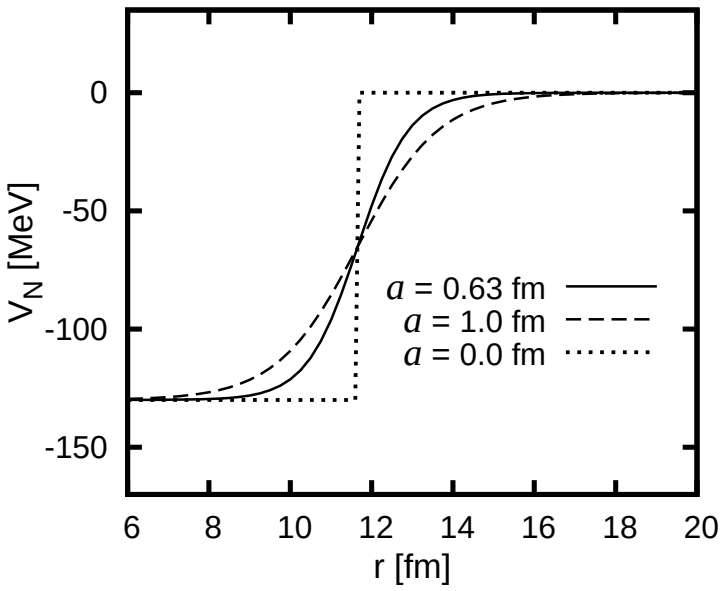

Figure 2.1: Illustration of the characteristic of the nuclear potential V_N at the surface region as a function of the distance between two nuclei using three different values of the diffuseness parameter a.

The radial Schrödinger equation comprises an effective potential defined by

[can refer to Eq. (2.11)]

$$V_{\text{eff}}(l,r) = V_N(r) + V_C(r) + \frac{\hbar^2 l(l+1)}{2\mu r^2}, \tag{2.4}$$

which is a sum of nuclear, Coulomb and centrifugal components. Figure 2.2 shows a typical nucleus-nucleus interaction for a heavy-ion system at zero angular momentum $l = 0$. The nucleus-nucleus potential produces a Coulomb barrier height V_B, located at a distance R_B between the centers of the colliding nuclei. The location of the potential pocket is denoted by r_{abs} in Fig. 2.2.

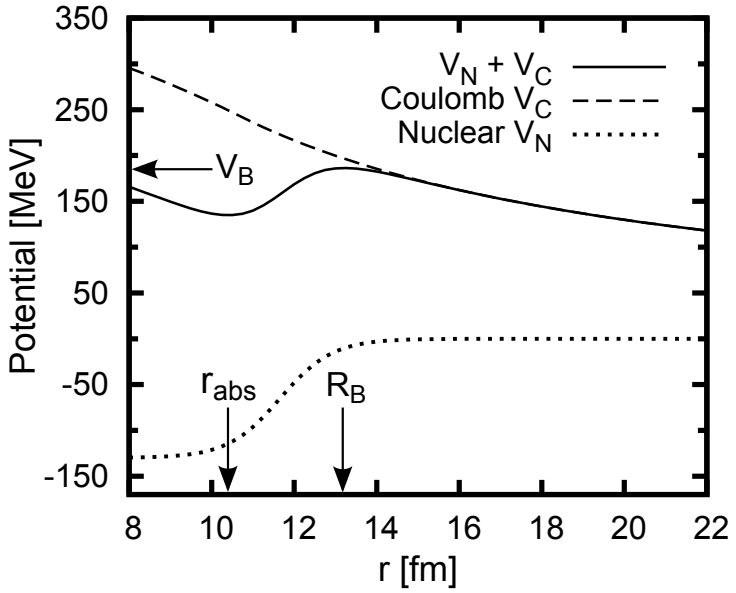

Figure 2.2: A typical nucleus-nucleus potential of a heavy-ion system at $l = 0$. The dotted, dashed and solid lines represent the nuclear potential V_N, Coulomb potential V_C, and the sum of the nuclear and Coulomb potentials, respectively.

In this thesis, we will study the nuclear potential for heavy-ion systems through large-angle quasi-elastic scattering, in particular using the collisions of ^{208}Pb with ^{48}Ti, ^{54}Cr, ^{56}Fe, ^{64}Ni and ^{70}Zn. Fusion reactions are regarded to certainly take place once a portion of the incoming flux traverses the Coulomb barrier, while the remaining flux is reflected by the barrier as quasi-elastic scattering. Next, the experimental methods to measure the quasi-elastic cross sections are reviewed. Then, we formulate the coupled-channels formalism for

the processes mentioned above.

2.2 Experimental method for large-angle quasi-elastic scattering

2.2.1 Introduction

The residual of the in-going flux particles that is not transmitted through the Coulomb barrier is generally reflected. We can quantify the reflected flux in terms of differential quasi-elastic scattering cross sections. By definition, quasi-elastic scattering comprises of elastic and inelastic scattering, and reactions involving the transfer of a few nucleons between the colliding nuclei. In this particular section, the experimental methods to measure the quasi-elastic cross sections are discussed. We introduce two different methods to measure the quasi-elastic cross sections [15]. One of the methods is by detecting the scattered projectile-like nuclei at backward angles, while the other is by measurement of the recoiling target-like nuclei at forward angles.

2.2.2 Detection at backward angles

Figure 2.3 illustrates the experimental set-up to detect quasi-elastic scattering at backward angles. A gas-ionization detector is positioned at a certain angle θ relative to the beam direction. The angle $\theta = 170^{\circ}$ was chosen by the Canberra group. Choosing the best position of the detector in performing the experiment will be discussed in Section 2.6 (scaling property). The energy loss ΔE of the scattered particles is measured by this detector. The silicon surface-barrier detector must be located at the edge of the gas-ionization detector in order to measure their residual energy E_{res}. For each beam energy, the combined information from these two detectors enable the atomic numbers of the detected

nuclei to be identified. This is shown in Fig. 2.4(a) for the ^{16}O + ^{144}Sm reaction. The elastic events is clearly differentiated from the inelastic events in the energy spectra, as shown in Fig. 2.4(b). This enables the extraction of the elastic scattering differential cross sections.

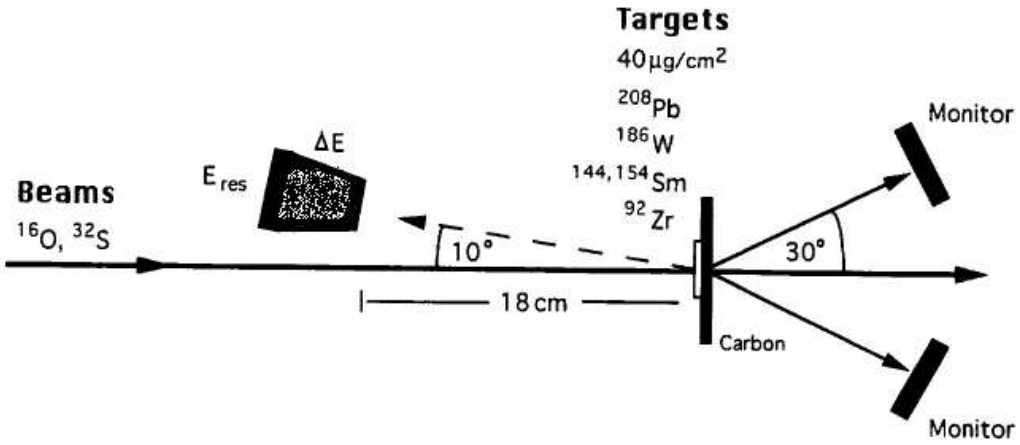

Figure 2.3: Schematic view of the experimental set-up which was used to measure the quasi-elastic scattering at backward angles by the Canberra group. Taken from Timmers [15].

2.2.3 Detection of recoils at forward angles

By detecting target-like nuclei, the quasi-elastic scattering cross sections can also be measured together with the fusion measurements. The recoils are detected through four monitor detectors located at forward angle $\theta_{\rm lab}$. The scattering angle of the recoiling target-like nucleus $\theta'_{\rm lab}$, and the angle of the scattered projectile-like nucleus $\theta_{\rm lab}$ for elastic scattering are related in the laboratory system by [15]

$$\cos^2(\theta'_{\rm lab}) = \frac{(A_P + A_T)^2}{4A_P A_T} - \frac{A_P}{4A_T}\left(\cos(\theta_{\rm lab}) + \sqrt{\frac{A_T^2}{A_P^2} - \sin^2(\theta_{\rm lab})}\right), \qquad (2.5)$$

Thus, for the ^{40}Ca + ^{96}Zr scattering for example, the detections of the recoiling zirconium nucleus at $\theta'_{\rm lab} = 22^\circ$ correspond to the scattering of ^{40}Ca projectile

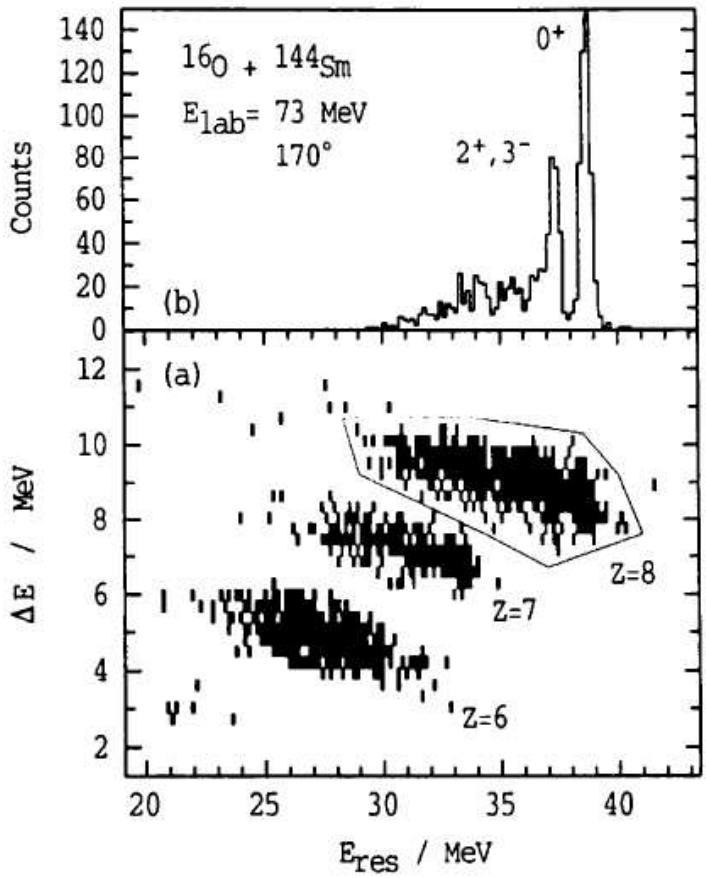

Figure 2.4: The lower panel (a) shows ΔE versus E_{res} for the $^{16}\mathrm{O}$ + $^{144}\mathrm{Sm}$ reaction at energy 73 MeV and $\theta = 170°$ in the laboratory frame. It can be seen that the scattered particles are clearly distinguished according their atomic numbers. The upper panel (b) shows the energy spectrum of the scattered oxygen nuclei. The channels associated with the 0^+ and the combination of the 2^+ and 3^- states of $^{144}\mathrm{Sm}$ are resolved. Taken from Timmers *et al.* [2].

at $\theta_{\rm lab} = 113.5°$. The scattering angle in the center-of-mass system in this case is $\theta_{\rm c.m.} = 136°$, since [15]

$$\tan(\theta_{\rm lab}) = \frac{\sin(\theta_{\rm c.m.})}{\cos(\theta_{\rm c.m.}) + A_P/A_T}. \tag{2.6}$$

A typical energy spectrum of particles detected by detectors at $\theta_{\rm lab} = 22°$ is shown in Fig. 2.5. The recoil peak in this spectra is identified from its energy relation to the Rutherford scattering peak as given by the reaction kinematics. The recoil peaks are integrated in the spectra of the four monitor detectors by shifting a fixed gate proportional to recoil energy. The number of counts are reduced by a background estimated as obtained from a region close to the peak. For each energy, the recoil counts of the four detectors are added and divided by the number of counts in the Rutherford scattering peak. This process is to normalize the differential quasi-elastic cross sections with respect to the Rutherford cross section so that the data points at the lowest energies equal to unity.

2.3 Formal theory of scattering

In this section, a single-channel potential model is used to derive the basic formula for calculating the elastic and the fusion cross sections. The Schrödinger equation for the relative motion in three dimensions is given as

$$\Big[-\frac{\hbar^2}{2\mu}\nabla^2 + V(r) - E \Big]\psi(\vec{r}) = 0, \tag{2.7}$$

where $V(r)$ is the sum of nuclear and Coulomb potentials (i.e. $V(r) = V_N(r) + V_C(r)$) and μ is the reduced mass of the system. In the absence of the potential $V(r)$, one can explicitly solved this equation with $\psi = \exp(i\vec{k}.\vec{r})$, where $\vec{k}$ being the wave number vector, and the magnitude is given by $k = \sqrt{2\mu E/\hbar^2}$. This

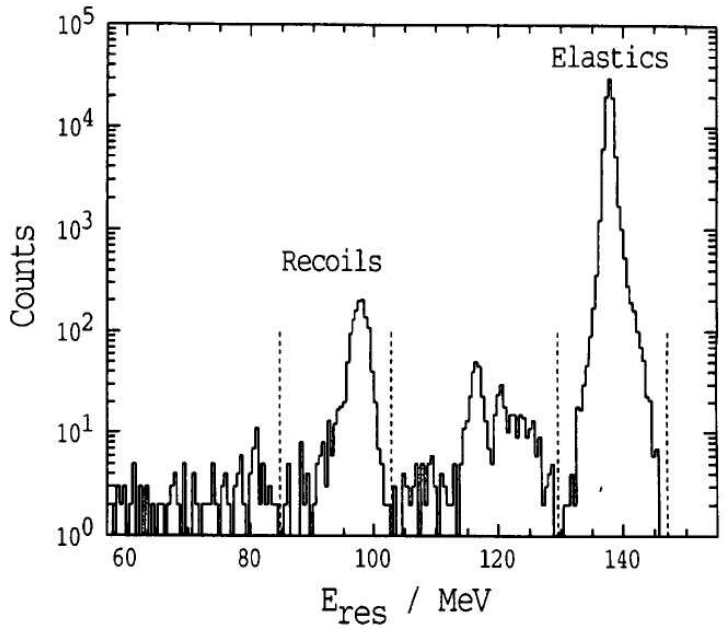

Figure 2.5: A typical energy spectrum of the particles detected by the monitor detector placed at forward angles $\theta = 22°$. The Rutherford scattering peak at 138 MeV comprises the most number of counts. The position of the gate is indicated by the dashed lines. Taken from Timmers [15].

solution has an asymptotic form of

$$\psi(r,\theta) = \quad e^{i\vec{k}.\vec{r}} \to \frac{i}{2k}\sum_{l=0}^{\infty}(2l+1)i^l\Big(\frac{e^{-ik(r-l\pi/2)}}{r} - \frac{e^{ik(r-l\pi/2)}}{r}\Big)P_l(\cos\theta)$$
$$r \to \infty, \tag{2.8}$$

where θ is the angle between $\vec{r}$ and $\vec{k}$, and P_l is the Legendre polynomials. The characteristic of the solution changes in the presence of the potential. However, the asymptotic form of the wave function can be written down in a similar way to Eq. (2.8) due to the fact that the potential vanishes at infinity. By substituting the plane waves with the corresponding Coulomb waves, the asymptotic form becomes

$$\psi(r,\theta) \to \frac{i}{2k}\sum_{l=0}^{\infty}(2l+1)i^l\Big(\frac{H_l^{(-)}(kr)}{r} - S_l\frac{H_l^{(+)}(kr)}{r}\Big)P_l(\cos\theta) \quad r \to \infty, \tag{2.9}$$

where $H_l^{(+)}(kr)$ and $H_l^{(-)}(kr)$ are the outgoing and the incoming Coulomb waves, respectively. S_l is the nuclear S-matrix and generally is a complex quantity.

The S-matrix is determined as follows. By expanding the wave function $\psi(\vec{r})$ in terms of the spherical harmonics as

$$\psi(\vec{r}) = \sum_{l=0}^{\infty} \sum_{m=-l}^{\infty} A_{lm} \frac{u_l(r)}{r} Y_{lm}(\vec{r}), \tag{2.10}$$

where A_{lm} is the expansion coefficient, $u_l(r)$ can fulfill the Schrödinger equation with

$$\left[-\frac{\hbar^2}{2\mu} \frac{d^2}{dr^2} + V(r) + \frac{l(l+1)\hbar^2}{2\mu r} - E \right] u_l(r) = 0. \tag{2.11}$$

The equation can be solved by imposing the boundary conditions

$$u_l(r) \sim r^{l+1} \qquad r \to 0 \tag{2.12}$$

$$= H_l^{(-)}(kr) - S_l H_l^{(+)}(kr) \qquad r \to \infty \tag{2.13}$$

Using the obtained nuclear S-matrix S_l, the differential elastic cross section is then evaluated as

$$\frac{d\sigma_{\rm el}}{d\Omega} = |f(\theta)|^2, \tag{2.14}$$

where

$$f(\theta) = \frac{i}{2k} \sum_{l=0}^{\infty} (2l+1) P_l(\cos\theta) (1 - S_l). \tag{2.15}$$

The total elastic cross section is given by

$$\sigma_{\rm el} = 2\pi \int_{-1}^{1} d(\cos\theta) \frac{d\sigma}{d\Omega} = \frac{\pi}{k^2} \sum_{l=0}^{\infty} (2l+1) |S_l - 1|^2. \tag{2.16}$$

The absorption of the incident flux can be considered as fusion reactions. The absolute value of the S-matrix is smaller than unity when the potential is complex. The difference between the incoming and the outgoing waves is

evaluated from Eq. (2.9) as

$$j_{\rm in} - j_{\rm out} = \frac{k\hbar}{\mu}\frac{\pi}{k^2}\sum_l (2l+1)\left(1-|S_l|^2\right). \tag{2.17}$$

In obtaining Eq. (2.17), the radial flux has been integrated for all possible values of θ. Dividing Eq. (2.17) with the incident flux $v = \hbar k/\mu$, the fusion cross section is then given by

$$\sigma_{\rm fus}(E) = \frac{\pi}{k^2}\sum_l (2l+1)\left(1-|S_l|^2\right). \tag{2.18}$$

In heavy-ion fusion reactions, rather than applying the regular boundary condition at the origin [Eq. (2.12)], the so-called incoming wave boundary condition (IWBC) has often been applied with keeping the potential real [10,16,17]. With this boundary condition, the wave function becomes

$$u_l(r) = \mathcal{T}_l \exp\left(-i\int_{r_{\rm abs}}^{r} k_l\left(r'\right)dr'\right), \qquad r \le r_{\rm abs} \tag{2.19}$$

at distances smaller than the absorption radius $r_{\rm abs}$, which are regarded to be inside the Coulomb barrier. $k_l(r)$ is the local wave number for the l-th partial wave and defined as

$$k_l(r) = \sqrt{\frac{2\mu}{\hbar^2}\left(E - V(r) - \frac{l(l+1)\hbar^2}{2\mu r^2}\right)}. \tag{2.20}$$

When there is a strong absorption in the inner region of the Coulomb barrier such that the incoming flux does not return back, this case is considered as the incoming wave boundary condition. For heavy-ion fusion reactions, the choice of the absorption radius $r_{\rm abs}$ does not affect the final results significantly. Usually $r_{\rm abs}$ is taken to be at the minimum position of the potential (see Fig. 2.2). Using the incoming wave boundary condition, $\mathcal{T}_l$ in Eq. (2.19) can be interpreted as the transmission coefficient. Therefore, the S-matrix S_l in Eq.

(2.13) is the reflection coefficient. Hence, Eq. (2.18) can be written as

$$\sigma_{\rm fus}(E) = \frac{\pi}{k^2}\sum_l (2l+1)P_l(E), \tag{2.21}$$

where $P_l(E)$ is the penetrability which is defined as

$$P_l(E) = 1 - |S_l|^2 = \frac{k_l(r_{\rm abs})}{k}|\mathcal{T}_l|^2 \tag{2.22}$$

for the boundary conditions of Eqs. (2.12) and (2.19).

2.4 Coupled-channel formalism

2.4.1 Coupled-channels equation with full angular momentum

Let us now discuss the effect of coupling to intrinsic degrees of freedom in heavy-ion collisions. When the number of the intrinsic degrees of freedom is small, this problem can be addressed by explicitly solving the Schrödinger equation.

The effect of the coupling between the relative motion and several intrinsic motions of the colliding nuclei has been shown to cause large enhancements of the fusion cross sections at collision energies below the Coulomb barrier. This has been demonstrated by extensive experimental as well as theoretical studies [8,18,19]. Quasi-elastic scattering is also influenced by a similar effect, where the cross sections at collision energies above the Coulomb barrier are larger than the prediction of one dimensional model [2, 3, 20, 21]. Among the possible intrinsic excitations of nuclei, the low-lying collective motions have been revealed as the most significant nuclear intrinsic motions for heavy-ion collisions , e.g. the low-lying vibrational excitations with several multi-polarities, or the rotational motion of deformed nuclei [8, 18]. In certain situations, the coupling to nucleon transfer processes also serves a role [2, 22–25]. In this section, we formulate the

coupled-channels framework for heavy-ion collisions, which is also the basis in formulating the computer code that is used in this thesis.

Let us consider a collision between two nuclei in the presence of the coupling between the relative motion of the center of mass of the colliding nuclei, $\vec{\mathbf{r}} = (r, \hat{\mathbf{r}})$ and the nuclear intrinsic motion ξ. We can say that Hamiltonian for the system is

$$H\left(\vec{\mathbf{r}}, \xi\right) = -\frac{\hbar^2}{2\mu}\nabla^2 + V(r) + H_0(\xi) + V_{\text{coup}}\left(\vec{\mathbf{r}}, \xi\right), \tag{2.23}$$

where μ is the reduced mass of the system, $V(r)$ is the bare potential in the absence of the coupling which consists of the nuclear and Coulomb parts ($V(r) = V_N(r) + V_C(r)$), $H_0(\xi)$ is the Hamiltonian for the intrinsic motion, and V_{coup} is the mentioned coupling. The Schrödinger equation for the total wave function then becomes

$$\left(-\frac{\hbar^2}{2\mu}\nabla^2 + V(r) + H_0(\xi) + V_{\text{coup}}\left(\vec{\mathbf{r}}, \xi\right)\right)\Psi\left(\vec{\mathbf{r}}, \xi\right) = E\Psi\left(\vec{\mathbf{r}}, \xi\right). \tag{2.24}$$

The internal degree of freedom ξ basically has a finite spin. We can write the coupling Hamiltonian in multipoles as

$$V_{\text{coup}}\left(\vec{\mathbf{r}}, \xi\right) = \sum_{\lambda>0,\mu} f_\lambda(r) Y_{\lambda\mu}\left(\hat{\mathbf{r}}\right) \cdot T_{\lambda\mu}\left(\xi\right), \tag{2.25}$$

where $Y_{\lambda\mu}\left(\hat{\mathbf{r}}\right)$ is the spherical harmonics and $T_{\lambda\mu}\left(\xi\right)$ is the spherical tensors built from the internal coordinate. The dot means a scalar product. The sum is taken over all values of λ except for $\lambda = 0$ since it is already considered in $V(r)$.

The expansion basis for the wave function in Eq. (2.24) for a fixed total angular momentum J and its z-component M is defined as

$$\langle \vec{\mathbf{r}}\xi | (nlI)JM\rangle = \sum_{m_l, m_I} \langle l m_l I m_I | JM\rangle Y_{l m_l}(\hat{\mathbf{r}}) \varphi_{n I m_I}(\xi), \tag{2.26}$$

where l and I are the orbital and the internal angular momenta, respectively. $\varphi_{nIm_I}(\xi)$ is the wave function for the internal motion which fulfills

$$H_0(\xi)\varphi_{nIm_I}(\xi) = \epsilon_n \varphi_{nIm_I}(\xi). \tag{2.27}$$

The total wave function $\Psi(\vec{\mathbf{r}}, \xi)$ is expanded with this basis as

$$\Psi(\vec{\mathbf{r}}, \xi) = \sum_{n,l,I} \frac{u^J_{nlI}(r)}{r} \langle \vec{\mathbf{r}}\xi | (nlI)JM \rangle, \tag{2.28}$$

The Schrödinger equation [Eq. (2.24)] can then be written as a set of coupled equations for $u^J_{nlI}(r)$

$$\begin{aligned} &\left[-\frac{\hbar^2}{2\mu}\frac{d^2}{dr^2} + V(r) + \frac{l(l+1)\hbar^2}{2\mu r^2} - E + \epsilon_n \right] u^J_{nlI}(r) \\ &+ \sum_{n',l',I'} V^J_{nlJ;n',l',I'}(r) u^J_{n',l',I'}(r) = 0, \end{aligned} \tag{2.29}$$

where the coupling matrix elements $V^J_{nlJ;n',l',I'}$ are given as

$$\begin{aligned} V^J_{nlJ;n',l',I'}(r) &= \langle JM(nlI)|V_{\rm coup}(\vec{\mathbf{r}}, \xi)|(n', l', I')JM\rangle \\ &= \sum_{\lambda} (-)^{I-I'+l'+J} f_\lambda(r) \langle l \| Y_\lambda \| l' \rangle \langle nI \| T_\lambda \| n'I' \rangle \\ &\quad \times \sqrt{(2l+1)(2I+1)} \begin{Bmatrix} I' & l' & J \\ l & I & \lambda \end{Bmatrix}. \end{aligned} \tag{2.30}$$

The reduced matrix elements in Eq. (2.30) are defined by

$$\langle l m_l | Y_{\lambda\mu} | l' m_{l'} \rangle = \langle l' m_{l'} \lambda\mu | l m_l \rangle \langle l \| Y_\lambda \| l' \rangle. \tag{2.31}$$

Since $V^J_{nlJ;n',l',I'}(r)$ are independent of the index M, the index has been suppressed as seen in Eq. (2.30). Equation (2.29) is called *coupled-channels equations*. For heavy-ion fusion reactions, these equations are usually solved using

the incoming wave boundary conditions

$$u^J_{nlI}(r) \sim \mathcal{T}^J_{nlI} \exp\left(-i\int_{r_{\rm abs}}^{r} k_{nlI}(r')dr'\right), \qquad r \le r_{\rm abs} \quad (2.32)$$

$$\to \frac{i}{2}\left(H^{(-)}_l(k_{nI}r)\delta_{n,n_i}\delta_{l,l_i}\delta_{I,I_i} + \sqrt{\frac{k_{nI_i}}{k_{nI}}}S^J_{lI}H^{(+)}_l(k_{nI}r)\right), \; r\to\infty \quad (2.33)$$

where $k_{nI} = \sqrt{2\mu(E-\epsilon_{nI})/\hbar^2}$, $k_{nI_i} = k = \sqrt{2\mu E/\hbar^2}$ and the local wave number k_{nlI} is defined as

$$k_{nlI}(r) = \sqrt{\frac{2\mu}{\hbar^2}\left(E - \epsilon_{nI} - \frac{l(l+1)\hbar^2}{2\mu r^2} - V(r) - V^J_{nlI;nlI}(r)\right)}. \quad (2.34)$$

Once we get the transmission coefficients $\mathcal{T}^J_{nlI}$, the penetrability through the Coulomb barrier is given by

$$P^J_{l_iI_i}(E) = \sum_{n,l,I}\frac{k_{nlI}(r_{\rm abs})}{k}|\mathcal{T}^J_{nlI}|^2, \quad (2.35)$$

where $k = k_{n_iI_i}$ is the wave number for the entrance channel. The fusion cross section for unpolarized target is given by

$$\sigma_{\rm fus}(E) = \frac{\pi}{k^2}\sum_{JMl_i}\frac{2J+1}{2I_i+1}P^J_{l_iI_i}(E). \quad (2.36)$$

The initial angular momentum l_i is J when the initial intrinsic spin I_i is zero. With the indexes l_i and I_i are suppressed in the penetrability, Eq. (2.36) then reads

$$\sigma_{\rm fus}(E) = \frac{\pi}{k^2}\sum_J(2J+1)P^J(E), \quad (2.37)$$

which is identical to Eq. (2.21), but the penetrability $P^J(E)$ is now affected by the channel couplings.

Contrary to the calculation of fusion cross sections, the calculation of quasi-elastic cross sections often requires a large value of angular momentum in order

to obtain converged results. The potential pocket at $r = r_{\rm abs}$ becomes shallow or even disappears for such large angular momentum. Hence, the incoming flux in Eq. (2.32) cannot be properly identified. Therefore, the quasi-elastic problem usually employ the regular boundary conditions at the origin rather than using the incoming wave boundary conditions. When using the regular boundary conditions, a complex potential, $V_N(r) = V_N^0(r) + iW(r)$, is required to simulate the fusion reaction. Once the nuclear S-matrix in Eq. (2.33) is obtained, the scattering amplitude can then be calculated as

$$\begin{aligned} f_{lI}^J(\theta, E) &= i\sum_{Jl}\sqrt{\frac{\pi}{kk_{nI}}}i^{J-l}e^{i[\sigma_J(E)+\sigma_l(E-\epsilon_{nI})]}\sqrt{2J+1}Y_{l0}(\theta)(S_{lI}^J - \delta_{I,I_i}\delta_{l,l_i}) \\ &\quad + f_C(\theta, E)\delta_{l,l_i}\delta_{I,I_i} \end{aligned} \tag{2.38}$$

where σ_l is the Coulomb phase shift and f_C is the Coulomb scattering amplitude. The phase shift is given by

$$\sigma_l = \arg\Gamma(l + 1 + i\eta), \tag{2.39}$$

where $\eta = Z_1 Z_2 e^2/\hbar\nu$ is the Sommerfeld parameter, while the scattering amplitude is given by

$$f_C(\theta, E) = \frac{\eta}{2k\sin^2(\theta/2)}\exp[-i\eta\ln[\sin^2(\theta/2)] + 2i\sigma_0(E)]. \tag{2.40}$$

Using Eq. (2.38), the differential cross section is evaluated as

$$\frac{d\sigma_{\rm qel}(\theta, E)}{d\Omega} = \sum_{JlI}\frac{k_{nI}}{k}|f_{lI}^J(\theta, E)|^2, \tag{2.41}$$

and from Eq. (2.40), the Rutherford cross section is given by

$$\frac{d\sigma_R(\theta, E)}{d\Omega} = |f_C(\theta, E)|^2 = \frac{\eta^2}{4k^2}\csc^4(\theta/2). \tag{2.42}$$

2.4.2 Coupled-channels equations in the no-Coriolis approximation

If many physical channels are considered, the full coupled-channels calculations [Eq. (2.30)] would be very difficult to manage. The dimension of the coupled-channels equations generally becomes too large for the practical purposes. In light of this, an approximation known as the no-Coriolis approximation, which is also called as the rotating frame approximation or the iso-centrifugal approximation, has often been used [9, 26–30]. The no-Coriolis approximation was initially used in the fields of chemistry under the name of centrifugal sudden approximation [31–33]. This approximation has also been employed in solving the electron molecule scattering problem [34].

For simplicity, let us say that the initial intrinsic spin is zero. In the no-Coriolis approximation, the whole system is transformed to the rotating frame such that the z-axis is along the direction of the relative motion $\vec{\mathbf{r}}$ at every instance [35]. One can accomplish this by replacing the angular momentum of the relative motion in each channel with the total angular momentum J, that is

$$\frac{l(l+1)\hbar^2}{2\mu r^2} \approx \frac{J(J+1)\hbar^2}{2\mu r^2}. \tag{2.43}$$

This assumption basically means that the change of the orbital angular momentum between the colliding nuclei due to the excitation of the intrinsic degree of freedom is negligible. The transformation to the rotating frame can be applied without leading to any complication since the operator for the rotational coordinate transformation in the whole space commutes with the centrifugal operator for the relative motion [35]. Using $Y_{\lambda\mu}(\hat{\mathbf{r}} = 0) = \sqrt{(2\lambda+1)/4\pi}\delta_{\mu,0}$, the coupling Hamiltonian of Eq. (2.25) in the rotating frame then reads

$$V_{\text{coup}}(r,\xi) = \sum_{\lambda} \sqrt{\frac{2\lambda+1}{4\pi}} f_\lambda(r) T_{\lambda 0}(\xi). \tag{2.44}$$

The complicated angular momentum coupling disappears in the no-Coriolis approximation as the coupling Hamiltonian no longer depends on the angular component of the relative coordinate between the colliding nuclei. Hence, the coupled-channels equations are transformed into those in a spin-less system. In the no-Coriolis approximation, the dimensions of the coupled-channels equations are drastically reduced. For example, the original coupled-channels equations for quadrupole mode of excitation ($\lambda = 2$) have 13 dimensions for $J > 4$ when the excitations are truncated at the second excited states. However, in the no-Coriolis approximation, the dimensions are reduced to 3.

To formulate the coupled-channels equations in the no-Coriolis approximation, the total wave function in the rotating frame can be expanded as

$$\Psi(\vec{\mathbf{r}}, \xi) = \sum_{nI} \frac{v^J_{nI}(r)}{r} Y_{J0}(\hat{\mathbf{r}}) \varphi_{nI0}(\xi). \tag{2.45}$$

The radial wave function for the (nI)-channel v^J_{nI} is connected to the original wave function as [36]

$$v^J_{nI}(r) = \sum_l \langle I0J0|l0\rangle u^J_{nlI}(r). \tag{2.46}$$

The coupled-channels equations for $v^J_{nI}(r)$ is then given by

$$\begin{aligned} &\left[-\frac{\hbar^2}{2\mu}\frac{d^2}{dr^2} + V(r) + \frac{J(J+1)\hbar^2}{2\mu r^2} - E + \epsilon_n\right] v^J_{nI}(r) \\ &+ \sum_{n',I'} \sum_{\lambda>0} \sqrt{\frac{2\lambda+1}{4\pi}} f_\lambda(r) \langle \varphi_{nI}|T_{\lambda 0}|\varphi_{n'I'}\rangle v^J_{n'I'}(r) = 0. \end{aligned} \tag{2.47}$$

For heavy-ion fusion reactions, these coupled-channels equations are again solved by employing the incoming wave boundary condition

$$u^J_{nlI}(r) \;\sim\; \mathcal{T}^J_{nI} \exp\left(-i \int_{r_{\rm abs}}^{r} k_{nJI}(r')dr'\right), \qquad r \le r_{\rm abs} \tag{2.48}$$

$$\rightarrow \frac{i}{2}\left(H_J^{(-)}(k_{nI}r)\delta_{n,n_i}\delta_{I,I_i} + \sqrt{\frac{k_{nI_i}}{k_{nI}}}S_I^J H_J^{(+)}(k_{nI}r)\right),\ r\rightarrow\infty \quad (2.49)$$

where k_{nI_i} , k_{nI} and $k_{nJI}(r)$ are defined the same as in the earlier subsection. The fusion cross section is given as in Eq. (2.37) where the penetrability is

$$P^J(E) = \sum_{n,I}\frac{k_{nJI}(r_{\rm abs})}{k}|\mathcal{T}_{nI}^J|^2. \quad (2.50)$$

As before, for large angle quasi-elastic scattering, the regular boundary condition is imposed at the origin instead of using the incoming wave boundary condition of Eq. (2.48) in order to solve Eq. (2.47). The quasi-elastic cross section can be calculated through Eq. (2.41) where the scattering amplitude is

$$\begin{aligned} f_{lI}^J(\theta,E) &= f_I^J(\theta,E) = i\sum_J\sqrt{\frac{\pi}{kk_{nI}}}e^{i[\sigma_J(E)+\sigma_J(E-\epsilon_{nI})]}\sqrt{2J+1} \\ &\quad\times Y_{J0}(\theta)(S_I^J-\delta_{I,I_i}) + f_C(\theta,E)\delta_{I,I_i}. \end{aligned} \quad (2.51)$$

Many studies have investigated the validity of the no-Coriolis approximation for both heavy-ion fusion reaction and quasi-elastic scattering and have shown that this approximation works very well [3, 8, 10].

2.5 Coupling to low-lying collective states

2.5.1 Vibrational coupling

Nuclear coupling

In this section, we will discuss the explicit form of the coupling Hamiltonian $V_{\rm coup}$. Throughout this thesis, we assume that the nuclear potential has a Woods-Saxon form as in Eq. (2.3). Let us first consider couplings of the relative motion to a $2^\lambda-$pole surface vibration of the target nucleus. The radius of the vibrating target nucleus in the geometrical model of Bohr and Mottelson is

characterized as

$$R_T(\theta,\phi) = R_T\left(1 + \sum_{\lambda} \alpha_{\lambda\mu} Y_{\lambda\mu}(\theta,\phi)\right), \tag{2.52}$$

with R_T is the equivalent sharp radius while $\alpha_{\lambda\mu}$ is the coordinate of the surface vibration. A harmonic oscillator can be used to approximate the surface oscillation and is given by

$$H_0 = \hbar\omega\left(\sum_{\mu} a^{\dagger}_{\lambda\mu} a_{\lambda\mu} + \frac{2\lambda+1}{2}\right), \tag{2.53}$$

where $\hbar\omega$ is the oscillator quanta and $a^{\dagger}_{\lambda\mu}$ and $a_{\lambda\mu}$ are the phonon creation and annihilation operators, respectively. The surface coordinate $\alpha_{\lambda\mu}$ is related to the phonon creation and annihilation operators by

$$\alpha_{\lambda\mu} = \alpha_0\left(a^{\dagger}_{\lambda\mu} + (-)^{\mu} a_{\lambda\mu}\right). \tag{2.54}$$

Here α_0 is the amplitude of the zero point motion and is related to the deformation parameter β_λ by $\alpha_0 = \beta_\lambda/\sqrt{2\lambda+1}$ [37]. The deformation parameter β_λ can be evaluated from the measured electromagnetic transition probability $B(E\lambda)\uparrow$ using [38]

$$\beta_\lambda = \frac{4\pi}{3Z_T R_C^{\lambda}}\left[\frac{B(E\lambda)\uparrow}{e^2}\right]^{1/2}, \tag{2.55}$$

where R_C is the Coulomb radius, and is taken to be the same as R_T.Therefore, α_0 is given by

$$\alpha_0 = \frac{1}{\sqrt{2\lambda+1}}\frac{4\pi}{3Z_T R_T^{\lambda}}\left[\frac{B(E\lambda)\uparrow}{e^2}\right]^{1/2}. \tag{2.56}$$

The angular momentum of the relative motion does not change in the no-Coriolis approximation. Evaluating the associated spherical harmonics in Eq.

(2.52) at angle $\hat{\mathbf{r}} = 0$ leads to the factor $\sqrt{(2\lambda+1)/4\pi}$. Thus, Eq. (2.52) reads

$$R_T(\theta, \alpha_{\lambda 0}) = R_T \left(1 + \sqrt{\frac{2\lambda+1}{4\pi}}\alpha_{\lambda 0}\right). \tag{2.57}$$

Using Eqs. (2.54), (2.56) and (2.57), the nuclear coupling potential can be written as

$$V_N^{\text{coup(vib)}}(r, \hat{O}_\lambda) = \frac{-V_0}{1 + \exp\left[\left(r - R_0 - R_T\hat{O}_\lambda/\sqrt{4\pi}\right)/a\right]}, \tag{2.58}$$

where the dynamical operator $\hat{O}_\lambda$ is

$$\hat{O}_\lambda = \beta_\lambda \left(a^\dagger_{\lambda 0} + a_{\lambda 0}\right). \tag{2.59}$$

The eigenvalues and the eigenvectors of the operator $\hat{O}_\lambda$ must be determined in order to obtained the matrix elements of the nuclear coupling Hamiltonian between the n-phonon state and the m-phonon state. The operator $\hat{O}_\lambda$ satisfies

$$\hat{O}_\lambda|\alpha\rangle = \xi_\alpha|\alpha\rangle. \tag{2.60}$$

The eigenvalues and eigenvectors can be obtained by diagonalizing the matrix elements of the operator between the phonon states,

$$O_{nm} = \beta_\lambda(\sqrt{m}\delta_{n,m-1} + \sqrt{n}\delta_{n,m+1}). \tag{2.61}$$

After the eigenvalues and eigenvectors are determined, then the nuclear matrix elements of Eq. (2.58) can be evaluated as

$$\begin{aligned} V^N_{nm}(r) &= \langle m|V_N^{\text{coup(vib)}}|n\rangle - V_N(r)\delta_{n,m} \\ &= \sum_\alpha \langle m|\alpha\rangle\langle\alpha|n\rangle \frac{-V_0}{1 + \exp\left[\left(r - R_0 - R_T\xi_\alpha/\sqrt{4\pi}\right)/a\right]} \\ &\quad -V_N(r)\delta_{n,m}. \end{aligned} \tag{2.62}$$

In order to ensure the coupling interaction vanishes in the entrance channel, the last term in Eq. (2.62) is introduced.

Coulomb coupling

Let us now look into the Coulomb part of the coupling Hamiltonian. The Coulomb potential between a point-like spherical projectile and a vibrating target is given by

$$\begin{aligned} V_C(\vec{\mathbf{r}}) &= \int d\vec{\mathbf{r}'} \frac{Z_P Z_T e^2}{|\vec{\mathbf{r}} - \vec{\mathbf{r}'}|} \rho_T(\vec{\mathbf{r}'}) \\ &= \frac{Z_P Z_T e^2}{r} + \sum_{\lambda' \neq 0} \sum_{\mu'} \frac{4\pi Z_P e}{2\lambda' + 1} Q_{\lambda'\mu'} Y^*_{\lambda'\mu'}(\hat{\mathbf{r}}) \frac{1}{r^{\lambda'+1}} \end{aligned} \tag{2.63}$$

where ρ_T is the charge density of the target nucleus, Z_T and Z_P are the atomic numbers of the target and the projectile nuclei, respectively, and $Q_{\lambda'\mu'}$ is the electric multipole operator defined by

$$Q_{\lambda'\mu'} = \int d\vec{\mathbf{r}} Z_T e \rho_T(\vec{\mathbf{r}}) r^{\lambda'} Y_{\lambda'\mu'}(\hat{\mathbf{r}}). \tag{2.64}$$

The first term on the right hand side of Eq. (2.63) is the bare Coulomb potential, while the second term is the Coulomb component of the coupling Hamiltonian. Equation (2.63) is obtained by using the following formula

$$\frac{1}{|\vec{\mathbf{r}} - \vec{\mathbf{r}'}|} = \sum_{\lambda'\mu'} \frac{4\pi}{2\lambda' + 1} \frac{r_<^{\lambda'}}{r_>^{\lambda'+1}} Y_{\lambda'\mu'}(\hat{\mathbf{r}'}) Y^*_{\lambda'\mu'}(\hat{\mathbf{r}}). \tag{2.65}$$

The relative coordinate r is assumed to be larger than the charge radius of the target nucleus. If the target nucleus is assumed to have a sharp distribution of matter, the electric multipole is given by

$$Q_{\lambda'\mu'} = \frac{3 Z_T e}{4\pi} R_T^{\lambda'} \alpha_{\lambda\mu} \delta_{\lambda,\lambda'} \delta_{\mu,\mu'} \tag{2.66}$$

up to the first order in the surface coordinate $\alpha_{\lambda\mu}$. Thus, we can write the coupling component of the Coulomb interaction as

$$\begin{aligned} V_C^{\text{coup(vib)}}(\vec{\mathbf{r}}, \alpha_{\lambda\mu}) &= \sum_{\lambda,\mu} \frac{3Z_P Z_T e^2}{2\lambda+1} \frac{R_T^\lambda}{r^{\lambda+1}} \alpha_{\lambda\mu} Y_{\lambda\mu}^*(\hat{\mathbf{r}}) \\ &= \sum_{\lambda,\mu} f_\lambda^C(r) \alpha_{\lambda\mu} Y_{\lambda\mu}^*(\hat{\mathbf{r}}) \end{aligned} \tag{2.67}$$

where

$$f_\lambda^C(r) = \frac{3Z_P Z_T e^2}{2\lambda+1} \frac{R_T^\lambda}{r^{\lambda+1}} \tag{2.68}$$

is called the Coulomb coupling form factor.

Transforming to the rotating frame according to the no-Coriolis approximation, the Coulomb coupling is given by

$$\begin{aligned} V_C^{\text{coup(vib)}}(r, \hat{O}_\lambda) &= \sum_{\lambda} 3Z_P Z_T e^2 \frac{R_T^\lambda}{r^{\lambda+1}} \frac{\alpha_{\lambda 0}}{\sqrt{4\pi}} \\ &= \sum_{\lambda} \frac{3Z_P Z_T e^2}{2\lambda+1} \frac{R_T^\lambda}{r^{\lambda+1}} \frac{\hat{O}_\lambda}{\sqrt{4\pi}} \end{aligned} \tag{2.69}$$

where $\hat{O}_\lambda$ is given by Eq. (2.59).

The Coulomb coupling matrix elements, denoted by $V_{nm}^C(r)$, can then be evaluated similar to the nuclear coupling Hamiltonian, with

$$\begin{aligned} V_{nm}^C(r) &= \langle m | V_C^{\text{coup(vib)}} | n \rangle \\ &= \sum_{\lambda} \frac{3Z_P Z_T e^2}{2\lambda+1} \frac{R_T^\lambda}{r^{\lambda+1}} \frac{\beta_\lambda}{\sqrt{4\pi}} [\sqrt{m}\delta_{n,m-1} + \sqrt{n}\delta_{n,m+1}] \end{aligned} \tag{2.70}$$

The total coupling matrix elements are basically the sum of the nuclear and the Coulomb couplings

$$V_{\text{coup}}(r) = V_{nm}^N(r) + V_{nm}^C(r). \tag{2.71}$$

Projectile and target excitations

The above formulation can also be extended to the case where the relative motion couples to the vibrational excitation of the projectile nucleus in addition to the vibrational excitation of the target nucleus. In this case, the coupling potential can be written as

$$V_{\rm coup}(r,\hat{O}_{\lambda_P},\hat{O}_{\lambda_T}) = V_C(r,\hat{O}_{\lambda_P},\hat{O}_{\lambda_T}) + V_N(r,\hat{O}_{\lambda_P},\hat{O}_{\lambda_T}), \tag{2.72}$$

$$\begin{aligned} V_C(r,\hat{O}_{\lambda_P},\hat{O}_{\lambda_T}) &= \frac{Z_P Z_T e^2}{r}\left(\frac{3R_P^{\lambda_P}}{(2\lambda_P+1)r^{\lambda_P}}\frac{\hat{O}_{\lambda_P}}{\sqrt{4\pi}}\right. \\ &\quad \left.+\frac{3R_T^{\lambda_T}}{(2\lambda_T+1)r^{\lambda_T}}\frac{\hat{O}_{\lambda_T}}{\sqrt{4\pi}}\right), \end{aligned} \tag{2.73}$$

$$\begin{aligned} V_N(r,\hat{O}_{\lambda_P},\hat{O}_{\lambda_T}) &= \frac{-V_0}{1+\exp\left(\dfrac{[r-R_0-(R_P\hat{O}_{\lambda_P}+R_T\hat{O}_{\lambda_T})/\sqrt{4\pi}]}{a}\right)} \\ &\quad -V_N(r). \end{aligned} \tag{2.74}$$

The $\hat{O}_{\lambda_T}$ and $\hat{O}_{\lambda_P}$ are the excitation operators for the target and projectile nuclei, respectively, and have a form of Eq. (2.59). λ_P and λ_T represent the multi-polarity of the vibrations in the projectile and the target nuclei, respectively. In Eq. (2.74), the term $V_N(r)$ is subtracted in order to avoid double counting.

The matrix elements of the coupling potential of Eq. (2.72) are evaluated in a similar way as Eqs. (2.62) and (2.70). Firstly, the operators $\hat{O}_{\lambda_P}$ and $\hat{O}_{\lambda_T}$ are diagonalize in the physical space in order to obtain their eigenvalues and eigenvectors. The coupling potentials are then calculated as

$$V_{nm}(r) = \langle m|V_{\rm coup}|n\rangle - V_N(r)\delta_{n,m}$$

$$
\begin{aligned}
= & \sum_{\alpha,\gamma} \langle m|\alpha\rangle\langle\alpha|n\rangle\langle m|\gamma\rangle\langle\gamma|n\rangle \\
& \times \frac{-V_0}{1+\exp\left(\dfrac{r-R_0-R_P\xi_\alpha/\sqrt{4\pi}-R_T\xi_\gamma/\sqrt{4\pi}}{a}\right)} \\
& + \sum_{\lambda_T,\lambda_P}\left[\frac{3Z_PZ_Te^2}{(2\lambda_T+1)}\frac{R_T^{\lambda_T}}{r^{\lambda_T+1}}\frac{\beta_{\lambda_T}}{\sqrt{4\pi}} + \frac{3Z_PZ_Te^2}{(2\lambda_P+1)}\frac{R_P^{\lambda_P}}{r^{\lambda_P+1}}\frac{\beta_{\lambda_P}}{\sqrt{4\pi}}\right] \\
& \times \left[\sqrt{n}\delta_{n,m+1}+\sqrt{n+1}\delta_{n,m-1}\right] - V_N(r)\delta_{n,m} \qquad (2.75)
\end{aligned}
$$

where $\xi_{\alpha(\gamma)}$ and $|\alpha(\gamma)\rangle$ are the eigenvalues and the eigenvectors for the operators $\hat{O}_{P(T)}$, respectively. This formalism will applied in the analyses of the quasi-elastic scattering at backward angles in Chapters 3 and 4.

In the previous section, we have shown that the dimension of the coupled-channels equations can be drastically reduced when the no-Coriolis approximation is employed. One can accomplish a further reduction by introducing the n-phonon channels [10, 27, 36]. The multi-phonon states generally have several levels at the same energy and they are distinguished from each other by the angular momentum and seniority [37]. As an example, for the quadrupole surface vibrations, the two-phonon triplet is degenerate in the excitation energy. The coupling to all members of the two-phonon triplet can therefore be replaced by the coupling to a single state given by

$$
|2\rangle = \sum_{I=0,2,4}\langle 2020|I0\rangle|I0\rangle = \frac{1}{\sqrt{2!}}\left(a_{20}^\dagger\right)^2|0\rangle. \qquad (2.76)
$$

Similarly, one can introduce the n-phonon channel for a general multipolarity λ as

$$
|n\rangle = \frac{1}{\sqrt{n!}}\left(a_{\lambda 0}^\dagger\right)^n|0\rangle. \qquad (2.77)
$$

If we truncate at the two-phonon states, the operator $\hat{O}_\lambda$ of Eq. (2.59) corresponds to the matrix elements which are given by

$$O_{mn} = \frac{1}{\sqrt{4\pi}} \begin{pmatrix} 0 & \beta_\lambda & 0 \\ \beta_\lambda & 0 & \sqrt{2}\beta_\lambda \\ 0 & \sqrt{2}\beta_\lambda & 0 \end{pmatrix}. \tag{2.78}$$

2.5.2 Rotational coupling

Nuclear Coupling

Here, we will look into the couplings to a ground state rotational band of the target nucleus. It is convenient to discuss them in the body fixed frame where the z-axis is along the orientation of the deformed target. The surface coordinate $\alpha_{\lambda\mu}$ is then transformed to

$$\alpha_{\lambda\mu} = \sum_{\mu'} D^{\lambda}_{\mu\mu'}(\phi_d, \theta_d, \chi_d) a_{\lambda\mu'}, \tag{2.79}$$

where ϕ_d, θ_d, χ_d are the Euler angles which describe the orientation of the target. If one considers a permanently deformed nucleus with the axial symmetry is about the body-fixed axis (z-direction), the deformation parameter $a_{\lambda\mu}$ have the form

$$a_{\lambda\mu} = \beta_\lambda \delta_{\mu 0}, \tag{2.80}$$

where β_λ is a constant which specifies the static deformation of the nucleus. In the space fixed frame we have

$$\alpha_{\lambda\mu} = \beta_\lambda D^{\lambda}_{\mu 0}(\phi_d, \theta_d, \chi_d). \tag{2.81}$$

Using Eqs. (2.52), (2.79) and (2.80), we have

$$R(\theta, \beta_\lambda) = R_T \left(1 + \sum_{\lambda\mu} \sqrt{\frac{4\pi}{2\lambda+1}} \beta_\lambda Y_{\lambda\mu}(\theta_d, \phi_d) Y^*_{\lambda\mu}(\hat{\mathbf{r}}) \right). \tag{2.82}$$

In getting Eq. (2.82), we have used the identity

$$D^{L}_{M0}(\phi,\theta,\chi)=\sqrt{\frac{4\pi}{2\lambda+1}}Y^{*}_{LM}(\theta,\phi). \tag{2.83}$$

In the rotating frame, Eq. (2.82) becomes

$$R(\theta,\beta_\lambda)=R_T\left(1+\sum_\lambda \beta_\lambda Y_{\lambda 0}(\theta)\right). \tag{2.84}$$

Using this equation, the nuclear coupling has a similar form as Eq. (2.58) with

$$V_N^{\mathrm{coup(rot)}}(r,\hat{O}_\lambda)=\frac{-V_0}{1+\exp\left[(r-R_0-R_T\hat{O}_\lambda)/a\right]}. \tag{2.85}$$

However, the dynamical operator $\hat{O}_\lambda$ is now given by

$$\hat{O}_\lambda=\sum_\lambda \beta_\lambda Y_{\lambda 0}(\theta). \tag{2.86}$$

Now we need to know the matrix elements of the operator $\hat{O}_\lambda$ between the $|n\rangle=|I0\rangle$ and $|m\rangle=|I'0\rangle$ states of the ground states rotational band for the target nucleus, and are given as

$$O_{II'}=\sum_\lambda \beta_\lambda\sqrt{\frac{(2\lambda+1)(2I+1)(2I'+1)}{4\pi}}\begin{pmatrix} I & \lambda & I' \\ 0 & 0 & 0\end{pmatrix}^2. \tag{2.87}$$

This matrix is diagonalized to determine its eigenvalues and eigenvectors. Again, the nuclear matrix elements are evaluated in the same way as Eq. (2.62). Hence, the matrix elements of Eq. (2.85) are calculated as

$$\begin{aligned} V^N_{nm}(r) &= \langle I'0|V_N^{\mathrm{coup(rot)}}|I0\rangle - V_N(r)\delta_{I',I} \\ &= \sum_\mu \langle I'0|\mu\rangle\langle\mu|I0\rangle\frac{-V_0}{1+\exp[(r-R_0-R_T\lambda_\mu)/a]} \\ &\quad -V_N(r)\delta_{I',I}, \end{aligned} \tag{2.88}$$

where λ_μ and $|\mu\rangle$ are the eigenvalue and the eigenvector of the operator $\hat{O}_\lambda$ in Eq. (2.86), respectively. As before, we introduce the last term in Eq. (2.88) in order to avoid double counting of the diagonal components.

Coulomb coupling

For the Coulomb interaction, the coupling component is given by [see Eq. (2.69)]

$$V_C^{\rm coup(rot)}(r,\hat{O}_\lambda) = \sum_\lambda \frac{3Z_P Z_T e^2}{2\lambda+1}\frac{R_T^\lambda}{r^{\lambda+1}}\hat{O}_\lambda \tag{2.89}$$

with the operator $\hat{O}_\lambda$ is given by Eq. (2.86).

Using Eq. (2.87), the matrix elements for the rotational coupling potential of Eq. (2.89) reads

$$\begin{aligned} V_{nm}^C(r) &= \langle I'0|V_C^{\rm coup(rot)}|I0\rangle \\ &= \sum_\lambda \beta_\lambda \frac{3Z_P Z_T e^2}{2\lambda+1}\frac{R_T^\lambda}{r^{\lambda+1}}\sqrt{\frac{(2\lambda+1)(2I+1)(2I'+1)}{4\pi}} \\ &\quad \times \begin{pmatrix} I & \lambda & I' \\ 0 & 0 & 0 \end{pmatrix}^2 . \end{aligned} \tag{2.90}$$

As usual, the total coupling matrix elements are the sum of the nuclear [Eq. (2.88)] and Coulomb [Eq. (2.90)] coupling matrix elements.

To explain the difference between the vibrational and the rotational couplings, let us consider a system coupled to a ground state rotational band up to 2^+ state of the target nucleus which has a quadrupole deformation β_2. The wave function for the $|I0\rangle$ state in the ground state rotational band is given by $|I0\rangle = Y_{I0}$. Thus, the matrix elements of the operator in Eq. (2.87) is given by

$$O_{ij} = \frac{1}{\sqrt{4\pi}}\begin{pmatrix} 0 & \beta_2 \\ \beta_2 & 2\sqrt{5}\beta_2/7 \end{pmatrix} . \tag{2.91}$$

In obtaining this matrix elements, we truncate the ground states of the rotational bands up to 2^+ state. One of the main differences between the rotational coupling matrix [Eq. (2.91)] and the vibrational coupling matrix [Eq. (2.78)] is that the former has a diagonal component which is proportional to the deformation parameter β_2. This is known as the '*reorientation effect*'. This effect has been used in the Coulomb excitation experiment in order to determine the sign of the deformation parameter [39].

2.6 Scaling property

The scaling property is mainly used in order to extract barrier distributions from quasi-elastic scattering experimental data [2,3]. This scaling property will also be used in our analyses since the available experimental data and Coulomb barrier heights that are used in this thesis require the calculations to be scaled accordingly.

In order to properly interpret transmission and reflection probabilities by the potential barrier as fusion and scattering, respectively, the collision should occur at an angle $\theta = 180^\circ$ (i.e. head-on collision). In a real experiment, it is basically impossible to measure the scattered elastic function at angle $\theta = 180^\circ$. One of the advantages of quasi-elastic scattering over fusion is that different scattering angles correspond to different angular momenta. This means that one can correct the effect of angular momentum by shifting the energy by an amount equal to the centrifugal potential. By estimating the centrifugal potential at the Coulomb turning point r_C, the effective energy is given by [2, 3]

$$E_{\text{eff}} \sim E - \frac{\lambda_C^2 \hbar^2}{2\mu r_C^2} = 2E \frac{\sin(\theta/2)}{1 + \sin(\theta/2)}, \tag{2.92}$$

where the definition of r_C with

$$E = \frac{Z_P Z_T e^2}{r_C} + \frac{\lambda_C^2 \hbar^2}{2\mu r_C^2} \tag{2.93}$$

has been used. λ_C is the angular momentum and is given by $\lambda_C = \eta \cot(\theta/2)$, where η is the Sommerfeld parameter. One can therefore expect that the function $d\sigma_{\rm el}/d\sigma_R$ (which is the ratio of the elastic to the Rutherford cross section) evaluated at an angle θ with energy E corresponds to the same function evaluated at scattering angle of 180° with effective energy given by Eq. (2.92).

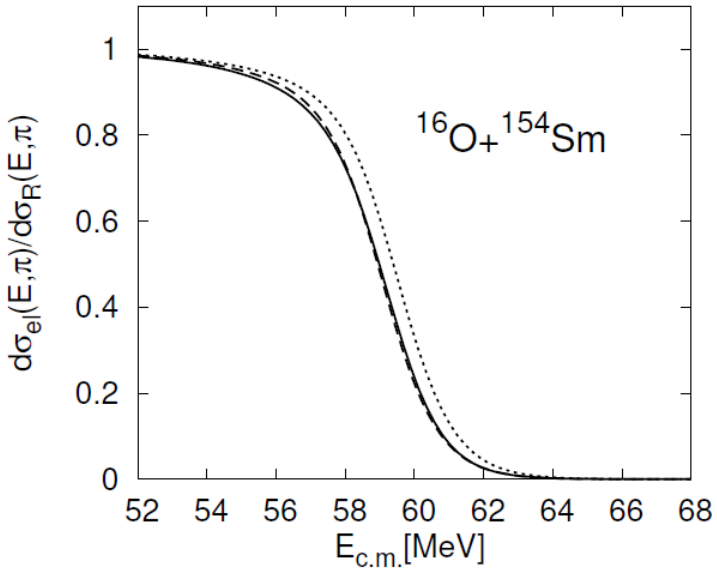

Figure 2.6: Comparison of the $d\sigma_{\rm el}/d\sigma_R$ evaluated at two different angles for ^{16}O+^{154}Sm reaction. The solid line is for $\theta = \pi$, while the dotted line is for $\theta = 160°$. The dashed line is the same as the dotted line, but the energy is shifted by an amount equals to the centrifugal potential evaluated at the distance of the closest approach of the Rutherford trajectory. Taken from Hagino and Rowley [3].

In order to check the validity of the scaling property of quasi-elastic scattering, we compare the function $d\sigma_{\rm el}/d\sigma_R$ for ^{16}O+^{154}Sm system obtained at two different scattering angles (see Fig. 2.6). The solid line is evaluated at $\theta = \pi$, while the dotted line is evaluated at $\theta = 160°$. The dashed line is the same as the dotted line, but the energy is shifted by $E_{\rm eff} - E$. It can be seen that the scaling works very well at energies both below and above the Coulomb barrier

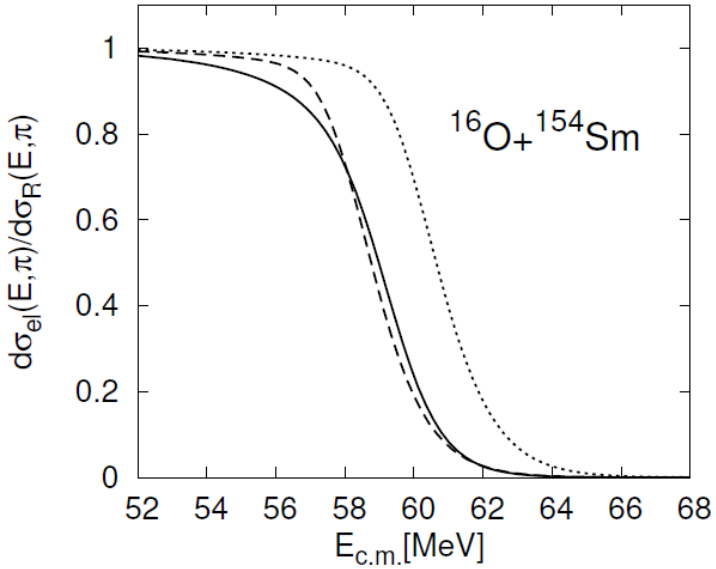

Figure 2.7: The same as Fig 2.6 but for $\theta = 140°$. Taken from Hagino and Rowley [3].

height.

However, if one uses a smaller scattering angle, the scaling becomes less good. This can be seen in Fig. 2.7 where the dashed line shows the scaling property for $\theta = 140°$. Therefore, in planning the experiment (especially if it combines data taken by detectors at different angles), this effect should be carefully taken into consideration. Besides, it is well known that the elastic cross section would display the Fresnel oscillation at smaller angles. It is important to minimize the effect of the Fresnel oscillation by choosing appropriate detector angles.

Chapter 3

Analysis of the nuclear potential for heavy-ion systems through large-angle quasi-elastic scattering at deep sub-barrier energies

3.1 Introduction

In Chapter 1, we have discussed that large-angle quasi-elastic scattering is a suitable method to study the nuclear potential. Recently, several studies have been done to investigate the nuclear potential (in particular the surface diffuseness parameter) for heavy-ion systems through large-angle quasi-elastic scattering [11–13].

Nuclear potential of the Woods-Saxon form [see Eq. (2.3)], which is described by the potential depth V_0, the radius parameter r_0, and the diffuseness parameter a, is widely used in the analyses of nuclear collisions. Throughout

this thesis, we assume that the nuclear potential has a Woods-Saxon form. As shown in Section 2.1, the diffuseness parameter determines the characteristic of the nuclear potential at the surface region. A diffuseness parameter of around 0.63 fm is widely accepted [40]. This has been supported by recent studies such as by Gasques *et al.* [11] and Evers *et al.* [13], where both studies performed analyses on the diffuseness parameter using the experimental data of large-angle quasi-elastic scattering. However, relatively higher diffuseness parameters are required in order to fit fusion data, as shown by Newton *et al.* [7] for example. The cause of the discrepancy is still not well understood.

At deep sub-barrier energies, channel couplings weakly influence a nucleus-nucleus collision. Thus, channel couplings can be justifiably omitted in the analyses at deep sub-barrier energies. According to Gasques *et al.* [11], this is true only for spherical collision systems. All of our studied systems here are spherical. Therefore, neglecting channel couplings at deep sub-barrier energies should be acceptable. The main advantage of performing analyses at deep sub-barrier energies is that the calculations are greatly simplified since channel couplings can be neglected. This, in turn, could avoid numerical instabilities in the calculations that would affect the accuracy of the analyses.

Washiyama *et al.* [12] has pointed out that at deep sub-barrier energies, deviation of the elastic cross sections from the Rutherford cross sections at backward angles is sensitive to the surface region of the nuclear potential, particularly to the surface diffuseness parameter. Thus, an accurate value of the diffuseness parameter could be determined by using large-angle quasi-elastic scattering experimental data at deep sub-barrier energies. However, this could also represent a drawback since small errors or uncertainties in the experimental data could affect the deduced value of the diffuseness parameter significantly. Nonetheless, it is certainly attractive and advantageous to study the nuclear potential through large-angle quasi-elastic scattering at deep sub-barrier ener-

gies.

In this chapter, we investigate the nuclear potential, in particular the diffuseness parameter, for some heavy-ion systems, namely ^{48}Ti, ^{54}Cr, ^{56}Fe, ^{64}Ni, and ^{70}Zn + ^{208}Pb systems through large-angle quasi-elastic scattering at deep sub-barrier energies. The procedures of the analysis are explained in Section 3.2. The results and subsequent discussion are presented in Sections 3.3 and 3.4, respectively. The study is then summarized in Section 3.5.

3.2 Procedures

The calculations are performed using CQEL [41], which is a modified version of the computer code CCFULL [10]. Washiyama *et al.* [12] defined a deep sub-barrier energy region as the region with $d\sigma_{\rm qel}/d\sigma_R \geq 0.94$, where $d\sigma_{\rm qel}/d\sigma_R$ is the ratio of the quasi-elastic to the Rutherford cross sections. Here, we also use the same definition.

As shown later in Section 3.3, relatively low values of the diffuseness parameter are needed in order to analyze the experimental data at deep sub-barrier energies. Low values of the diffuseness parameter would produce significant numerical instabilities in the calculations when channel couplings are taken into account, which is unwanted. More importantly, since channel couplings can be neglected at deep sub-barrier energies, we only perform single-channel calculations for the analyses at deep sub-barrier energies.

In order to find the best fitted value of the diffuseness parameter in comparison with the experimental data, the chi square method χ^2 is used. The experimental data are taken from Mitsuoka *et al.* [21]. The data with $d\sigma_{\rm qel}/d\sigma_R > 1$ are excluded from the fitting procedures, but included in the figures for completeness. This is because theoretically, it is clear that $d\sigma_{\rm qel}/d\sigma_R$ cannot be larger than unity.

In our calculations, the nuclear potential has a real and an imaginary com-

ponents. Both components are assumed to have Woods-Saxon forms. The purpose of the imaginary component is to simulate the compound nucleus formation. We use an imaginary potential with a potential depth of 30 MeV, a radius parameter of 1.0 fm, and a diffuseness parameter of 0.3 fm. The calculations are insensitive to the imaginary parameters provided that the imaginary potential is confined inside the Coulomb barrier. For the real part of the nuclear potential, the radius parameter r_0 is taken to be 1.22 fm. The value of potential depth V_0 depends on the diffuseness parameter such that the Coulomb barrier height V_B for each system is reproduced. The calculations are carried out at scattering angle of $\theta_{\text{c.m.}} = 170^{\circ}$. The radii of the target and projectile are taken as $R_T = r_T A_T^{1/3}$ and $R_P = r_P A_P^{1/3}$, respectively, where r_T and r_P are taken to be 1.2 fm in order to be consistent with the deformation parameters taken from Kibedi and Spears [42], and Raman *et al.* [43]. In order to ensure that the calculations are properly scaled according to the available experimental data, the calculated ratio of the quasi-elastic to the Rutherford cross sections are analyzed and plotted as functions of effective energies [2, 3], as explained in Section 2.6.

Even though coupled-channels calculations are not employed in determining the best fitted diffuseness parameters at deep sub-barrier energies, they are used in order to investigate the effects of some calculational inputs on the resulting diffuseness parameters. In order to perform coupled-channels calculations, the excited states of the colliding nuclei must be considered. The properties of the single-phonon excitation and the deformation parameter for each nucleus are shown in Table 3.1, which are taken from Kibedi and Spears [42], and Raman *et al.* [43].

Table 3.2 shows the coupling scheme used in the coupled-channels calculations and the Coulomb barrier height for each system. For ^{54}Cr, ^{56}Fe, and ^{64}Ni + ^{208}Pb systems, we use triple-quadrupole phonon and triple-octupole phonon

Table 3.1: The properties of the single-phonon excitation for each nucleus. I, π, $\hbar\omega$, and β are the angular momentum, parity, excitation energy and dynamical deformation parameter of the phonon state, respectively. The properties for ^{208}Pb are taken from Kibedi and Spears [42], while the properties for ^{48}Ti, ^{54}Cr, ^{56}Fe, ^{64}Ni, and ^{70}Zn are taken from Raman *et al.* [43].

Nucleus	I^π	$\hbar\omega$ (MeV)	β
^{208}Pb	3^-	2.164	0.110
^{48}Ti	2^+	0.983	0.269
^{54}Cr	2^+	0.834	0.250
^{56}Fe	2^+	0.846	0.239
^{64}Ni	2^+	1.346	0.179
^{70}Zn	2^+	0.884	0.228

excitations in the projectiles and the targets, respectively. As found by Muhammad Zamrun F. and Abu Kassim [44] for ^{54}Cr + ^{208}Pb system, we find that the mentioned coupling scheme fits the experimental data better than double-quadrupole phonon excitations in the projectiles and triple-octupole phonon excitations in the targets as found by Muhammad Zamrun F. *et al.* [45]. For ^{48}Ti + ^{208}Pb and ^{70}Zn + ^{208}Pb systems, the coupling schemes are taken to be same as found by Muhammad Zamrun F. *et al.* [45].

Table 3.2: The coupling scheme used in coupled-channels calculations and the Coulomb barrier height V_B for each system (taken from Muhammad Zamrun F. *et al.* [45]). For the coupling scheme, n_P represents the number of quadrupole phonon excitation in the projectile, while n_T represents the number of octupole phonon excitation in the target.

System	Coupling scheme [n_P,n_T]	V_B (MeV)
^{48}Ti + ^{208}Pb	[1,3]	190.50
^{54}Cr + ^{208}Pb	[3,3]	205.50
^{56}Fe + ^{208}Pb	[3,3]	222.50
^{64}Ni + ^{208}Pb	[3,3]	236.25
^{70}Zn + ^{208}Pb	[2,3]	249.30

3.3 Results

^{48}Ti + ^{208}Pb system

The best fitted value of the diffuseness parameter for ^{48}Ti + ^{208}Pb system obtained through a single-channel calculation is 0.40 fm. The calculated ratio of the quasi-elastic to the Rutherford cross sections for ^{48}Ti + ^{208}Pb system using $a = 0.40$ fm is shown by the solid line in Fig. 3.1. The χ^2 value for the best fitted diffuseness parameter in comparison with the experimental data is 0.20. The Coulomb barrier height for ^{48}Ti + ^{208}Pb system is 190.5 MeV [45] and the potential depth V_0 that is required to reproduce the Coulomb barrier height is 303.5 MeV. It is clear that the best fitted diffuseness parameter is rather low compared to the standard value of around 0.63 fm.

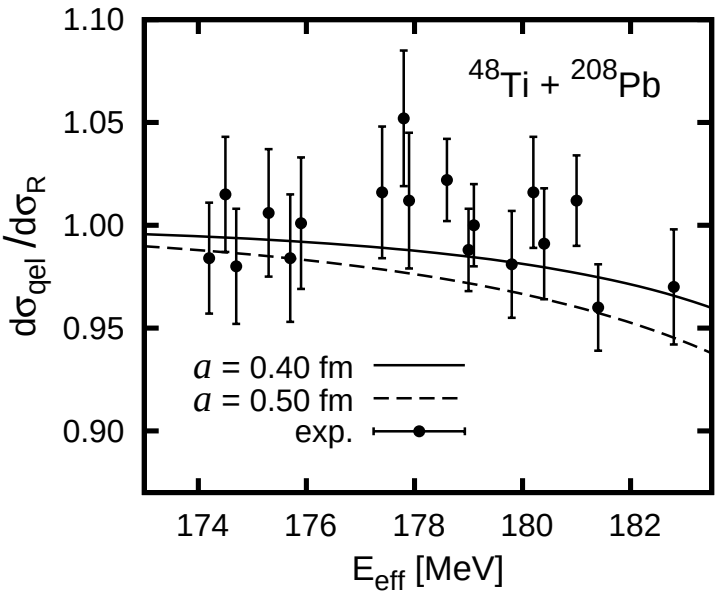

Figure 3.1: The ratio of the quasi-elastic to the Rutherford cross sections for ^{48}Ti + ^{208}Pb system at deep sub-barrier energies. The experimental data (taken from Mitsuoka *et al.* [21]) with $d\sigma_{\rm qel}/d\sigma_R \geq 0.94$ are shown and denoted by dots with error bars. The best fitted diffuseness parameter is 0.40 fm, and shown by the solid line. The calculation using $a = 0.50$ fm is shown for comparison.

^{54}Cr + ^{208}Pb system

For ^{54}Cr + ^{208}Pb system, the best fitted diffuseness parameter obtained through a single-channel calculation is 0.56 fm. The best fitted diffuseness parameter can be considered to be in a good agreement with the standard value. The χ^2 value for $a = 0.56$ fm in comparison with the experimental data is 0.18. The required potential depth V_0 to reproduce the Coulomb barrier height is 114.5 MeV. The calculated ratio of the quasi-elastic to the Rutherford cross sections for ^{54}Cr + ^{208}Pb system using $a = 0.56$ fm is shown by the solid line in Fig. 3.2.

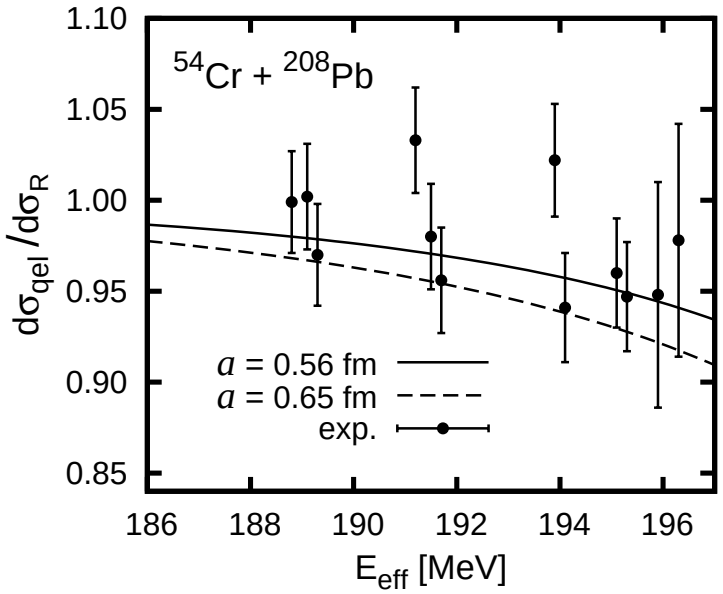

Figure 3.2: The ratio of the quasi-elastic to the Rutherford cross sections for ^{54}Cr + ^{208}Pb system at deep sub-barrier energies. The experimental data (taken from Mitsuoka *et al.* [21]) with $d\sigma_{\rm qel}/d\sigma_R \geq 0.94$ are shown and denoted by dots with error bars. The best fitted diffuseness parameter is 0.56 fm, and shown by the solid line. The calculation using $a = 0.65$ fm is shown for comparison.

^{56}Fe + ^{208}Pb system

The best fitted diffuseness parameter for ^{56}Fe + ^{208}Pb system using a single-channel procedure is 0.38 fm, with $\chi^2 = 0.17$. The plot for the best fitted diffuseness parameter is shown by the solid line in Fig. 3.3. The obtained

diffuseness parameter is considerably lower than the standard value. The potential depth V_0 that is required to reproduce the Coulomb barrier height is 355.5 MeV.

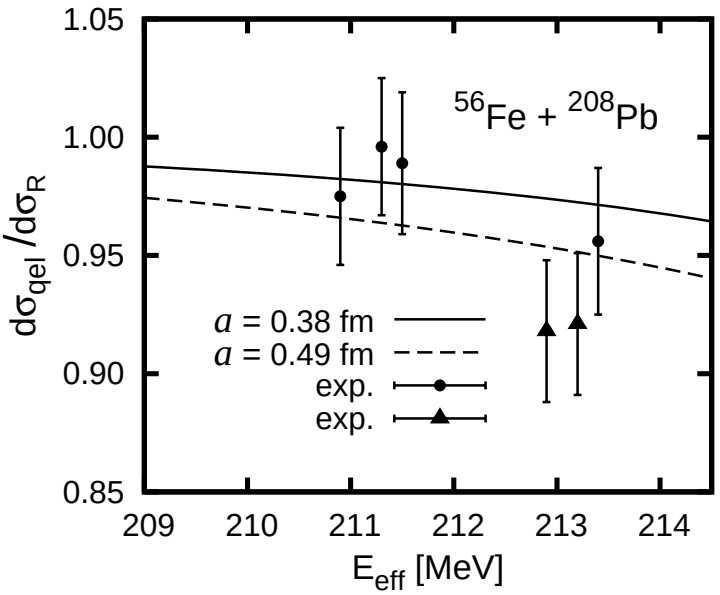

Figure 3.3: The ratio of the quasi-elastic to the Rutherford cross sections for ^{56}Fe + ^{208}Pb system at deep sub-barrier energies. The experimental data (taken from Mitsuoka *et al.* [21]) with $d\sigma_{\rm qel}/d\sigma_R \geq 0.94$ and $0.94 > d\sigma_{\rm qel}/d\sigma_R \geq 0.90$ are denoted by dots and triangles with error bars, respectively. The best fitted diffuseness parameters when fitting using the data with $d\sigma_{\rm qel}/d\sigma_R \geq 0.94$ and $d\sigma_{\rm qel}/d\sigma_R \geq 0.90$ are 0.38 fm and 0.49 fm, respectively, shown by the solid line and the dashed line, respectively.

It can be seen in Fig. 3.3 that there are only four data points available when the analysis is performed using the experimental data with $d\sigma_{qel}/d\sigma_R \geq 0.94$. If we include the experimental data with $d\sigma_{\rm qel}/d\sigma_R \geq 0.90$ in the fitting, the best fitted diffuseness parameter obtained using a single-channel calculation is 0.49 fm, with $\chi^2 = 0.76$ and $V_0 = 156$ MeV in order to reproduce the Coulomb barrier height. This is shown by the dashed line in Fig. 3.3. This value of diffuseness parameter is still quite low compared to the standard value.

^{64}Ni + ^{208}Pb system

For ^{64}Ni + ^{208}Pb system, the best fitted diffuseness parameter obtained using a single-channel calculation is 0.32 fm. This value is significantly lower than the standard value. The χ^2 value for the best fitted diffuseness parameter in comparison with the experimental data is 0.06. The potential depth V_0 that is required in order to reproduce the Coulomb barrier height is 752 MeV, which is relatively high. The calculated ratio of the quasi-elastic to the Rutherford cross sections for the best fitted diffuseness parameter is shown by the solid line in Fig. 3.4.

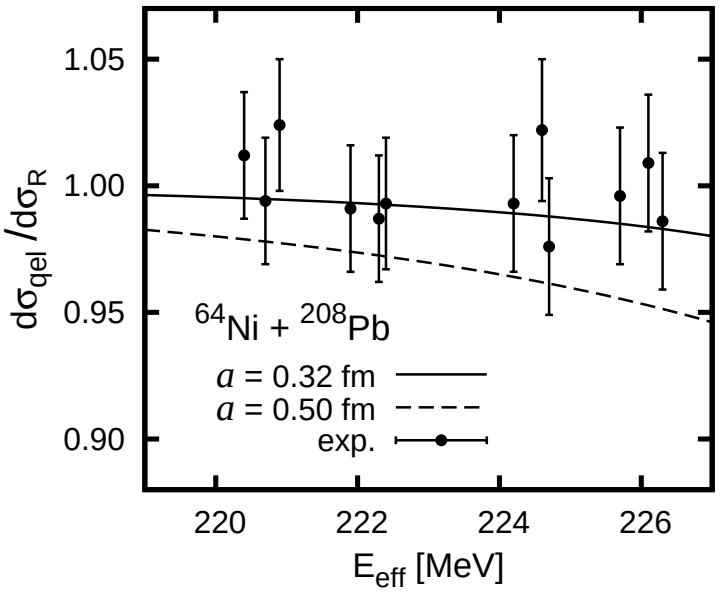

Figure 3.4: The ratio of the quasi-elastic to the Rutherford cross sections for ^{64}Ni + ^{208}Pb system at deep sub-barrier energies. The experimental data (taken from Mitsuoka *et al.* [21]) with $d\sigma_{\rm qel}/d\sigma_R \geq 0.94$ are shown and denoted by dots with error bars. The best fitted diffuseness parameter is 0.32 fm, denoted by the solid line. The calculation using $a = 0.50$ fm is shown for comparison.

^{70}Zn + ^{208}Pb system

For ^{70}Zn + ^{208}Pb system, the best fitted diffuseness parameter obtained through a single-channel calculation is 0.42 fm, shown by the solid line in Fig. 3.5. This value is considerably lower than the standard value. The value of χ^2

in comparison with the experimental data is 0.48. The potential depth V_0 that is required to reproduce the barrier height is 302.5 MeV.

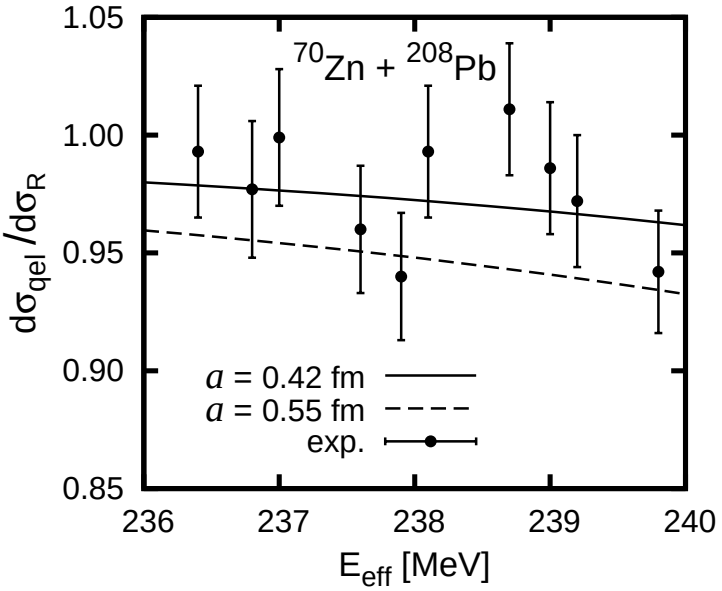

Figure 3.5: The ratio of the quasi-elastic to the Rutherford cross sections for ^{70}Zn + ^{208}Pb system at deep sub-barrier energies. The experimental data (taken from Mitsuoka *et al.* [21]) with $d\sigma_{\rm qel}/d\sigma_R \geq 0.94$ are shown and denoted by dots with error bars. The best fitted diffuseness parameter is 0.42 fm, denoted by the solid line. The calculation using $a = 0.55$ fm is shown for comparison.

3.4 Discussion

Figure 3.6 below summarizes the best fitted diffuseness parameters obtained at sub-barrier energies as functions of charge products of the target and projectile. For ^{56}Fe + ^{208}Pb system, the best fitted diffuseness parameter obtained using the experimental data with $d\sigma_{qel}/d\sigma_R \geq 0.94$ is accepted, even though there are only four data points available. This is because channel couplings might be required in order to analyze the experimental data with $0.94 > d\sigma_{qel}/d\sigma_R \geq 0.90$.

It can be seen from Fig. 3.6 that the best fitted diffuseness parameters obtained at deep sub-barrier energies for all of the studied systems are considerably lower than the standard value of around 0.63 fm, except for ^{56}Cr + ^{208}Pb

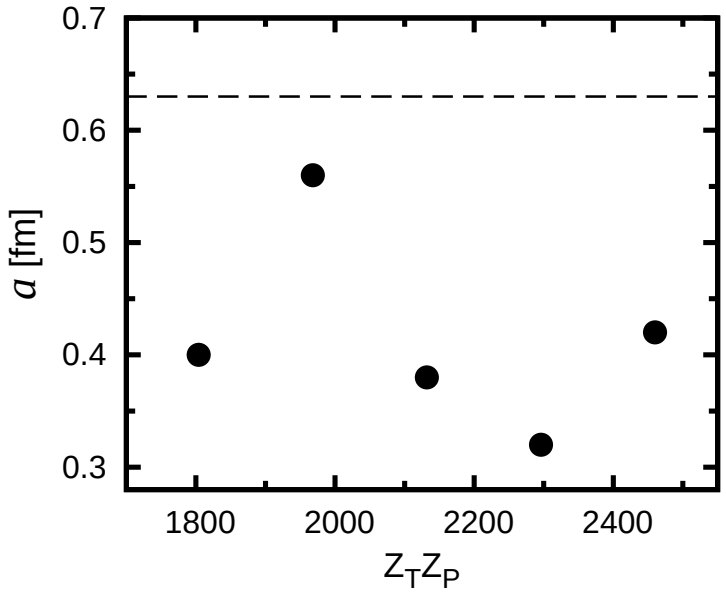

Figure 3.6: The best fitted diffuseness parameters obtained at deep sub-barrier energies as functions of charge products of the target and projectile $Z_T Z_P$. The dashed line indicates $a = 0.63$ fm.

system, where the best fitted diffuseness parameter can be considered to be in a satisfactory agreement with (but still lower than the) the standard value. From Fig. 3.6, it is also difficult to deduce if there is any relationship between the best fitted diffuseness parameter obtained at deep sub-barrier energies and the charge product of the target and projectile.

Effect of Coulomb barrier height

In order to find the cause for the low values of the diffuseness parameter, the effects of inputs need to be investigated. According to Washiyama *et al.* [12], a slightly higher Coulomb barrier height would lead to a very small increase in the best fitted diffuseness parameter. We also investigate regarding this matter and find the same conclusion. To illustrate this, Figs. 3.7 and 3.8 compare the best fitted diffuseness parameters at deep sub-barrier energies for ^{48}Ti, and ^{64}Ni + ^{208}Pb systems using $V_B = 190.5$ MeV and $V_B = 236.25$ MeV as originally used, respectively, with $V_B = 191.5$ MeV and $V_B = 237.25$ MeV,

respectively. For increases of 1 MeV in the barrier height from the values that are originally used, the best fitted diffuseness parameters increase by 0.02 fm, to $a = 0.42$ fm and $a = 0.34$ fm for ^{48}Ti, and ^{64}Ni + ^{208}Pb systems, respectively. The reason for this can be easily understood, where a slight increase or decrease in the barrier height would slightly shift the line of the original best fitted diffuseness parameter from the best fitted line. Hence, a slightly higher or lower diffuseness parameter is required to compensate this. Therefore, slight variations or uncertainties in the values of the barrier height can be dismissed as a cause for the low values of the diffuseness parameter obtained at deep sub-barrier energies.

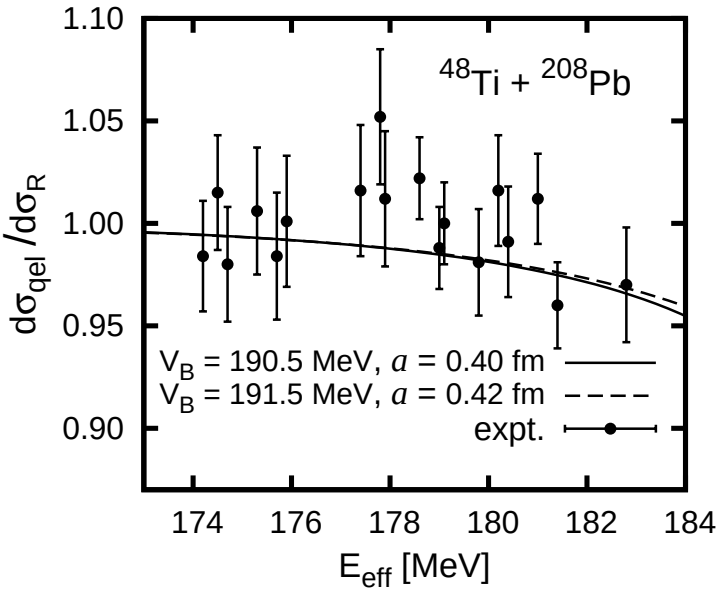

Figure 3.7: Comparison of the ratio of the quasi-elastic to the Rutherford cross sections at deep sub-barrier energies for ^{48}Ti + ^{208}Pb system using two different values of the Coulomb barrier height V_B. When $V_B = 190.5$ MeV and $V_B = 191.5$ MeV are used, the best fitted diffuseness parameters are 0.40 fm and 0.42 fm, respectively.

Effect of r_T and r_P

According to Gasques *et al.* [11], a higher value of the target radius parameter r_T would lead to a higher best fitted diffuseness parameter for a deformed system, but has a negligible effect on a spherical system. We check and find that

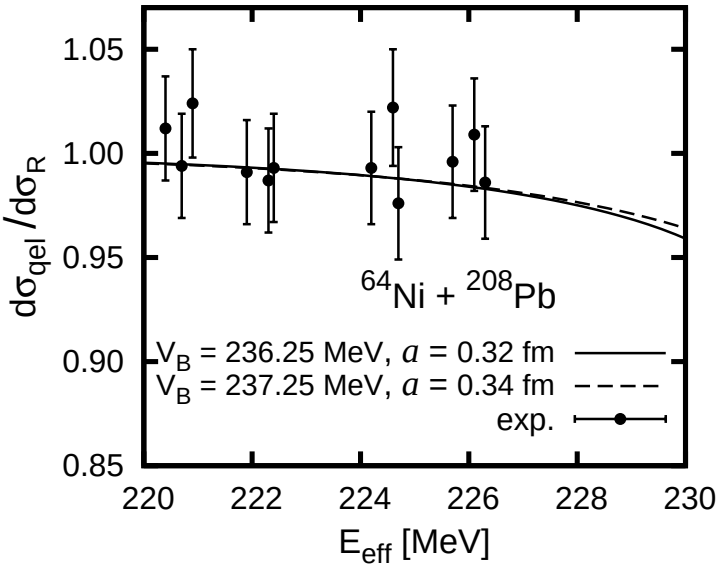

Figure 3.8: Comparison of the ratio of the quasi-elastic to the Rutherford cross sections at deep sub-barrier energies for ^{64}Ni + ^{208}Pb system using two different values of the Coulomb barrier height V_B. When $V_B = 236.25$ MeV and $V_B = 237.25$ MeV are used, the best fitted diffuseness parameters are 0.32 fm and 0.34 fm, respectively.

the effect of increasing the target radius parameters r_T and/or the projectile radius parameter r_P on the calculated quasi-elastic cross sections is negligible when using single-channel calculations. This is illustrated by Fig. 3.9, where the two calculations using two different values of the r_T and r_P are basically indistinguishable. This is comprehensible since changing the r_T and the r_P, which would change the radii of the colliding nuclei, mainly affect the deformation parameters β_λ [see Eq. (2.55)], which are not used in single-channel calculations. An increase in the radii of the colliding nuclei alone basically does not affect the calculated cross sections as long as the mass and the atomic numbers of the colliding nuclei are still the same.

In order to make a more comprehensive study on the effects of the r_T and the r_P on the deduced diffuseness parameters, we vary the r_T and the r_P using coupled-channels calculations. The ranges of the r_T and the r_P are generally likely to lie between 1.06 fm and 1.2 fm [11].

Figures 3.10 to 3.14 show comparisons between the calculated ratios of the

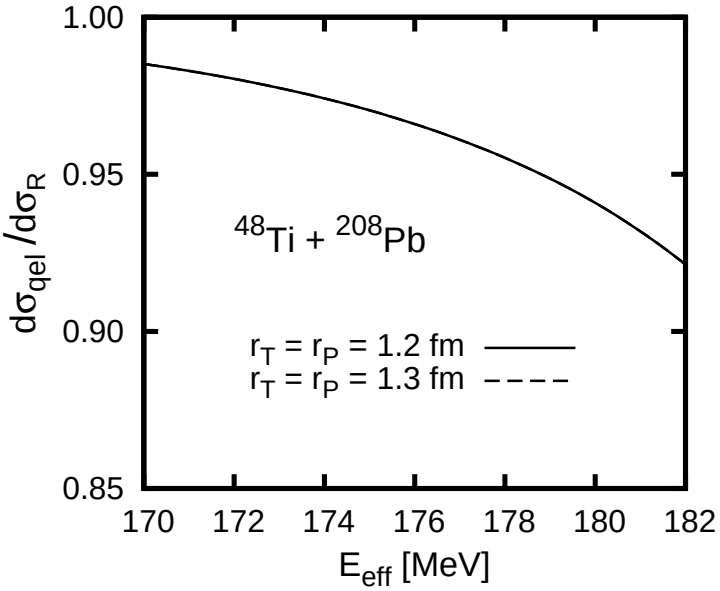

Figure 3.9: The calculated ratio of the quasi-elastic to the Rutherford cross sections at deep sub-barrier energies for ^{48}Ti + ^{208}Pb system using $r_T = r_P = 1.2$ fm (solid line) and $r_T = r_P = 1.3$ fm (dashed line). The calculations are performed using single-channel procedures, with $a = 0.63$ fm. The two calculations are indistinguishable.

quasi-elastic to the Rutherford cross sections for all of the studied systems using $r_T = r_P = 1.2$ fm and $r_T = r_P = 1.3$ fm (which is quite well above the mentioned range). All of the calculations are performed using $a = 0.63$ fm and the coupling schemes as shown in Table 3.2. When using $r_T = r_P = 1.3$ fm, the deformation parameters are modified according to Eq. (2.55), with β_2 for ^{48}Ti, ^{54}Cr, ^{56}Fe, ^{64}Ni, and ^{70}Zn are 0.229, 0.213, 0.204, 0.153, and 0.194, respectively, while $\beta_3 = 0.087$ for ^{208}Pb.

It can be seen from Figs. 3.10 to 3.14 that increasing the r_T and the r_P from 1.2 fm to 1.3 fm would give small increases in the calculated quasi-elastic cross sections at deep sub-barrier energies for all of the studied systems when coupled-channels calculations are used, particularly at the highest energies of the deep sub-barrier region. It is known that the r_T and r_P affect the deformation parameters, which, in turn, affect channel couplings. Since channel couplings are weak at deep sub-barrier energies, the effects of varying the r_T and r_P on

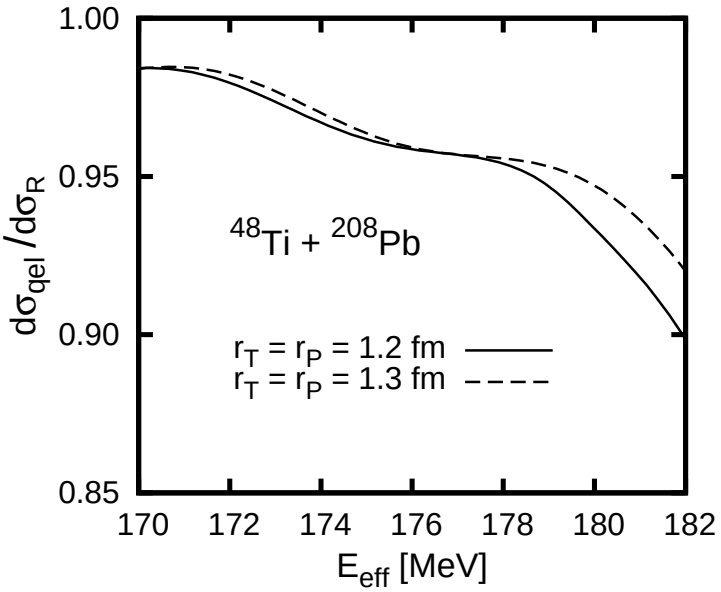

Figure 3.10: Comparison between the calculated ratio of the quasi-elastic to the Rutherford cross sections at deep sub-barrier energies for ^{48}Ti + ^{208}Pb system using $r_T = r_P = 1.3$ fm (dashed line) and $r_T = r_P = 1.2$ fm (solid line). The calculations are performed using $a = 0.63$ fm and coupled-channels procedures with the coupling scheme as in Table 3.2.

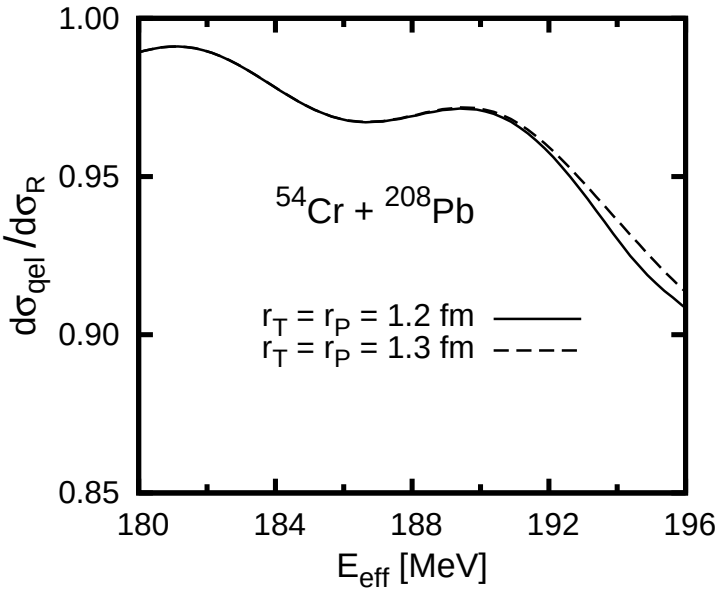

Figure 3.11: The same as Fig. 3.9 but for ^{54}Cr + ^{208}Pb system.

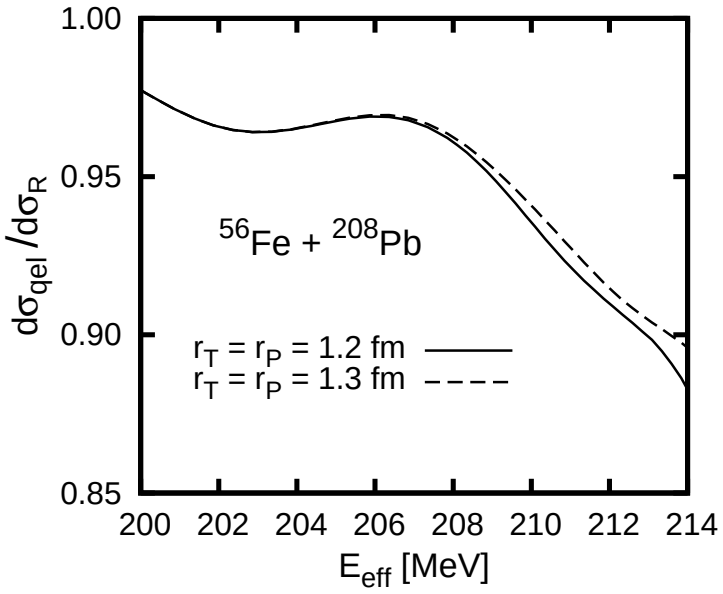

Figure 3.12: The same as Fig. 3.9 but for ^{56}Fe + ^{208}Pb system.

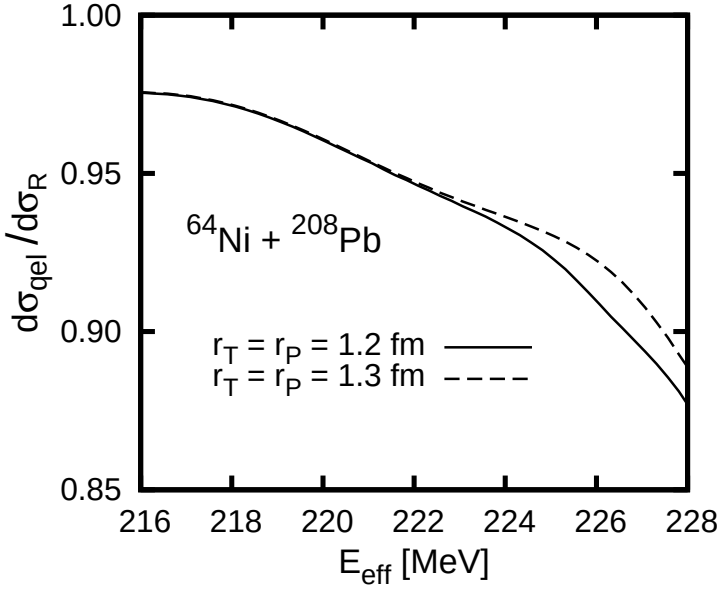

Figure 3.13: The same as Fig. 3.9 but for ^{64}Ni + ^{208}Pb system.

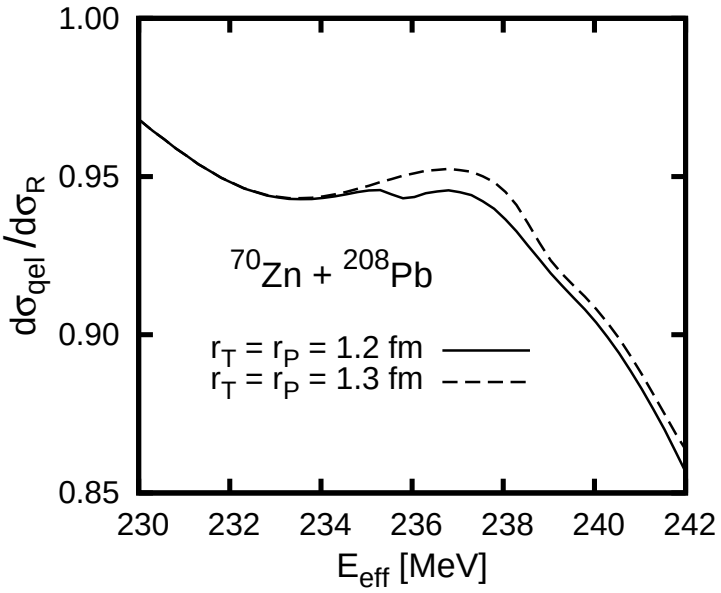

Figure 3.14: The same as Fig. 3.9 but for ^{70}Zn + ^{208}Pb system.

the calculated quasi-elastic cross sections are small at those energies.

Since increasing the r_T and r_P increases the calculated quasi-elastic cross sections when coupled-channels calculations are used, this would in turn increase the best fitted diffuseness parameters. In order to explicitly see the effect of varying the r_T and r_P on the deduced diffuseness parameters at deep sub-barrier energies, we try to find the best fitted diffuseness parameter for ^{48}Ti + ^{208}Pb system at deep sub-barrier energies using $r_T = r_P = 1.3$ fm and coupled-channels calculations. It is found that the best fitted parameter is still lower than 0.41 fm. The χ^2 values for diffuseness parameters lower than 0.41 fm cannot be properly determined since the calculations with diffuseness parameters lower than 0.41 fm produce significant numerical instabilities when channel couplings are introduced.

It is not surprising the best fitted diffuseness parameter obtained using $r_T = r_P = 1.3$ fm and a coupled-channels calculation is approximately the same as the best fitted diffuseness parameter obtained using $r_T = r_P = 1.2$ fm and a single-channel calculation. This is because increases in the quasi-elastic cross

sections at deep sub-barrier energies when using larger r_T and r_P can only be achieved through coupled-channels calculations. However, a coupled-channels calculation would produce slightly lower quasi-elastic cross sections than a single-channel calculation for the same r_T and r_P. Therefore, the effects of using the channel couplings and using higher r_T and r_P on the calculated quasi-elastic cross sections at deep sub-barrier energies basically cancel out each other. Figure 3.15 shows a comparison between single-channel and coupled-channels calculations for ^{48}Ti + ^{208}Pb system at deep sub-barrier energies. It can be seen that for the same inputs, the effect of channel couplings is to slightly reduce the quasi-elastic cross sections at deep sub-barrier energies.

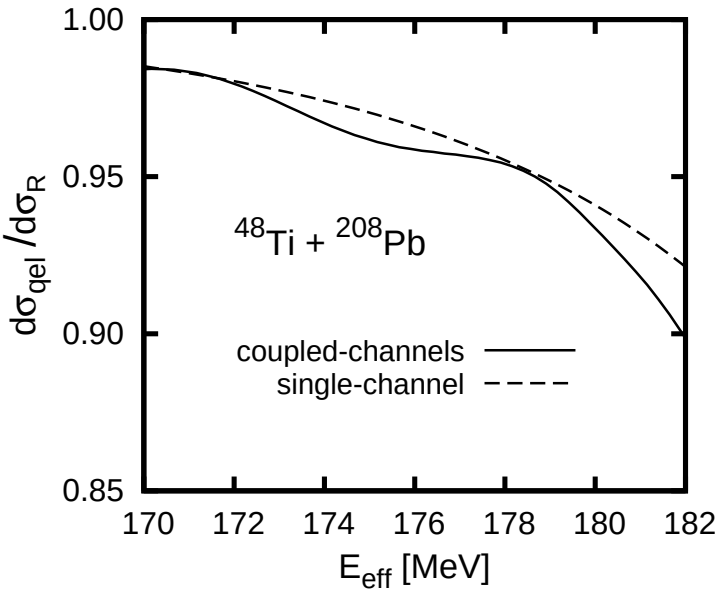

Figure 3.15: Comparison between the calculated ratio of the quasi-elastic to the Rutherford cross sections at deep sub-barrier energies for ^{48}Ti + ^{208}Pb system using single-channel and coupled-channels calculations. Both calculations are performed using the same inputs with $a = 0.63$ fm, and $r_T = r_P = 1.2$ fm. The coupled-channel calculation uses the coupling scheme as in Table 3.2.

Furthermore, the ranges of the r_T and the r_P are generally likely to lie between 1.06 fm and 1.2 fm [11]. So, the value that is used here (which is 1.2 fm) can be considered to be relatively high. Hence, it is unlikely that the values of the r_T and r_P that are used in this study contribute to the relatively low

values of the diffuseness parameter obtained at deep sub-barrier energies.

São Paulo potential

From the results, it seems that there is an effect that is not considered in a typical nucleus-nucleus collision (and also in our study here) that could be the reason for the diffuseness parameters at deep sub-barrier energies to appear considerably lower than the standard value in general. It was shown that the effect of Pauli nonlocality would make the nuclear potential to be energy dependent [46–48], which might explain the relatively low diffuseness parameters obtained at deep sub-barrier energies. For nucleus-nucleus collisions, the nuclear potential due to Pauli nonlocality (called the São Paulo potential V_{S-P}) is given by [46–48]

$$V_{S-P}(r;E) = V_F(r)\exp\{-\varrho[E - V_C(r) - V_{S-P}(r;E)]\}, \tag{3.1}$$

where V_F is the nuclear potential without the effect of Pauli nonlocality, V_C is the Coulomb potential, E is the relative motion energy, and ϱ is a system-dependent constant.

For heavy-ion systems, the São Paulo potential should be negligible at near-barrier energies since $E \approx V_C(R_B)+V_{S-P}(R_B)$ [48], (where R_B is the location of the barrier height) and ϱ is very small [47]. From first impression, it seems that the results of this study are negligibly affected by the effect of Pauli nonlocality.

However, let us still consider this effect. In order to employ the nuclear potential of Eq. (3.1), we need the values of ϱ for our studied systems, which we do not know. For heavy-ion systems, when V_C+V_{S-P} is small in comparison with E, we can expand Eq. (3.1) and write [47]

$$V_{S-P}(r;E) \approx V_F(r)[1 - \varrho E]. \tag{3.2}$$

From Eq. (3.2), Chamon *et al.* [47] showed that

$$V_{S-P}(r;E) = V_F(r)\left[1 - \Lambda\frac{E_{\rm lab}}{A_P}\right], \tag{3.3}$$

where Λ is a system-independent constant equals to 0.0086 MeV^{-1}. Equation (3.3) enables us to explicitly investigate the effect of Pauli nonlocality in our study. A quick check for ^{56}Fe + ^{208}Pb system at E = 212 MeV ($E_{\rm lab}$ = 269 MeV) gives $V_{S-P} = 0.96V_F$. It is important to remember that in this present study, the actual V_{S-P} should be less energy dependent than Eq. (3.3) since $V_C + V_{S-P}$ is not small compared to E. Hence, the actual ratio of V_{S-P}/V_F for ^{56}Fe + ^{208}Pb system at $E = 212$ MeV should be larger than 0.96 (i.e. closer to 1).

In order to explicitly see whether the nuclear potential based on Pauli nonlocality can explain our results or not, we replace the Woods-Saxon potential [Eq. (2.3)] with the São Paulo potential [Eq. (3.3)] in our calculations. The V_F should basically be the double folding potential. However, in order to serve our purpose which is to study the nuclear potential in the Woods-Saxon form, we use the Woods-Saxon form for the V_F in our calculations. Therefore, the São Paulo potential used in our calculations reads

$$V_{S-P}(r;E) = \frac{-V_0(1 - \Lambda E_{\rm lab}/A_P)}{1 + \exp\left[(r - R_0)/a\right]}. \tag{3.4}$$

As usual, the barrier height must be reproduced in the calculations. Hence, for the same diffuseness parameter, the V_0 when using the São Paulo potential [Eq. (3.4)] is higher than the V_0 when using purely the Woods-Saxon potential [Eq. (2.3)]. For example, for a = 0.59 fm, the São Paulo potential requires V_0 = 108.3 MeV while the Woods-Saxon potential requires V_0 = 103.6 MeV.

Figure 3.16 shows the results of our calculations for ^{56}Fe + ^{208}Pb system at deep sub-barrier energies. The differences between the quasi-elastic cross

sections obtained using the São Paulo potential and the Woods-Saxon potential for the same diffuseness parameter are very small. If all the plots in Fig. 3.16 are shown by lines, it is hard to distinguish between the plots using the São Paulo potential and the Woods-Saxon potential for the same diffuseness parameter.

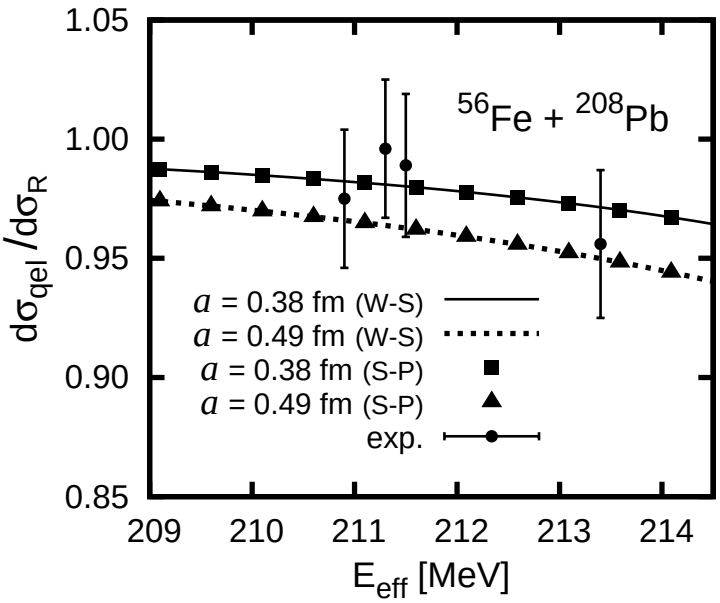

Figure 3.16: Same as Fig. 3.3. W-S and S-P denote the Woods Saxon potential [Eq. (2.3)] and the São Paulo potential [Eq. (3.4)], respectively. The plots using the Woods-Saxon potential (solid and dotted lines) are the same as in Fig. 3.3. The plots using the São Paulo potential shown by squares and triangles are obtained using single-channel calculations with $a = 0.38$ fm and $a = 0.49$ fm, respectively.

If the effect of Pauli nonlocality is able to explain the relatively low diffuseness parameter obtained at deep sub-barrier energies, then the best fitted diffuseness parameter should be consistent with the standard value when using the V_{S-P} [Eq. (3.4)]. However, we show that the V_{S-P} still produces a best fitted diffuseness parameter that is considerably lower than the standard value (practically the same as the best fitted diffuseness parameter when using purely the Woods-Saxon potential). In conclusion, we demonstrate that the effect of Pauli nonlocality is clearly negligible in the analyses at deep sub-barrier energies.

Effect of threshold anomaly

One of the well-known phenomena in the scattering of heavy-ions is the threshold anomaly [49]. This phenomenon is related to the variation of the real part of the nuclear potential due to a dispersion relation that arises from the causality principle [50, 51]. The dispersion relation takes the form [50, 51]

$$\Delta V_N(r;E) = \frac{P}{\pi}\int_0^\infty \frac{W_N(r;E')}{E'-E}dE', \tag{3.5}$$

where P denotes the "principal value", W_N is the imaginary part of the nuclear potential, and ΔV_N is the real part of the nuclear potential that depends on the imaginary part. The total real part of the nuclear potential can then be written as

$$V_N(r;E) = V_U(r;E) + \Delta V_N(r;E), \tag{3.6}$$

where V_U is the real component that varies at most slowly with energies E [50]. Hence, V_U can be regarded to be independent of E [49].

It is interesting to see whether the effect of threshold anomaly can account for the relatively low values of the diffuseness parameter obtained at deep sub-barrier energies. If the effect of threshold anomaly is present and influences the studied collisions, then the nuclear potentials obtained from the fittings of experimental data are equivalent to the potential on the left hand side of Eq. (3.6) [i.e.$V_N(r;E)$]. For the nuclear potential obtained through the fitting of experimental data, we can say that the energy E in Eq. (3.6) is the average energy of the experimental data points that are used in the fitting. Let us write the nuclear potential obtained at deep sub-barrier energies $V_{N(\mathrm{deep})}$ as

$$V_{N(\mathrm{deep})} = V_U + \Delta V_{N(\mathrm{deep})}, \tag{3.7}$$

where $\Delta V_{N(\mathrm{deep})}$ is the ΔV_N at the deep sub-barrier region, and V_U is the original

nuclear potential that is not affected by the threshold anomaly.

Unfortunately, we do not have the experimental data to determine W_N as a function of energy. Thus, the absolute value of $\Delta V_{N(\text{deep})}$ cannot be determined. However, if $|W_N|$ (where $W_N \leq 0$) rises rapidly as a function of energy over some energy range, the contribution to ΔV_N will be attractive ($\Delta V_N < 0$) in that same energy range [50]. For all nucleus-nucleus collisions, it is natural to think that $|W_N|$ (where $W_N \leq 0$) definitely rises from (almost) zero at energies well below the barrier height to some value at energies in the vicinity of the barrier height, and this value of $|W_N|$ is approximately maintained for all energies above the barrier height. This behavior of W_N has been shown by many studies [49, 50, 52, 53]. Therefore, generally speaking, the integral of Eq. (3.5) makes the ΔV_N to be negative (attractive) since $W_N \leq 0$.

Furthermore, the dispersion relation makes the modulus of the real part of the nuclear potential to have a bell-shaped maximum in vicinity of the Coulomb barrier height [49, 50, 52, 53]. Hence, the contribution by the dispersion relation to ΔV_N at $E = V_B$ should be stronger (more negative) than the contribution at deep sub-barrier energies $\Delta V_{N(\text{deep})}$.

Since $\Delta V_{N(\text{deep})}$ should be attractive ($\Delta V_{N(\text{deep})} < 0$), from Eq. (3.7), we can generally write

$$V_{N(\text{deep})} - V_U \leq 0. \tag{3.8}$$

where less than zero and equals to zero indicate the presence and the absence of the threshold anomaly at deep sub-barrier energies, respectively.

Now, let us use the result of ^{56}Fe + ^{208}Pb system to illustrate our discussion. Using the best fitted diffuseness parameter and the required potential depth to reproduce the barrier height (as obtained from the result in Section 3.3), we can write the best fitted nuclear potential at deep sub-barrier energies as

$$V_{\text{deep}}(r) = -\frac{355.5}{1 + \exp[(r - 11.9\,\text{fm})/0.38\,\text{fm}]}\,\text{MeV}. \tag{3.9}$$

In order to explain the relatively low diffuseness parameter obtained at deep sub-barrier energies, our aim is to see that the V_U has a diffuseness parameter that agrees with the standard value. Let us say that the V_U has $a = 0.63$ fm, and the required potential depth to reproduce the barrier height for ^{56}Fe + ^{208}Pb system when $a = 0.63$ fm is 92.85 MeV (without considering the contribution by the dispersion relation). It is important to notice that if there is a contribution by the dispersion relation at barrier height energy (i.e. $E = V_B$), the potential depth should be lower than 92.85 MeV in order to reproduce the barrier height. For now, let us write the V_U for ^{56}Fe + ^{208}Pb system as

$$V_U(r) = -\frac{V_0}{1 + \exp[(r - 11.9\,\text{fm})/0.63\,\text{fm}]}\,\text{MeV}. \tag{3.10}$$

Let us evaluate the nuclear potentials at $r = 14.4$ fm, which is approximately the turning point for the average deep sub-barrier energies of our experimental data. This gives $V_{N(\text{deep})} = -0.49$ MeV, and $V_U = -1.72$ MeV when the V_0 for Eq. (3.10) is 92.85 MeV. It can be seen that when $V_0 = 92.85$ MeV (i.e. without considering the contribution by the dispersion relation), the V_U of Eq. (3.10) does not satisfy Eq. (3.8).

However, as mentioned before, the V_0 for Eq. (3.10) could be lower than 92.85 MeV due to the contribution by the dispersion relation. For example, if the threshold anomaly is negligible at deep sub-barrier energies but very strong at $E = V_B$, Eq. (3.8) can be satisfied at $r = 14.4$ fm if the V_0 for Eq. (3.10) is approximately 26.5 MeV. Hence, we show that the threshold anomaly could explain the relatively low diffuseness parameters obtained at deep sub-barrier energies, or at least make the V_U to have a higher diffuseness parameter than the one obtained at deep sub-barrier energies. This is due to the fact that the contribution by the dispersion relation at $E = V_B$ is stronger than the contribution at deep sub-barrier energies. However, a more detailed analysis must be done in order to know the actual contribution by the dispersion relation

for each of the studied system. This is required in order to see whether the dispersion relation can lead the V_U to have a diffuseness parameter that agrees with the standard value or not.

3.5 Summary

The surface diffuseness parameters of the nuclear potential for heavy-ion systems of ^{48}Ti, ^{54}Cr, ^{56}Fe, ^{64}Ni, ^{70}Zn + ^{208}Pb reactions have been studied through large-angle quasi-elastic scattering at deep sub-barrier energies. It is found that the diffuseness parameters required to fit the experimental data at deep sub-barrier energies are between 0.32 fm and 0.56 fm. The deduced diffuseness parameters for all of the studied systems are clearly significantly lower than the standard value of around 0.63 fm, except for ^{56}Cr + ^{208}Pb system, where the best fitted diffuseness parameter is in satisfactory agreement with (but still lower than) the standard value. We also study the effects of some calculational inputs, the São Paulo potential, and the phenomenon of threshold anomaly on the deduced diffuseness parameters. We find that the calculational inputs and the São Paulo potential cannot account for the low values of the diffuseness parameter. However, it is found that the phenomenon of threshold anomaly might explain the relatively low diffuseness parameters obtained at deep sub-barrier energies.

Chapter 4

Analysis of the nuclear potential for heavy-ion systems through large-angle quasi-elastic scattering at sub-barrier energies

4.1 Introduction

In Chapter 3, we found that the diffuseness parameter with values considerably lower than the standard value are required in order to fit the experimental data at deep sub-barrier energies. It is clear that a further investigation is required in order to understand the nuclear potential for heavy-ion systems.

In order to make a comprehensive study on the diffuseness parameter, it could be important to make comparisons, for example between the deduced diffuseness parameters for different charge products of the target and projectile. In light of this, we will perform a study on the diffuseness parameter at energies

with an upper range that is above the deep sub-barrier region. This would enable us to check whether low values of the diffuseness parameter are also required at a different energy region other than the deep sub-barrier region, and therefore, would also allow us to see the effect of collision energies on the deduced diffuseness parameter. In order to perform this study, channel couplings must be considered in the calculations since it involves the fittings of experimental data at energies above the deep sub-barrier region.

In this chapter, we carry out a study on the nuclear potential, particularly on the surface diffuseness parameter, for ^{48}Ti, ^{54}Cr, ^{56}Fe, ^{64}Ni, and ^{70}Zn + ^{208}Pb systems (i.e. the same systems as in previous chapter) through large-angle quasi-elastic scattering at sub-barrier energies, which are defined in the next section. The procedures of the analyses are explained in Section 4.2. The results and subsequent discussion are presented in Sections 4.3 and 4.4, respectively. The study is then summarized in Section 4.5.

4.2 Procedures

The calculations are performed using CQEL [41], a modified version of the computer code CCFULL [10]. As before, we deduce the best fitted value of the diffuseness parameter in comparison with the experimental data using the chi square method χ^2, and the experimental data are taken from Mitsuoka *et al.* [21].

The inclusion of channel couplings in the calculations creates numerical instabilities in varying degrees, which depend on the inputs. This would affect the accuracy of the analyses. Using the code, we check and find that at energies below the Coulomb barrier height, the quasi-elastic cross sections are less influenced by channel couplings and by different coupling schemes compared to the quasi-elastic cross sections at energies above the barrier height (see Appendix B). Therefore, in order to serve the purpose and maximize the accuracy of our analyses, we choose to study the diffuseness parameter at energies with an up-

per range above the deep sub-barrier region, but below the Coulomb barrier height.

Hence, in this chapter, we perform analyses at what we referred as "sub-barrier energy region", where all the experimental data up to 3 MeV below the Coulomb barrier height are considered in the fittings. For each system in this study, 3 MeV below the barrier height V_B approximately corresponds to between $0.98V_B$ to $0.99V_B$. Both single-channel and coupled-channels calculations are performed in the analyses at sub-barrier energies. The properties of the single-phonon excitations, the deformation parameters, and the coupling scheme used in coupled-channels calculations are as in Tables 3.1 and 3.2 of Section 3.2. As before, the experimental data with $d\sigma_{\rm qel}/d\sigma_R > 1$ are excluded from the fitting procedures, but included in the figures for completeness.

As in previous chapter, we use an imaginary potential of the Woods-Saxon form with a potential depth of 30 MeV, a radius parameter of 1.0 fm, and a diffuseness parameter of 0.3 fm to simulate the compound nucleus formation. The calculations are insensitive to the imaginary parameters provided that the imaginary potential is confined inside the Coulomb barrier. For the real part of the nuclear potential, the radius parameter r_0 is taken to be 1.22 fm. The value of potential depth V_0 depends on the diffuseness parameter, where the barrier height V_B for each system must be reproduced. The calculations are carried out at scattering angle of $\theta_{\rm c.m.} = 170^\circ$. The radii of the target and the projectile are taken as $R_T = r_T A_T^{1/3}$ and $R_P = r_P A_P^{1/3}$, respectively, where r_T and r_P are taken to be 1.2 fm in order to be consistent with the deformation parameters taken from Kibedi and Spears [42], and Raman *et al.* [43]. As in previous chapter, we analyze and plot the calculated ratio of the quasi-elastic to the Rutherford cross sections as functions of effective energies [2, 3].

4.3 Results

^{48}Ti + ^{208}Pb system

When a single-channel calculation is used, the best fitted diffuseness parameter for ^{48}Ti + ^{208}Pb system is 0.66 fm, with $\chi^2 = 3.21$. The potential depth V_0 that is required to reproduce the Coulomb barrier height is 303.5 MeV. The best fitted diffuseness parameter is in agreement with the standard value of around 0.63 fm. The calculated ratio of the quasi-elastic to the Rutherford cross sections for $a = 0.66$ fm using a single-channel calculation is shown by the solid line in Fig. 4.1(a).

However, as mentioned before, channel couplings start to play an important role at energies above the deep sub-barrier region and therefore should be taken into account in our analyses here. Using the coupling scheme as shown in Table 3.2, the best fitted diffuseness parameter obtained through a coupled-channels calculation is 0.43 fm. This is shown by the solid line in Fig. 4.1(b). The χ^2 value in comparison with the experimental data is 1.52, and the required potential depth V_0 is 233.5 MeV. The deduced diffuseness parameter is considerably lower than the standard value. However, from the resulting χ^2 values, the best fitted diffuseness parameter obtained using a coupled-channels calculation fits the experimental data better than the one obtained through a single-channel calculation. Therefore, the best fitted diffuseness parameter obtained through a coupled-channels calculation should be accepted over the one obtained through a single-channel calculation, which is expected.

^{54}Cr + ^{208}Pb system

For ^{54}Cr + ^{208}Pb system, the best fitted diffuseness parameter obtained using a single-channel calculation is 0.80 fm, with $\chi^2 = 2.05$ and $V_0 = 69.84$ MeV. The best fitted diffuseness parameter is significantly higher than the standard value. The calculated ratio of the quasi-elastic to the Rutherford cross sections

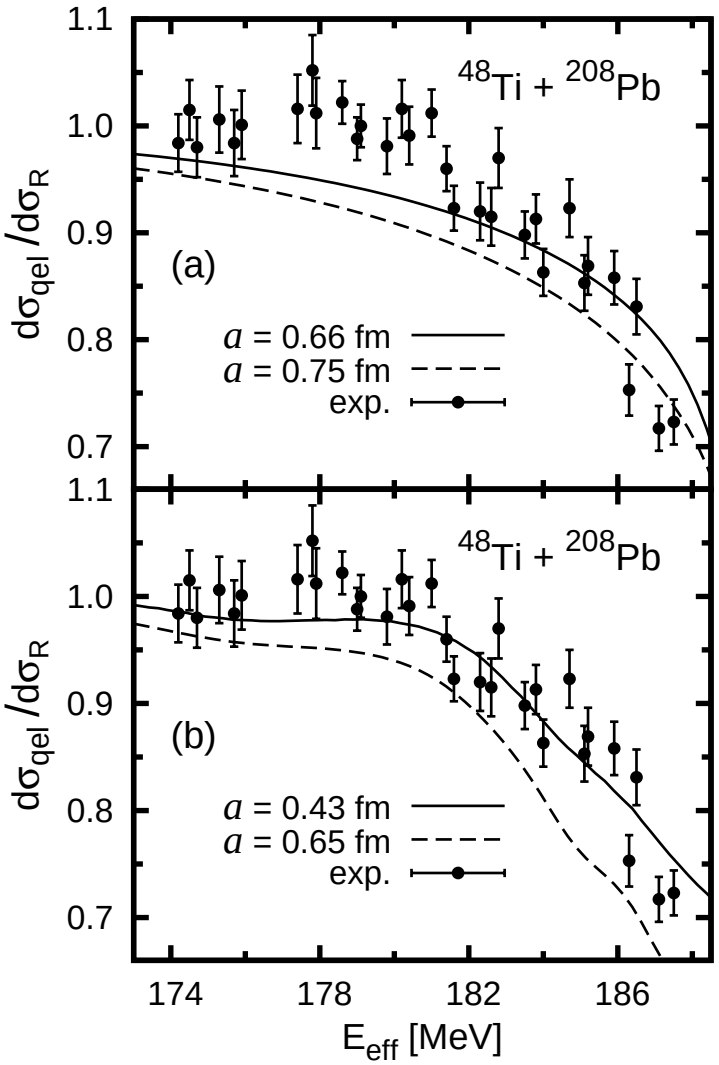

Figure 4.1: The ratio of the quasi-elastic to the Rutherford cross sections for ^{48}Ti + ^{208}Pb system at sub-barrier energies. The analyses in (a) the upper and (b) lower panels are performed using single-channel and coupled-channels calculations, respectively. The experimental data (taken from Mitsuoka *et al.* [21]) with energies up to 3 MeV below the Coulomb barrier height are shown and denoted by dots with error bars. The best fitted diffuseness parameters obtained using a single-channel and a coupled-channels calculations are 0.66 fm and 0.43 fm, respectively. The single-channel and coupled-channels calculations using $a = 0.75$ fm and $a = 0.65$ fm, respectively, are shown for comparison.

for $a = 0.80$ fm using a single-channel calculation is shown by the solid line in Fig. 4.2(a).

When a coupled-channel calculation is used, the best fitted diffuseness parameter is 0.63 fm, with $\chi^2 = 1.36$ and $V_0 = 91.7$ MeV. The best fitted diffuseness parameter, which is shown by the solid line in Fig. 4.2(b), is in agreement with the standard value. Furthermore, the resulting χ^2 values show that the best fitted diffuseness parameter obtained through a coupled-channels calculation fits the experimental data better than the one obtained through a single-channel calculation.

^{56}Fe + ^{208}Pb system

Using a single-channel procedure, the best fitted diffuseness parameter for ^{56}Fe + ^{208}Pb system is 0.76 fm, with $\chi^2 = 3.85$ and $V_0 = 74.9$ MeV. This value is a little high compared to the standard value. Figure 4.3(a) shows the calculated ratio of the quasi-elastic to the Rutherford cross sections for $a = 0.76$ fm using a single-channel calculation.

The best fitted diffuseness parameter obtained through a coupled-channels calculation is 0.59 fm [shown by the solid line in Fig. 4.3(b)], with $\chi^2 = 1.66$ and $V_0 = 103.6$ MeV. This value is in good agreement with the standard value. Again, the obtained χ^2 values show that the best fitted diffuseness parameter obtained through a coupled-channels analysis produce a better fit to the experimental data than the one obtained through a single-channel analysis.

^{64}Ni + ^{208}Pb system

The best fitted diffuseness parameter for ^{64}Ni + ^{208}Pb system obtained through a single-channel analysis is 0.82 fm, with $\chi^2 = 13.28$ and $V_0 = 73.97$ MeV. The deduced diffuseness parameter is significantly higher than the standard value. The calculated ratio of the quasi-elastic to the Rutherford cross sections for the

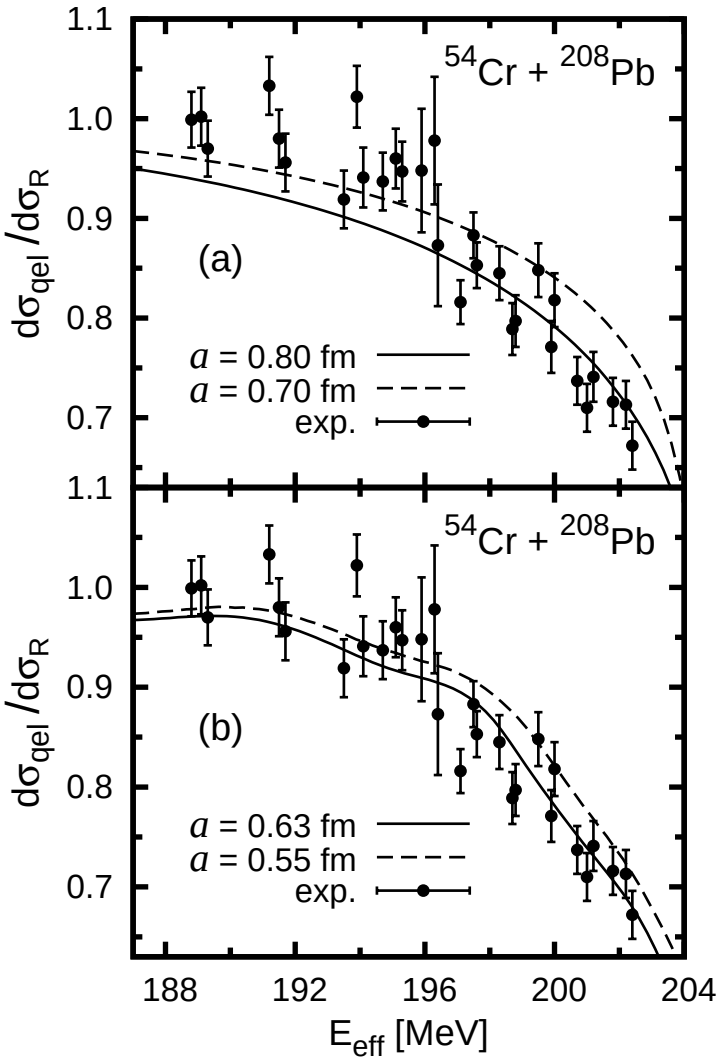

Figure 4.2: The ratio of the quasi-elastic to the Rutherford cross sections for ^{54}Cr + ^{208}Pb system at sub-barrier energies. The analyses in (a) the upper and (b) lower panels are performed using single-channel and coupled-channels calculations, respectively. The experimental data (taken from Mitsuoka *et al.* [21]) with energies up to 3 MeV below the Coulomb barrier height are shown and denoted by dots with error bars. The best fitted diffuseness parameters obtained using a single-channel and a coupled-channels calculations are 0.80 fm and 0.63 fm, respectively. The single-channel and coupled-channels calculations using using $a = 0.70$ fm and $a = 0.55$ fm, respectively, are shown for comparison.

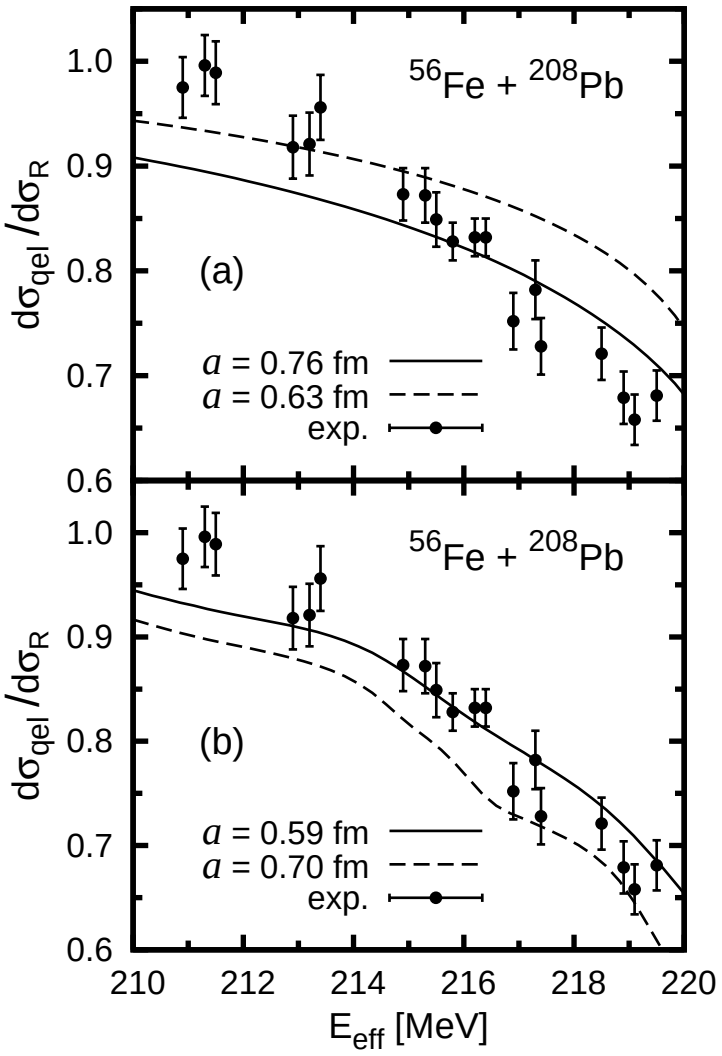

Figure 4.3: The ratio of the quasi-elastic to the Rutherford cross sections for ^{56}Fe + ^{208}Pb system at sub-barrier energies. The analyses in (a) the upper and (b) lower panels are performed using single-channel and coupled-channels calculations, respectively. The experimental data (taken from Mitsuoka *et al.* [21]) with energies up to 3 MeV below the Coulomb barrier height are shown and denoted by dots with error bars. The best fitted diffuseness parameters obtained using a single-channel and a coupled-channels calculations are 0.76 fm and 0.59 fm, respectively. The single-channel and coupled-channels calculations using using $a = 0.63$ fm and $a = 0.70$ fm, respectively, are shown for comparison.

best fitted diffuseness parameter obtained through a single-channel analysis is shown by the solid line in Fig. 4.4(a).

When a coupled-channels procedure is employed, the best fitted diffuseness parameter is 0.66 fm, which is in agreement with the standard value. The obtained χ^2 value is 3.99 and the potential depth V_0 that is required to reproduce the barrier height is 89.05 MeV. Figure 4.4(b) shows the calculated ratio of the quasi-elastic to the Rutherford cross sections for $a = 0.66$ fm using a coupled-channels calculation. It can be seen by comparing Fig. 4.4(a) with Fig. 4.4(b) that the best fitted diffuseness parameter obtained through a coupled-channels procedure fits the experimental data better than the best fitted diffuseness parameter obtained through a single-channel procedure. This fact is very clearly indicated by the χ^2 values obtained from the analyses.

^{70}Zn + ^{208}Pb system

For ^{70}Zn + ^{208}Pb system, the best fitted diffuseness parameter obtained using a single-channel calculation is 0.64 fm, with $\chi^2 = 2.41$ and $V_0 = 105.5$ MeV. This is shown by the solid line in Fig. 4.5(a). The best fitted diffuseness is in a very good agreement with the standard value.

However, channel couplings should be considered in the analysis at sub-barrier energies. This is shown by the results of the other collision systems where coupled-channels calculations produce better fit to the experimental data than single-channel calculations. Using a coupled-channels procedure, the best fitted diffuseness parameter is 0.51 fm, with $\chi^2 = 1.11$ and $V_0 = 168.3$ MeV. This is shown by the solid line in Fig. 4.5(b). The best fitted diffuseness parameter is rather low compared to the standard value. Again, the best fitted diffuseness parameter obtained through a coupled-channels analysis produce a better fit to the experimental data than the one obtained through a single-channel analysis.

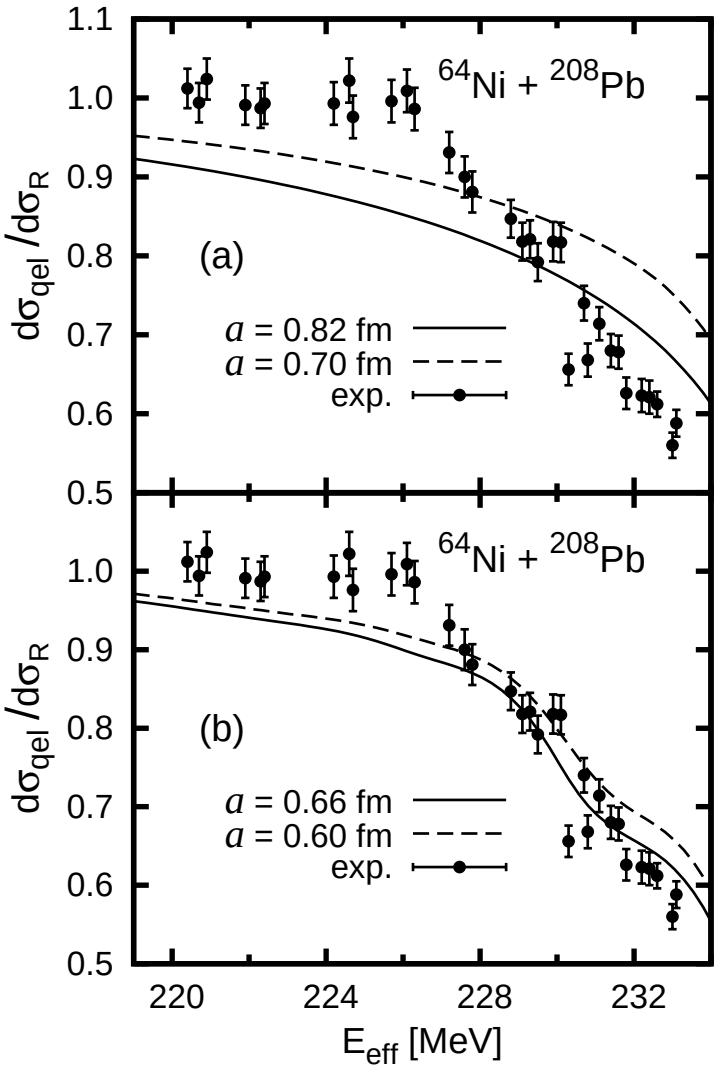

Figure 4.4: The ratio of the quasi-elastic to the Rutherford cross sections for ^{64}Ni + ^{208}Pb system at sub-barrier energies. The analyses in (a) the upper and (b) lower panels are performed using single-channel and coupled-channels calculations, respectively. The experimental data (taken from Mitsuoka *et al.* [21]) with energies up to 3 MeV below the Coulomb barrier height are shown and denoted by dots with error bars. The best fitted diffuseness parameters obtained using a single-channel and a coupled-channels calculations are 0.82 fm and 0.66 fm, respectively. The single-channel and coupled-channels calculations using using $a = 0.70$ fm and $a = 0.60$ fm, respectively, are shown for comparison.

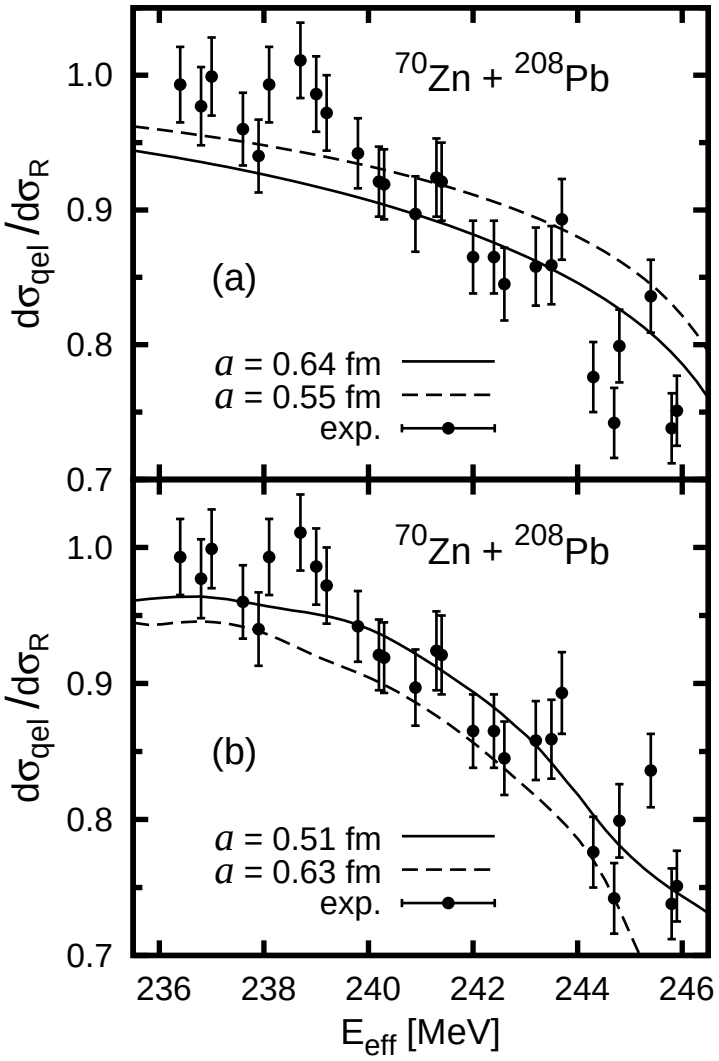

Figure 4.5: The ratio of the quasi-elastic to the Rutherford cross sections for ^{70}Zn + ^{208}Pb system at sub-barrier energies. The analyses in (a) the upper and (b) lower panels are performed using single-channel and coupled-channels calculations, respectively. The experimental data (taken from Mitsuoka *et al.* [21]) with energies up to 3 MeV below the Coulomb barrier height are shown and denoted by dots with error bars. The best fitted diffuseness parameters obtained using a single-channel and a coupled-channels calculations are 0.64 fm and 0.51 fm, respectively. The single-channel and coupled-channels calculations using using $a = 0.55$ fm and $a = 0.63$ fm, respectively, are shown for comparison.

4.4 Discussion

For all of the studied systems, the best fitted diffuseness parameters at sub-barrier energies obtained through coupled-channels and single-channel calculations differ considerably. In light of this, the best fitted diffuseness parameters obtained through coupled-channels calculations are taken as the correct parameters since they produce better fits to the experimental data than the ones obtained through single-channel calculations. This is actually expected since the effect of channel couplings is significant and should be taken into account at energies above the deep sub-barrier region. Figure 4.6 summarizes the best fitted diffuseness parameters obtained at sub-barrier energies as functions of charge products of the target and projectile. The best fitted diffuseness parameters obtained at deep sub-barrier energies from previous chapter are also included for comparison.

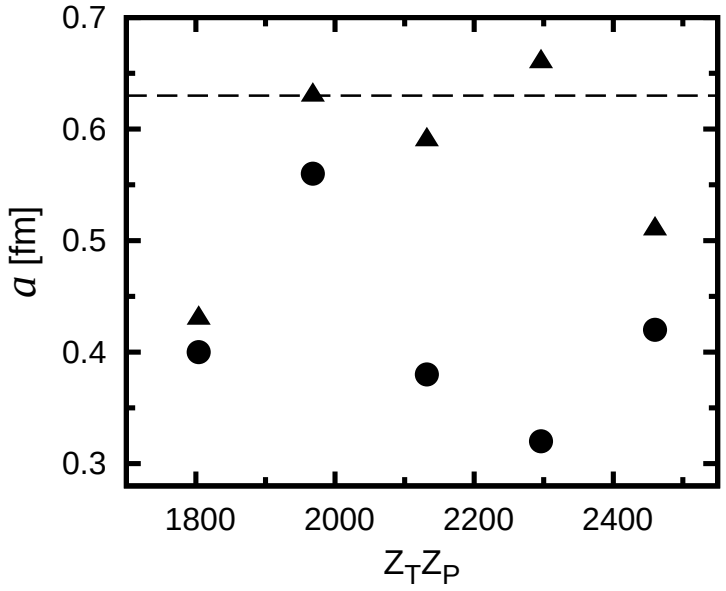

Figure 4.6: The best fitted diffuseness parameters obtained at sub-barrier energies (denoted by triangles) as functions of charge products of the target and projectile $Z_T Z_P$. The best fitted diffuseness parameters obtained at deep sub-barrier energies (denoted by circles) from previous chapter are also included for comparison. The dashed line indicates $a = 0.63$ fm.

At sub-barrier energies, the best fitted diffuseness parameters for ^{54}Cr, ^{56}Fe,

and ^{64}Ni + ^{208}Pb systems are in good agreements with the standard value, but not for ^{48}Ti, and ^{70}Zn + ^{208}Pb systems, where the best fitted diffuseness parameters are significantly low and rather low, respectively, compared to the standard value. It can be seen from Fig. 4.6 that the best fitted diffuseness parameters obtained at sub-barrier energies are generally quite significantly closer to the standard value compared to the diffuseness parameters obtained at deep sub-barrier energies.

It is also interesting to observe that higher diffuseness parameters are required in order to fit the experimental data as the energies are increased closer to the Coulomb barrier heights. This can be clearly seen in Fig. 4.6 by comparing the diffuseness parameters obtained at deep sub-barrier energies with the ones obtained at sub-barrier energies. It must be remembered that the fittings at sub-barrier energies also include the data at deep sub-barrier energies. If the data at deep sub-barrier energies are excluded from the fittings at sub-barrier energies, one can see more prominent increases in the best fitted diffuseness parameter.

It can also be seen from Fig. 4.6 that there is a possible tendency that a higher charge product of the target and projectile leads to a higher increase in the best fitted diffuseness parameter from the one obtained deep sub-barrier energies to the one obtained at sub-barrier energies. However, the increase for ^{70}Zn + ^{208}Pb system is lower than the increases for both ^{56}Fe + ^{208}Pb and ^{64}Ni + ^{208}Pb systems.

An increase in the diffuseness parameter also leads to a lower potential depth required to reproduce the Coulomb barrier height. Therefore, an inconsistency in the diffuseness parameters obtained at the two studied energy regions basically would lead to an inconsistency in values of the potential depth obtained at those studied regions. Figure 4.7 below shows and compares the potential depths obtained at sub-barrier (denoted by triangles) and deep sub-

barrier energies (denoted by circles). It can be seen from Fig. 4.7 that only for ^{54}Cr + ^{208}Pb system, the potential depths obtained at the two studied energy regions quite agree with each other.

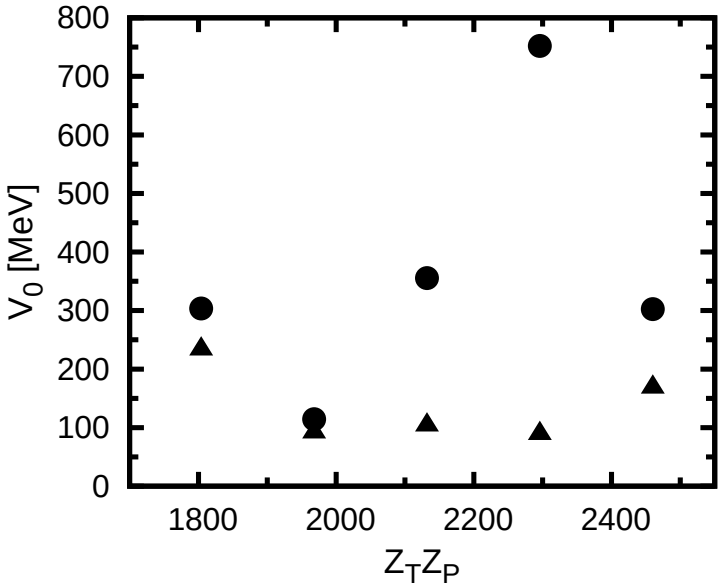

Figure 4.7: The potential depths V_0 obtained at sub-barrier energies (denoted by triangles) as functions of charge products of the target and projectile $Z_T Z_P$. The potential depths V_0 obtained at deep sub-barrier energies (denoted by circles) from the previous chapter are also included for comparison.

Effect of Coulomb barrier height

We found in previous chapter that a small variation in the value of the Coulomb barrier height has a small effect on the deduced diffuseness parameter obtained at deep sub-barrier energies. Here, we find that the effect of the variation of the Coulomb barrier height on the best fitted diffuseness parameter at sub-barrier energies is considerably stronger than the effect at deep sub-barrier energies. For a decrease of 1 MeV in the barrier height from the value that is originally used (i.e. 236.25 MeV), the best fitted diffuseness parameter for ^{64}Ni + ^{208}Pb system obtained at sub-barrier energies decreases by 0.08 fm, to $a = 0.58$ fm (see Fig. 4.8). When $V_B = 235.25$ MeV is used, only the experimental data with energies equal to or lower than 232.25 MeV are used in the fittings. Therefore,

it is important to accurately and precisely know the value of the barrier height in order to study the diffuseness parameter at sub-barrier energies.

Furthermore, it is possible the actual values of the barrier height could be slightly lower or higher than the values that are used here. However, it seems that the uncertainties in barrier height cannot account for the discrepancy between the diffuseness parameters obtained at the two studied energy regions, for example the discrepancy for ^{56}Fe, and ^{64}Ni + ^{208}Pb systems. In fact, lower barrier heights would also make the diffuseness parameters obtained at deep sub-barrier energies (in Chapter 3) to be more inconsistent with the standard value.

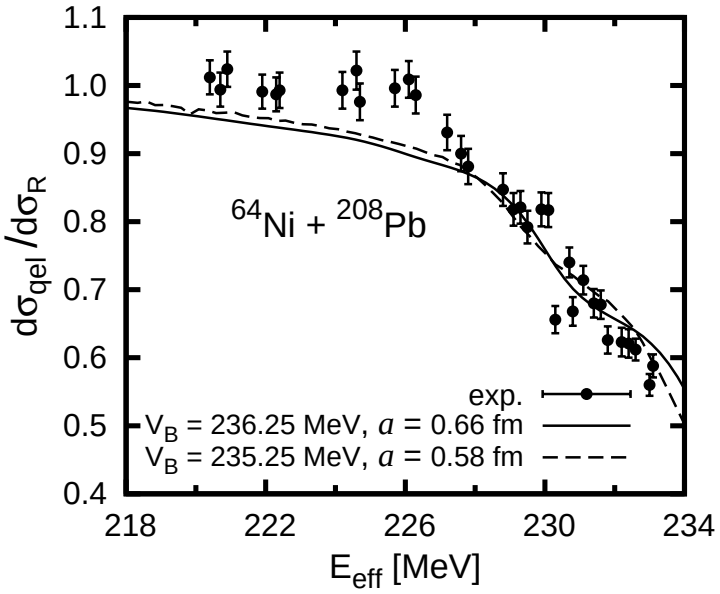

Figure 4.8: The calculated ratio of the quasi-elastic to the Rutherford cross sections for the best fitted diffuseness parameters obtained at sub-barrier energies through coupled-channel calculations for ^{64}Ni + ^{208}Pb system using two different values of the Coulomb barrier height V_B. When $V_B = 236.25$ MeV and $V_B = 235.25$ MeV are used, the best fitted diffuseness parameters are 0.66 fm and 0.58 fm, respectively.

Effect of r_T and r_P

In previous chapter, we found that varying the target and projectile radius parameters (i.e. r_T and r_P) has no effect on the analyses at deep sub-barrier

energies when single-channel calculations are used, while the effect is small when coupled-channels calculations are used. However, at energies above the deep sub-barrier region, varying the r_T and the r_P would considerably vary the calculated quasi-elastic cross sections when coupled-channels calculations are used. For example, when the r_T and/or the r_P are increased, the calculated quasi-elastic cross sections increase. This is because increasing the r_T and/or the r_P reduces the deformation parameters [see Eq. (2.55)], which, in turn, reduces the coupling strengths. Since channel couplings play an important role at sub-barrier energies, the decrease in coupling strengths would decrease fusion cross sections at those energies, which, in turn, would increase quasi-elastic cross sections.

Figures 4.9 to 4.13 show comparisons between the calculated ratio of the quasi-elastic to the Rutherford cross sections for all of the studied systems using $r_T = r_P = 1.3$ fm and $r_T = r_P = 1.2$ fm. As before (see Section 3.4), when $r_T = r_P = 1.3$ fm, the deformation parameters are modified according to Eq. (2.55). It can be seen from Figs. 4.9 to 4.13 that the effects of changing the r_T and the r_P at deep sub-barrier energies are small compared to the effect at energies above the deep sub-barrier region.

The effect of varying the diffuseness parameter on the quasi-elastic cross sections is opposite to the effect of varying the r_T and the r_P. This can be clearly seen from the results (Sections 3.3 and 4.3) where a higher diffuseness parameter leads to lower quasi-elastic cross sections, whereas higher r_T and r_P lead to higher quasi-elastic cross sections. Hence, a lower diffuseness parameter is required in order to best fit the experimental data at sub-barrier energies when lower r_T and r_P are used.

Therefore, it is possible to make the best fitted diffuseness parameters obtained at sub-barrier energies to be consistent with the ones obtained at deep sub-barrier energies by lowering the values of the r_T and the r_P appropriately.

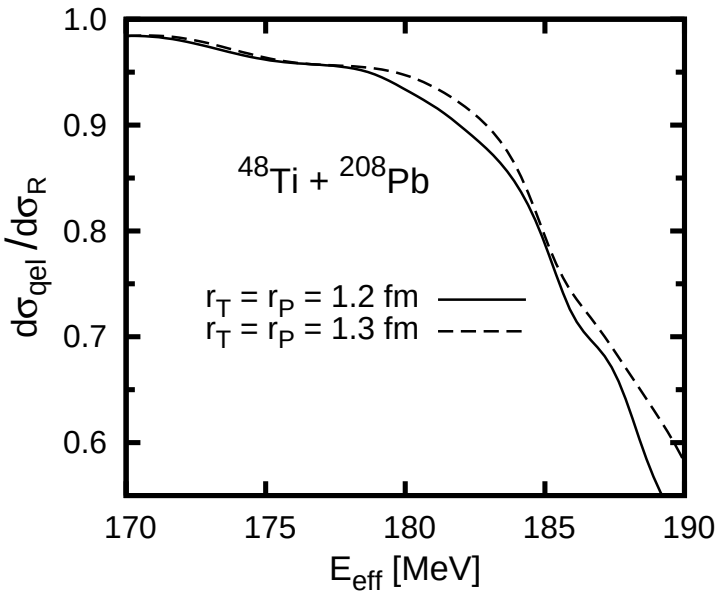

Figure 4.9: Comparison between the calculated ratio of the quasi-elastic to the Rutherford cross sections for ^{48}Ti + ^{208}Pb system using $r_T = r_P = 1.3$ fm (dashed line) and $r_T = r_P = 1.2$ fm (solid line). Both calculations are performed using $a = 0.63$ fm and coupled-channels calculations with the coupling scheme as shown in Table 3.2.

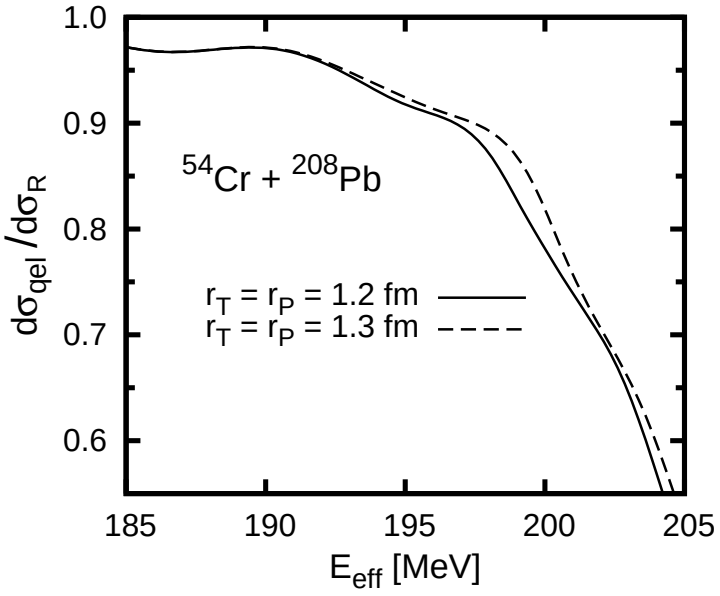

Figure 4.10: The same as Fig. 4.9 but for ^{54}Cr + ^{208}Pb system.

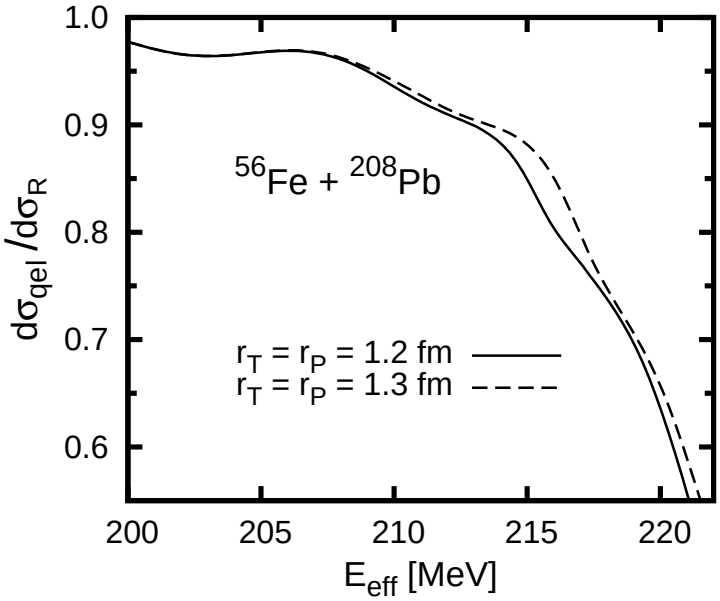

Figure 4.11: The same as Fig. 4.9 but for ^{56}Fe + ^{208}Pb system.

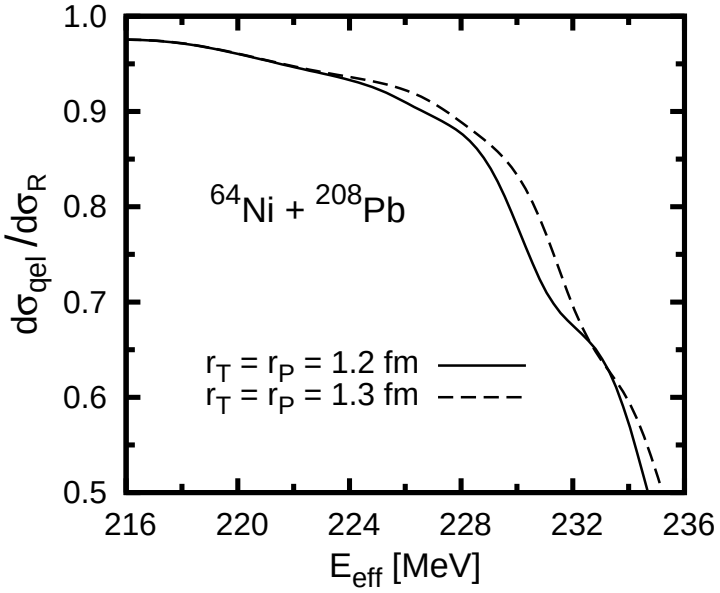

Figure 4.12: The same as Fig. 4.9 but for ^{64}Ni + ^{208}Pb system.

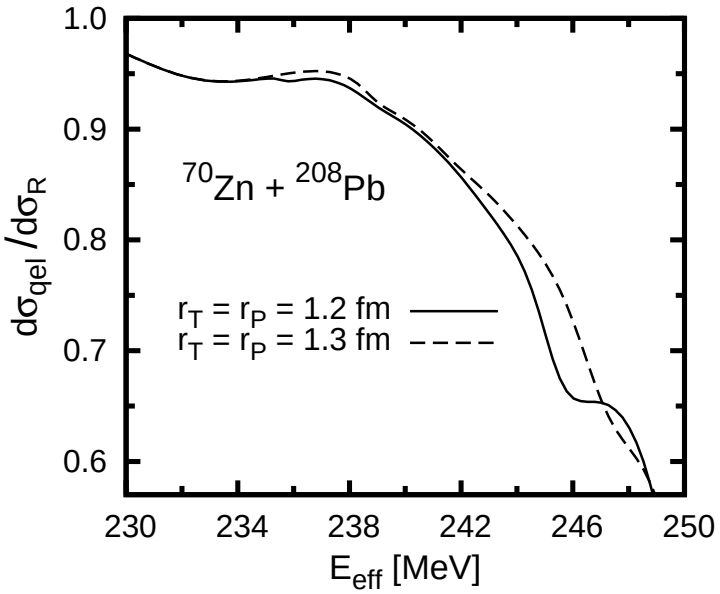

Figure 4.13: The same as Fig. 4.9 but for ^{70}Zn + ^{208}Pb system.

However, several things must be remembered and considered, and this would present difficulties. First, since all of the studied systems have the same target nucleus, the same r_T should be used. Secondly, the ranges of the r_T and the r_P are likely to lie between 1.06 fm and 1.2 fm [11]. Furthermore, it must be remembered that all of the colliding nuclei here are spherical. Therefore, it is natural to feel that the r_P (or the r_T for ^{208}Pb) for each nucleus should not differ significantly.

According to the results for ^{48}Ti + ^{208}Pb system, $r_T \approx 1.2$ fm should be used in order to make the best fitted diffuseness parameters obtained at the two energy regions to be consistent with each other. However, when $r_T \approx 1.2$ fm is used for ^{56}Fe, and ^{64}Ni + ^{208}Pb systems for example, the consistency in the values of the diffuseness parameter obtained at the two energy regions can only be achieved if the r_P's for ^{56}Fe and ^{64}Ni are significantly lower than 1.06 fm. This effort would also make the value of the r_P and the r_P for each nuclei studied here to differ significantly. Therefore, an inconsistency in the values of r_P and r_T would be created in order to achieve a consistency in the values of the

diffuseness parameter obtained at the two studied energy regions. Furthermore, this effort would also make the best fitted diffuseness parameters obtained at sub-barrier energies to be much more inconsistent with the standard value.

In order to support our discussion above, when $r_T = 1.2$ fm and $r_P = 1.06$ fm are used, the best fitted diffuseness parameter for ^{56}Fe + ^{208}Pb system obtained at sub-barrier energies through a coupled-channels calculation is to 0.57 fm (shown in Fig. 4.14). This means that the value of the best fitted diffuseness parameter is reduced by only 0.02 fm from the value when $r_T = r_P = 1.2$ fm are used. This shows that when $r_T = 1.2$ fm is used, r_P with a value much lower than 1.06 fm is required for ^{56}Fe + ^{208}Pb system to make the best fitted diffuseness parameter obtained at sub-barrier energies to be consistent with the one obtained at deep sub-barrier energies, if it is possible.

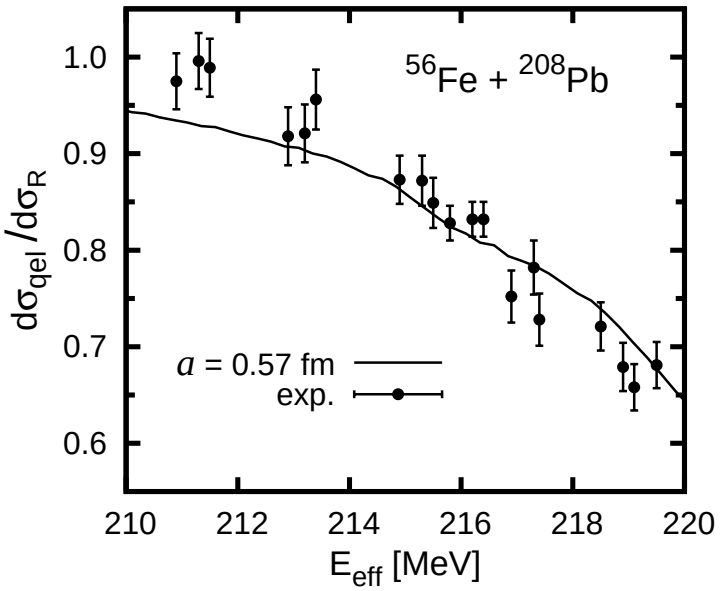

Figure 4.14: The calculated ratio of the quasi-elastic to the Rutherford cross sections for the best fitted diffuseness parameter ($a = 0.57$ fm) for ^{56}Fe + ^{208}Pb system when $r_T = 1.2$ fm and $r_P = 1.06$ fm are used. The analysis is obtained using a coupled-channels calculation. As usual, the experimental data are taken from Mitsuoka *et al.* [21]).

The values of $r_T = r_P = 1.2$ fm that we use here are widely used for the studied nuclei, including by our references, such as by Kibedi and Spears [42],

and Raman *et al.* [43]. Hence, it must be stressed that it is very important to accurately and precisely know the r_T and the r_P in order to correctly determine the diffuseness parameters at sub-barrier energies. Therefore, considering the inputs that are available, this present study suggests that higher values of diffuseness parameter are required in order to fit the experimental data as the energies are increased from the deep sub-barrier region to the energies closer to the Coulomb barrier height.

São Paulo potential

In Section 3.4, we showed that the effect of Pauli nonlocality is clearly negligible at deep sub-barrier energies. In order to try to explain the discrepancy between the diffuseness parameters obtained at sub-barrier energies and deep sub-barrier energies, we employ the São Paulo potential [i.e. by using Eq. (3.4)] in the calculations at sub-barrier energies.

Figure 4.15 shows the results of our calculations for ^{56}Fe + ^{208}Pb system at sub-barrier energies. Similar as the result at deep sub-barrier energies, the differences between the quasi-elastic cross sections at sub-barrier energies obtained using the São Paulo potential and the Woods-Saxon potential for the same diffuseness parameter are very small.

If the Pauli nonlocality is able to explain the discrepancy found in this study, then the V_{S-P} [Eq. (3.4)] should produce (almost) the same best fitted diffuseness parameter when fitting the experimental data at deep sub-barrier energies and when fitting the experimental data at sub-barrier energies. However, the calculations show that this is not the case. Hence, we demonstrate that the effect of Pauli nonlocality is clearly negligible at sub-barrier energies, and cannot account for the discrepancy found in this study.

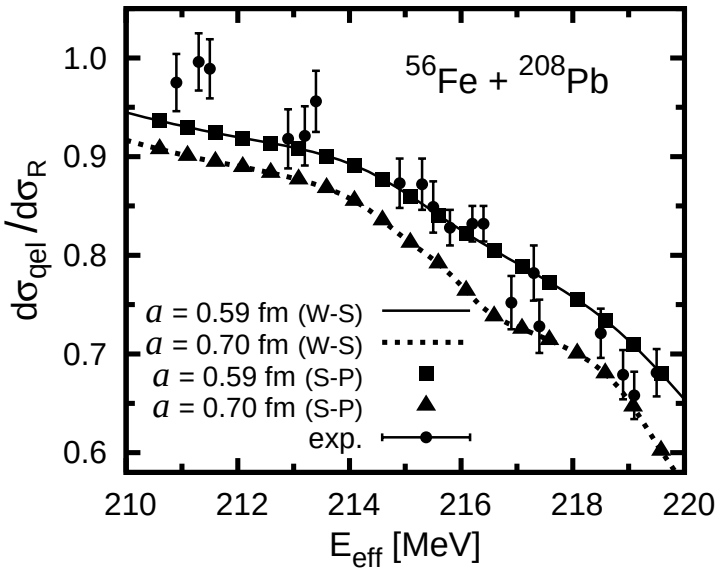

Figure 4.15: Same as Fig. 4.3(b). W-S and S-P denote the Woods Saxon potential [Eq. (2.3)] and the São Paulo potential [Eq. (3.4)], respectively. The plots using the Woods-Saxon potential (solid and dotted lines) are the same as in Fig. 4.3(b). The plots using the São Paulo potential shown by squares and triangles are obtained using coupled-channels calculations (as shown in Table 3.2) with $a = 0.59$ fm and $a = 0.70$ fm, respectively.

Effect of threshold anomaly

In Section 3.4, we have discussed the effect of the phenomenon of threshold anomaly on the obtained best fitted diffuseness parameters. It can be concluded that if the phenomenon of threshold anomaly is present, it could make the best fitted diffuseness parameters to appear lower than their original values.

It is interesting to see if the effect of threshold anomaly could explain the discrepancy between the diffuseness parameters obtained at sub-barrier energies and deep sub-barrier energies. As mentioned before, the dispersion relation makes the modulus of the real part of the nuclear potential to have a bell-shaped maximum at energies near the Coulomb barrier height [49, 50, 52, 53]. The sub-barrier region should effectively be closer to the location of the maximum than the deep sub-barrier region. This is apparent since from our definition here, the sub-barrier region can be described as the deep sub-barrier region plus all the energies up to 3 MeV below the barrier height. Hence, due to the dispersion

relation, the modulus of ΔV_N [see Eq. (3.5)] at sub-barrier region $\Delta V_{N(\mathrm{sub})}$ should be larger than the modulus of ΔV_N at deep sub-barrier region $\Delta V_{N(\mathrm{deep})}$. In other words, $\Delta V_{N(\mathrm{sub})}$ is more negative than $\Delta V_{N(\mathrm{deep})}$.

Similar as the discussion on the threshold anomaly at deep sub-barrier energies (see Section 3.4), we can write the nuclear potential obtained from the fitting of the experimental data at sub-barrier energies $V_{N(\mathrm{sub})}$ as

$$V_{N(\mathrm{sub})} = V_U + \Delta V_{N(\mathrm{sub})}, \tag{4.1}$$

where V_U is the original nuclear potential that is not affected by the threshold anomaly. Let us write again the nuclear potential obtained at deep sub-barrier energies, which is

$$V_{N(\mathrm{deep})} = V_U + \Delta V_{N(\mathrm{deep})}. \tag{4.2}$$

In order to eliminate the discrepancy, the V_U's in Eqs. (4.1) and (4.2) should be the same. Eliminating the V_U through Eqs. (4.1) and (4.2), and using the fact that $\Delta V_{N(\mathrm{sub})}$ is more negative than $\Delta V_{N(\mathrm{deep})}$, we can write

$$V_{N(\mathrm{sub})} - V_{N(\mathrm{deep})} < 0. \tag{4.3}$$

Let us again use the results of ^{56}Fe + ^{208}Pb system for illustration. Using the obtained potential depths and diffuseness parameters (see Sections 3.3 and 4.3), we can write

$$V_{\mathrm{deep}}(r) = -\frac{355.5}{1 + \exp[(r - R_0)/0.38\,\mathrm{fm}]}\,\mathrm{MeV}, \tag{4.4}$$

and

$$V_{\mathrm{sub}}(r) = -\frac{103.6}{1 + \exp[(r - R_0)/0.59\,\mathrm{fm}]}\,\mathrm{MeV}. \tag{4.5}$$

The R_0 in Eq. (4.5) should be slightly higher than the R_0 in Eq. (4.4) due to couplings [see Eq. (2.58)]. However, let us also use $R_0 = 11.9$ fm in Eq. (4.5)

since this would not invalidate our discussion here. Let us evaluate the nuclear potentials at $r = 15$ fm, which makes $V_{N(\text{deep})} = -0.102$ MeV and $V_{N(\text{sub})} = -0.539$ MeV. It can be seen that $V_{N(\text{sub})} - V_{N(\text{deep})} = -0.437$ MeV, which is less than 0 MeV, thus, satisfies Eq. (4.3). Therefore, it seems that it is possible to eliminate or at least reduce the discrepancy through the dispersion relation. However, again, it is important to know the actual contribution by the dispersion relation, so we can determine how much the discrepancy can be reduced.

Dynamical effects

It is also likely that the discrepancy between the diffuseness parameters obtained at the two studied regions could due to the same factors that might cause the diffuseness parameters obtained through fusion experimental data higher than those obtained through scattering experimental data (see Newton *et al.* [7] for example). In fusion process, the colliding nuclei would penetrate deeper into the nuclear potential region (i.e. the colliding nuclei approach each other closer) than in scattering. Similarly, in quasi-elastic scattering at sub-barrier energies, the colliding nuclei generally approach each other closer than in quasi-elastic scattering at deep sub-barrier energies. So, it is apparent to make a connection between the obtained diffuseness parameters and how close the colliding nuclei approach each other.

Newton *et al.* [7] have discussed several reasons that might cause the discrepancy between the diffuseness parameter obtained through fusion and scattering experimental data. One reason that might be related to scattering at energies below the barrier height is the dynamical effects, particularly regarding neutron movements towards the other nucleus when the colliding nuclei come close together. This would reduce the dynamical barrier compared to the normal static barrier [54]. The reduction in the barrier clearly would increase the fusion cross

sections, thus decreasing the quasi-elastic cross sections.

So, if the neutron movements are stronger at sub-barrier energies than at deep sub-barrier energies, then the quasi-elastic cross sections at sub-barrier energies would be lower than expected in comparison with the quasi-elastic cross sections obtained at deep sub-barrier energies. As can be seen from the results of the calculations (e.g. Section 4.3), a higher diffuseness parameter is required in order to fit lower quasi-elastic cross sections. This could at least partly explain the increase in the diffuseness parameters obtained in this present study as the energies increase.

4.5 Summary

The surface diffuseness parameters of the nuclear potential for heavy-ion systems of ^{48}Ti, ^{54}Cr, ^{56}Fe, ^{64}Ni, and ^{70}Zn + ^{208}Pb reactions have been studied through large-angle quasi-elastic scattering at sub-barrier energies. The diffuseness parameters required to fit the experimental data are between 0.43 fm and 0.66 fm. The deduced diffuseness parameters for ^{54}Cr, ^{56}Fe, and ^{64}Ni + ^{208}Pb systems agree with the standard value. However, the best fitted diffuseness parameters for ^{48}Ti, and ^{70}Zn + ^{208}Pb systems are significantly low and rather low, respectively, compared to the standard value.

At sub-barrier energies, higher values of the r_T and r_P would give higher best fitted diffuseness parameters when coupled-channels calculations are used. Therefore, accurate and precise values of the r_T and r_P are required in order to find the correct values of the diffuseness parameter. Similarly, accurate and precise Coulomb barrier heights are needed in order to study and deduce the diffuseness parameters at sub-barrier energies.

From the analyses, it is found that higher values of the diffuseness parameter are required in order to fit the experimental data as the energies are increased from the deep sub-barrier region to the energies closer to the Coulomb barrier

heights. This can be seen by comparing the results of the analyses at deep sub-barrier (from Chapter 3) and at sub-barrier energies. The increase in the diffuseness parameters also leads to a decrease in the potential depths. There is also a possible tendency that a higher charge product of the target and projectile leads to a higher increase in the best fitted diffuseness parameter from the one obtained at deep sub-barrier energies to the one obtained at sub-barrier energies. However, the increase for ^{70}Zn + ^{208}Pb system is lower than the increase for both ^{56}Fe + ^{208}Pb and ^{64}Ni + ^{208}Pb systems.

The are a few possible reasons that might cause the discrepancy between the diffuseness parameters obtained at sub-barrier and deep sub-barrier energies. It is found that the phenomenon of threshold anomaly could possibly explain the discrepancy. It is also possible that the discrepancy is due to the same factors that might cause the discrepancy between the diffuseness parameters obtained through quasi-elastic scattering experimental data and fusion experimental data [7], particularly regarding neutron movements.

Chapter 5

Summary and concluding remarks

In this thesis, the nuclear potentials for some heavy-ion reactions have been studied through large-angle quasi-elastic scattering. We have shown and argued that large-angle quasi-elastic scattering is a suitable method to study the nuclear potential. Recently, many large-angle quasi-elastic scattering experimental data have been measured with high precision and accuracy, which enable reliable analyses to be performed. In this thesis, analyses on the nuclear potentials, in particular the surface diffuseness parameters, for ^{48}Ti, ^{54}Cr, ^{56}Fe, ^{64}Ni, and ^{70}Zn + ^{208}Pb systems have been performed. The analyses are performed by fitting the experimental data at deep sub-barrier and sub-barrier energies, as defined in Chapters 3 and 4, respectively.

For the analyses at deep sub-barrier energies, the diffuseness parameters that are required to fit the experimental data are between 0.32 fm and 0.56 fm. The best fitted values for all of the studied reaction systems are clearly significantly lower than the standard value of around 0.63 fm, except for ^{56}Cr + ^{208}Pb system, where the best fitted diffuseness parameter ($a = 0.56$ fm) is in satisfactory agreement with (but still lower than) the standard value. We investigate the effects of some calculational inputs, the São Paulo potential, and the threshold

anomaly on the deduced diffuseness parameters. We find that the threshold anomaly might explain the relatively low diffuseness parameters obtained at deep sub-barrier energies in comparison with the standard value.

For the analyses at sub-barrier energies, the diffuseness parameters that are required to fit the experimental data are between 0.43 fm and 0.66 fm. The best fitted diffuseness parameters for ^{54}Cr, ^{56}Fe, and ^{64}Ni + ^{208}Pb systems agree with the standard value. However, the best fitted diffuseness parameters for ^{48}Ti, and ^{70}Zn + ^{208}Pb systems are significantly low and rather low, respectively, compared to the standard value. The deduced diffuseness parameters obtained at sub-barrier energies are generally quite significantly closer to the standard value compared to the diffuseness parameters obtained at deep sub-barrier energies. We investigate the effects of some calculational inputs on the deduced diffuseness parameters and found that the target radius parameter r_T, the projectile radius parameter r_P, and the Coulomb barrier heights V_B play quite significant roles in determining the diffuseness parameters at sub-barrier energies. Therefore, accurate and precise values of the target radius parameter, the projectile radius parameter, and the barrier height must be known to correctly determine the diffuseness parameters from the analyses at sub-barrier energies.

From the results of the analyses, it is found that higher values of diffuseness parameter are required in order to fit the experimental data as the energies are increased from the deep sub-barrier region to the energies closer to the Coulomb barrier heights. This can be seen by comparing the results of the analyses at deep sub-barrier energies (Chapter 3) and at sub-barrier energies (Chapter 4). An increase in the diffuseness parameter also leads to a decrease in the potential depth. There is also a possible tendency that a higher charge product of the target and projectile leads to a higher increase in the best fitted diffuseness parameter from the one obtained at deep sub-barrier energies to the one obtained

at sub-barrier energies. However, the increase for ^{70}Zn + ^{208}Pb system is lower than the increase for both ^{56}Fe + ^{208}Pb and ^{64}Ni + ^{208}Pb systems.

We try to find out the reasons other than the calculational inputs in order to account for discrepancy between the diffuseness parameters obtained at the two studied regions. We show that that the effect of Pauli nonlocality is negligible in this present study. On the other hand, we find that the phenomenon of threshold anomaly, a well-known phenomenon in the scattering of heavy-ions, could eliminate or at least reduce the discrepancy. It is also possible that the discrepancy is due to the same factors that might cause the best fitted diffuseness parameters obtained through fusion experimental data higher than those obtained through scattering experimental data. One of the factors is the dynamical effects, particularly regarding the neutron movements.

Further studies on many other collision systems will definitely be helpful in order to support or disprove the findings in this present study. Experimental data that enable the determination of the actual contribution by the dispersion relation on the studied systems will also be helpful in order to see how well the threshold anomaly can explain the findings in this study. New experimental data will also be helpful in case there are errors in the present data.

Appendix A

Phenomenological nuclear potential

In the thesis, we assume that the nuclear potential has the Woods-Saxon form [Eq. (2.3)], and we determine the parameters such that they reproduce the experimental data. The nuclear potential can also be obtained by folding a nucleon-nucleon interaction in the projectile and the target densities [55]. The nuclear potential in this double folding procedure is given by

$$V_N(r) = \int d\vec{\mathbf{r}}_1 d\vec{\mathbf{r}}_2 v_{NN}(\vec{\mathbf{r}} - \vec{\mathbf{r}_1} + \vec{\mathbf{r}_2})\rho_T(\vec{\mathbf{r}_1})\rho_P(\vec{\mathbf{r}_2}), \tag{A.1}$$

where v_{NN} is the effective interaction between two nucleons, while ρ_P and ρ_T are the the distribution of the centers of mass of the nucleons in the ground state of the projectile and target nuclei, respectively. The coordinates for the double folding potential are shown in Fig. A.1.

Akyüz and Wither [56] numerically performed this procedure and parameterized the nuclear interaction in the Woods-Saxon form with

$$V_0 = 16\pi\gamma\bar{R}a, \tag{A.2}$$

$$R_0 = R_P + R_T + 0.29, \tag{A.3}$$

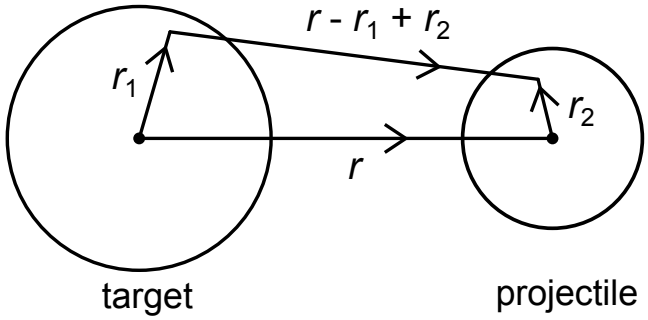

Figure A.1: Coordinates for the double folding potential.

$$R_i = 1.233A_i^{1/3} - 0.98A_i^{-1/3} \qquad (i = P, T), \tag{A.4}$$

$$\bar{R} = R_P R_T/(R_T + R_P), \tag{A.5}$$

$$\gamma = \gamma_0 \left[1 - 1.8 \left(\frac{N_P - Z_P}{A_P}\right) \left(\frac{N_T - Z_T}{A_T}\right)\right], \tag{A.6}$$

where $a = 0.63$ fm and $\gamma_0 = 0.95$ MeV fm^{-2}.

Christensen and Winther [57] used the experimental data of elastic scattering to formulate a nuclear potential in the form of

$$V_N(r) = V_0 \bar{R} \exp[-(r - R_T - R_P)/a], \tag{A.7}$$

where R_P, R_T, $\bar{R}$ and a are the same as those in the Akyüz-Winther potential described above. Vaz *et al.* [58] has discussed a method to use the experimental data of heavy-ion fusion reactions at energies above the Coulomb barrier. This method has also been employed in high precision data of heavy-ion fusion cross sections [7, 59]. Such procedure leads to results that suggest a Woods-Saxon potential has larger surface diffuseness parameters a (ranging from 0.75 to 1.1 fm) than the ones obtained from the experimental data of elastic scattering (i.e. $a \approx 0.63$ fm). The effects of internal excitations have been shown to have an important role in determining the empirical nuclear potential for the ^{16}O + ^{144}Sm reaction [60]. However, for deformed systems ^{16}O + ^{154}Sm, ^{186}W, those effects are negligible at energies above the Coulomb barrier where the experimental

data were fitted. Therefore, the origin of the large surface diffuseness parameter still remains a problem to be solved.

Appendix B

Comparison between coupled-channels calculations at energies around the Coulomb barrier

In order to see the effect of collision energy on the obtained best fitted diffuseness parameter, we have to make a comparison between the best fitted diffuseness parameter obtained at deep sub-barrier energies with the one obtained at energies above the deep sub-barrier range. We find that at energies below the Coulomb barrier height, the quasi-elastic cross sections are less influenced by channel couplings and by different coupling schemes compared to the quasi-elastic cross sections at energies above the barrier height. Figure B.1 below illustrates this. It can be seen that at energies below the barrier height (which is 205.50 MeV for ^{54}Cr + ^{208}Pb system [45]), the coupled-channels calculations are closer to the single-channel calculation than those at energies above the barrier height. Also, the differences between the coupled-channels calculations obtained using two different coupling schemes are smaller at energies below the barrier height than those at energies above the barrier height.

Since the analyses above the deep sub-barrier region require coupled-channels calculations, we decide to constrain the energy range of our analyses to the region below the Coulomb barrier height in order to minimize the effect of channel couplings and maximize the accuracy of the analyses. Therefore, in Chapter 4, we perform analyses by using large-angle quasi-elastic experimental data with energy up to 3 MeV below the Coulomb barrier height.

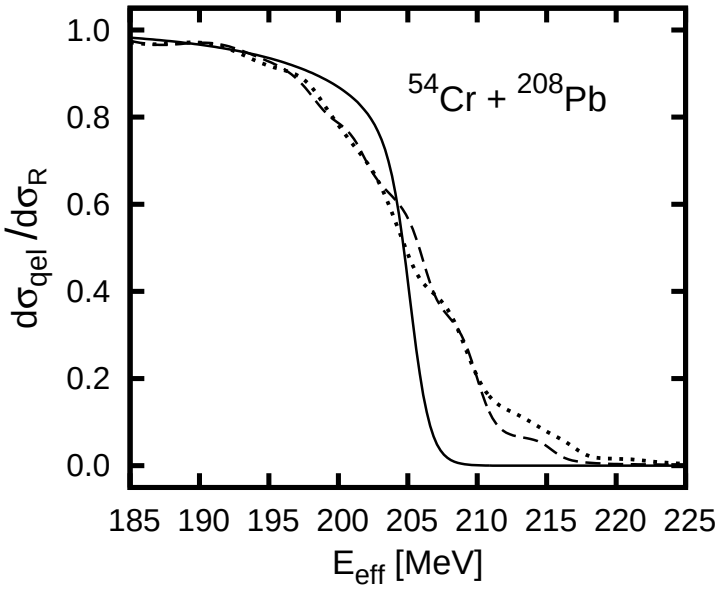

Figure B.1: A comparison between a single-channel calculation (solid line) and coupled-channel calculations obtained using two different coupling schemes (dashed and dotted lines) for ^{54}Cr + ^{208}Pb system. The dashed line shows a coupled-channels calculation using single-quadrupole phonon and triple-octupole phonon excitations in the projectile and the target, respectively. The dotted line shows a coupled-channels calculation using triple-quadrupole phonon and triple-octupole phonon excitations in the projectile and the target, respectively. All calculations are performed using $a = 0.63$ fm.

Appendix C

Numerical stabilization of coupled-channels calculations

When coupled-channels analyses are performed using the CCFULL code [10], the off-diagonal components of the coupling matrix are assumed to be zero at a distance below a coupling cut-off radius $r_{\rm cut}$. This is justified due to a strong absorption in the inner region of a heavy-ion system. The coupling cut-off radius is intended to stabilize the calculations and only affects coupled-channels calculations. This matter was discussed in more details by Muhammad Zamrun F. *et al.* [45].

For ^{70}Zn + ^{208}Pb system, a coupling cut-off radius of 12 fm is used, instead of 10.9 fm that is used in the other systems. The reason for this change is because a cut-off radius below 12 fm produces significant numerical instabilities in the calculations for ^{70}Zn + ^{208}Pb system at relatively high values of diffuseness parameter, causing the best fitted diffuseness parameter at sub-barrier energies unable to be determined when using a coupled-channels procedure.

Figure C.1 compares between the calculated ratio of the quasi-elastic to the Rutherford cross sections using $r_{\rm cut}$ = 12.0 fm and $r_{\rm cut}$ = 10.9 fm for ^{70}Zn + ^{208}Pb system. The calculations are done using the coupling scheme as shown in Table 4.2, and a = 0.63 fm. It can be seen that the differences

between the calculated cross sections using the two values of r_{cut} are small in the studied energy region, which is under 3 MeV below the Coulomb barrier height. Moreover, it is also justified to increase the r_{cut} slightly for the ^{70}Zn + ^{208}Pb system since the projectile has a slightly larger nuclear radius compared to the other studied projectiles. The barrier height for ^{70}Zn + ^{208}Pb system when using $a = 0.63$ fm is located at 13.45 fm. Therefore, the location of the $r_{\mathrm{cut}} = 12.0$ fm should still be well inside the Coulomb barrier for other values of diffuseness parameter in general.

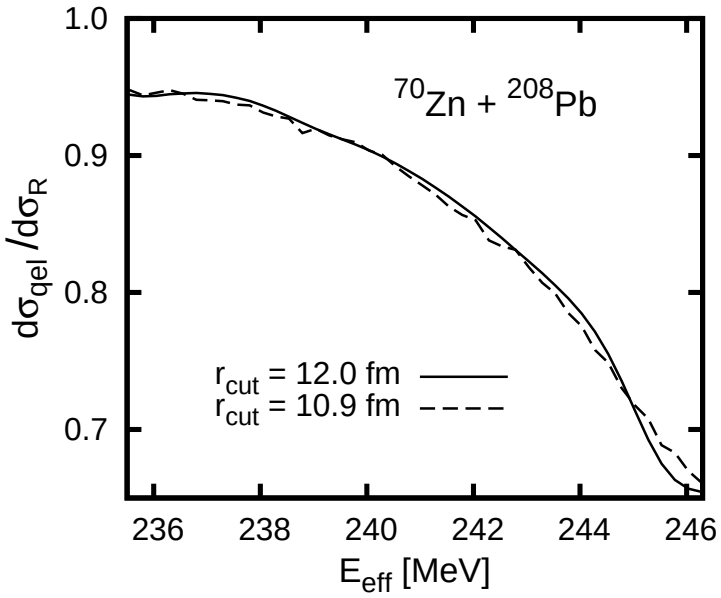

Figure C.1: Comparison between the calculated ratio of the quasi-elastic to the Rutherford cross sections obtained using $r_{\mathrm{cut}} = 12.0$ fm (solid line) and $r_{\mathrm{cut}} = 10.9$ fm (dashed line) for ^{70}Zn + ^{208}Pb system. The calculations are performed using the coupling scheme as shown in Table 3.2, with $a = 0.63$ fm.

Bibliography

[1] R. D. Woods and D. S. Saxon, *Phys. Rev.* **95**, 2 (1954).

[2] H. Timmers, J. R. Leigh, M. Dasgupta, D. J. Hinde, R. C. Lemmon, J. C. Mein, C. R. Morton, J. O. Newton and N. Rowley, *Nucl. Phys.* **A584**, 190 (1995).

[3] K.Hagino and N. Rowley, *Phys. Rev. C* **69**, 054610 (2004).

[4] Yu. Ts. Oganessian *et al.*, *Nature* **400**, 242-245 (1999).

[5] Yu. Ts. Oganessian *et al.*, *Phys. Rev. C* **63**, 011301(R) (2001).

[6] Yu. Ts. Oganessian *et al.*, *Phys. Rev. Lett.* **104**, 142502 (2010).

[7] J. O. Newton, R. D. Butt, M. Dasgupta, D. J. Hinde, I. I. Gontchar, C. R. Morton, and K. Hagino, *Phys. Rev. C* **70**, 024605 (2004); *Phys. Lett.* **B586**, 219 (2004).

[8] A. B. Balantekin, and N. Takigawa, *Rev. Mod. Phys.* **70**, 77 (1998).

[9] H. Esbensen, S. Landowne and H. Price, *Phys. Rev. C* **36**, 1216 (1987); **36** 2359 (1987).

[10] K. Hagino, N. Rowley and A. T. Kruppa, *Comput. Phys. Commun.* **123**, 143 (1999).

[11] L. R. Gasques, M. Evers, D. J. Hinde, M. Dasgupta, P. R. S. Gomes, R. M. Anjos, M. L. Brown, M. D. Rodriguez, R. G. Thomas and K. Hagino, *Phys. Rev. C* **76**, 024612 (2007).

[12] K. Washiyama, K. Hagino and M. Dasgupta, *Phys. Rev. C* **73**, 034607 (2006).

[13] M. Evers, M. Dasgupta, D. J. Hinde, L. R. Gasques, M. L. Brown, R. Rafiei and R. G. Thomas, *Phys. Rev. C* **78**, 034614 (2008).

[14] P. Fröbrich and R. Lipperheide, *Theory of Nuclear Reactions* (Oxford University Press, New York, 1996), p.243.

[15] H. Timmers, PhD Thesis, Australian National University, Canberra (1996).

[16] C. H. Dasso, S. Landowne and A. Winther, *Nucl. Phys.* **A405**, 381 (1983).

[17] S. Landowne and S. C. Pieper, *Phys. Rev. C* **29**, 1352 (1984).

[18] M. Dasgupta, D. J. Hinde, and A. M. Stefanini, *Annu. Rev. Part. Sci.* **48**, 401 (1998).

[19] W. Reisdorf, *J. of Phys. G* **20**, 1297 (1994).

[20] S. S. Ntshangase *et al.*, *Phys. Lett.* **B651**, 27 (2007).

[21] S. Mitsuoka, H. Ikezoe, K. Nishio, K. Tsuruta, S. C. Jeong, Y. Watanabe, *Phys. Rev. Lett.* **99**, 182701 (2007).

[22] C. H. Dasso and G. Pollarolo, *Phys. Lett.* **B155**, 223 (1985); C. H. Dasso and A. Vitturi, *ibid.* **B179**, 337 (1986).

[23] S. Landowne, C. Price and H. Esbensen, *Nucl. Phys.* **A484**, 98 (1988).

[24] R. A. Broglia, C. H. Dasso and S. Landowne, *Phys. Rev. C* **32**, 1426 (1985).

[25] H. Esbensen and S. Landowne, *Nucl. Phys.* **A492**, 473 (1989).

[26] M. A. Nagarajan, A. B. Balantekin and N. Takigawa, *Phys. Rev. C* **34**, 894 (1986).

[27] N. Takigawa and K. Ikeda, ANL-PHY-86-1, p.613-620; *Proc. of the Intl. Symposium on the Many Facets of Heavy Ion Fusion Reactions*, March 24-26, 1986, ANL.

[28] O. Tanimura, *Phys. Rev. C* **35**, 1600 (1987).

[29] N. Takigawa, Y. Alhassid and A. B. Balantekin, *Phys. Rev. C* **45**, 1850 (1992).

[30] J. Gomes-Camacho and R. C. Johnson, *Jour. Phys. G* **12**, L235 (1986); *Jour. Phys. G* **14**, 609 (1988).

[31] P. Mclenithen and D. Secrest, *J. Chem. Phys.* **80**, 2480 (1984).

[32] P. McGuire and D. J. Kouri,, *J. Chem. Phys.* **60**, 2488 (1974).

[33] M. Moribayashi, S. Takada and H. Nakamura, *J. Chem. Phys.* **100**, 4284 (1994).

[34] Y. Alhassid, V. Liu and B. Shao, *Phys. Rev. A* **46**, 3865 (1992); emph-Phys. Rev. A **48**, 2832 (1993).

[35] K. Hagino, N. Takigawa, A. B. Balantekin and J. R. Bennett, *Phys. Rev. C* **52**, 286 (1995).

[36] A. T. Kruppa, P. Romain, M. A. Nagarajan and N. Rowley, *Nucl. Phys.* **A560**, 845 (1993).

[37] A. Bohr and B. Mottelson, *Nuclear Structure* (Benyamin, New York,1975), Vol. 2.

[38] P. Fröbrich and R. Lipperheide, *Theory of Nuclear Reactions* (Oxford University Press, New York, 1996), p.247.

[39] J. de Boer and J. Eichler *Advanced in Nuclear Physics*, (Plenum Press, New York, 1968) Vol.I, p.1.

[40] R. A. Broglia and A. Winther, *Heavy Ion Reactions (Lecture Notes), Volume 1: Elastic and Inelastic Reactions* (The Benjamin/Cummings Publishing Company, Inc., 1981), p.114.

[41] K. Hagino *et al.* (to be published).

[42] T. Kibedi and R. H. Spears, *At. Data Nucl. Data Tables* **80**, 35 (2002).

[43] S. Raman, C. W. Nestor, and P. Tikkanen, *At. Data Nucl. Data Tables* **78**, 1 (2001).

[44] Muhammad Zamrun F. and Hasan Abu Kassim, *AIP Conf. Proc.* **1328**, 74 (2012).

[45] Muhammad Zamrun F., K. Hagino, S. Mitsuoka, and H. Ikezoe, *Phys. Rev. C* **77**, 034604 (2008).

[46] M. A. Cândido Ribeiro, L. C. Chamon, D. Pereira, M. S. Hussien, and D. Galetti, *Phys. Rev. Lett* **78**, 3270 (1997).

[47] L. C. Chamon, D. Pereira, M. S Hussein, M. A. Cândido Ribeiro, and D. Galetti, *Phys. Rev. Lett* **79**, 5218 (1997).

[48] L. C. Chamon, B. V. Carlson, L. R. Gasques, D. Pereira, C. De Conti, M. A. G. Alvarez, M. S. Hussien, M. A. Cândido Ribeiro, E. S. Rossi, Jr., and C. P. Silva, *Phys. Rev. C* **66**, 014610 (2002).

[49] G. R. Satchler, *Phys. Rep.* **199**, 147 (1991).

[50] C. Mahaux, H. Ngo, and G. R. Satchler, *Nucl. Phys.* **A449**, 354 (1986).

[51] M. A. Nagarajan, C. Mahaux, and G. R. Satchler, *Phys. Rev. Lett.* **54**, 1136 (1985).

[52] W. Y. So, T. Udagawa, K. S. Kim, S. W. Hong, and B. T. Kim, *Phys. Rev. C* **76**, 024613 (2007).

[53] W. Y. So, T. Udagawa, S. W. Hong, and B. T. Kim, *Phys. Rev. C* **77**, 024609 (2008).

[54] A. Iwamoto, and K. Harada, *Z. Phys. A* **326**, 201 (1987).

[55] R. A. Broglia and A. Winther, *Heavy Ion Reactions*, Vol. 84 in Frontier in Physics Lecture Notes Series (Addison-Wesley, Redwood City, CA, 1991).

[56] O. Akyüz and A. Winter, in Proc. of the Enrico Fermi School of Physics, 1979, *Course on Nuclear Structure and Heavy-Ions Reactions*, Ed. R. A. Broglia, C. H. Dasso, and R. Ricci (North Holland, Amsterdam, 1981).

[57] P. R. Christensen and A. Winther, *Phys. Lett.* **B65**, 19 (1976).

[58] L. C. Vaz, J. M. Alexander and G. R. Satchler, *Phys. Rep.* **69**, 373 (1981).

[59] J. R. Leigh, M. Dasgupta, D. J. Hinde, J. C. Mein, C. R. Morton, J. P. Lestone, J. O. Newton, H. Timmers, J. X. Wei and N. Rowley, *Phys. Rev. C* **52**, 3151 (1995).

[60] H. Esbensen and B. B. Back, *Phys. Rev. C* **54**, 3109 (1996).